# Photosynthetic Water Oxidation in Plants and Cyanobacteria - Activation Energy of the O-O Bond Formation Step and Substrate Analogue NH3

**Dissertation**

zur Erlangung des Grades eines

Doktors der Naturwissenschaften

am Fachbereich Physik

der Freien Universität Berlin

vorgelegt von

**Zhiyong Liang**

Berlin 2018

Prof. Dr. Holger Dau (Betreuer, Erstgutachter)

Prof. Dr. Ulrike Alexiev (Zweitgutachterin)

Datum der Disputation: 7. 5. 2018

I wish to dedicate this thesis to my beloved parents.

致我的父亲母亲

# Glossary

| | |
|---|---|
| **AD** | Analogue-to-digital |
| **BBY** | PSII enriched membrane particles, named after Berthold, Babcock and Yocum |
| **Chl** | Chlorophyll |
| **DAQ** | Data acquisition |
| **DCBQ** | 2,6-Dichloro-1,4-benzoquinone |
| **DF** | Delayed chlorophyll fluorescence |
| $E_a$ | Activation energy |
| $E_a^H$ | Enthalpy of activation |
| $E_a^S$ | Entropy of activation |
| **EEC** | Enthalpy-entropy compensation |
| **EPR** | Electron paramagnetic resonance |
| **FTIR** | Fourier-transform infrared |
| **FWHM** | Full-width at half-maximum |
| **G** | Gibbs free energy |
| $K_M$ | Michaelis  constant |
| **LHC** | Light harvesting complex |
| **NADP** | Nicotinamide adenine dinucleotide phosphate |
| **OEC** | Oxygen evolving complex |
| **OP** | Time-resolved oxygen polarography |
| $P_{680}$ | Primary electron donor of PSII |
| $P_{700}$ | Primary electron donor of PSI |
| **PF** | Prompt chlorophyll fluorescence |
| **Phe** | Pheophytin |
| **PSI** | Photosystem I |
| **PSII** | Photosystem II |

| | |
|---|---|
| **$Q_A$** | Primary quinone acceptor of PSII |
| **$Q_B$** | Secondary quinone acceptor of PSII |
| **QM/MM** | Quantum mechanics/molecular mechanics |
| **RC** | Reaction centre |
| ***Syn.*** | *Synechococcus* |
| ***T. elongatus*** | *Thermosynechococcus elongatus* |
| **TST** | Transition state theory |
| **TTL** | Transistor-transistor-logic |
| **WT** | Wild-type |
| **XFEL** | X-ray free electron laser |
| **$Y_D$** | Tyrosine D (D2-Tyr160) of PSII |
| **$Y_Z$** | Tyrosine Z (D1-Tyr161) of PSII |

# Contents

# Chapter 1 Introduction

Where does the oxygen in the atmosphere come from? And how fast does the nature produce oxygen molecule? This is a very old topic dating back to almost three billion years ago when the atmosphere was changed from an anaerobic to an aerobic one, first by cyanobacteria and then later on additionally by algae and plants.

Generations after generations of scientists make enormous efforts digging into the details of the mechanisms of photosynthesis in order to reveal the secrets of this photochemical reaction (Dau & Zaharieva, 2009; Vinyard & Brudvig, 2017). The whole process of photosynthesis is found to be very complicated, thus it could take decades (or even centuries) to discover the fine details. One of the essential steps is the oxidation of water in the protein complex photosystem II (PSII), where oxygen is produced from water, driven by absorption of solar radiation. Luckily, PSII is not as unreachable as a black hole. This means that it can be approached by a number of modern techniques and in the end, all its functions and key questions are likely to be solved in the foreseeable future.

In this study the goal of the research described in the following was to explore the function of PSII, focusing on (1) the water oxidation process, by understanding the O-O bond formation, specifically from the kinetic and energetic point of view; and (2) the co-solvent effects, as an approach for new insight into the electron and protonation dynamics. Currently, a set of well-developed high profile methods form a solid base to study PSII. The basic background knowledge of this topic is to be introduced in the following sections.

## 1.1 Photosynthesis

Photosynthesis is a process of transforming light energy into chemical energy and producing the sugar needed in all living species. It takes place in the thylakoid membrane of cyanobacteria, algae and plants. The main protein complexes are photosystem II (PSII), cytochrome $b_6f$, photosystem I (PSI) and adenosine triphosphate (ATP) synthase, which, together with further electron carriers, compose the electron transfer chain (Figure 1.1). Photosynthesis includes energy-fixing (light reactions) and carbon-fixing reactions (dark reactions). In the energy fixing-reaction, water is transformed into oxygen, nicotinamide adenine dinucleotide phosphate (NADP) into NADPH and ADP into ATP respectively; while in the carbon fixing reactions carbon dioxide is essential to sugar formation. The overall equation of the photosynthesis can be expressed as

$$\text{solar energy} + 6H_2O + 6CO_2 \rightarrow 6O_2 + C_6H_{12}O_6 \,.$$

First of all, the photon energy is taken up by the reaction centre chlorophylls ($P_{680}$), a special pair of chlorophylls in PSII. This photochemical reaction initiates charge separation that the primary electron transfer takes place from the oxidation of $P_{680}$ to reduction of a specific pheophytin, followed by the reduction of a quinone molecule. The flow of electrons runs through cytochrome $b_6f$ to PSI in which the reaction centre ($P_{700}$) is excited by photon energy, initiating another chain of electron transfer processes that reduces NADP into NADPH. The released electron from $P_{680}$ is substituted by the one generated from water oxidation in the oxygen evolving complex (OEC). The protons released from water oxidation within the OEC together with those from the $PQH_2$ pool form a transmembrane proton gradient and thus power the synthesis of ATP from ADP (Figure 1.1).

The very central system of this study is PSII, the catalyst allowing for oxygen evolution by water oxidation. This protein complex is a dimer composed of at least 20 protein subunits and is introduced in the following section.

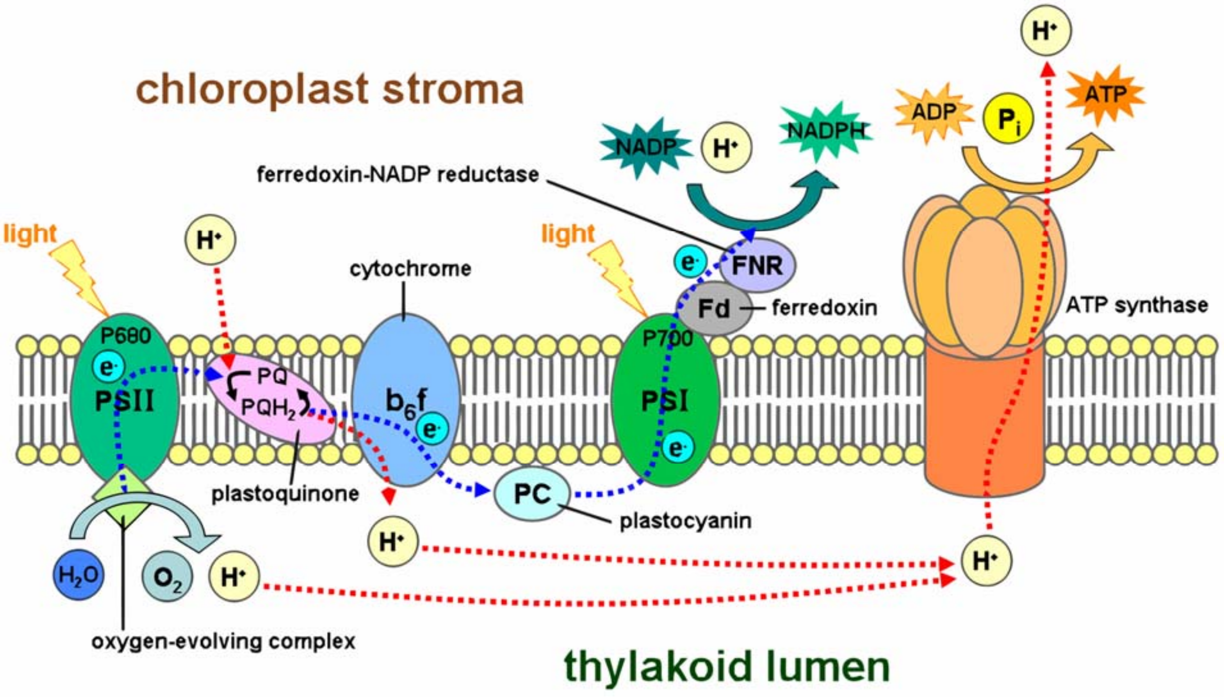

**Figure 1.1. Light-dependent reactions of photosynthesis at the thylakoid membrane (Somepics, 2018). For further details of the shown compounds of the photosynthetic electron transfer chain, see (Blankenship, 2002).**

## 1.2 Photosystem II

PSII is located in the thylakoid membrane of the grana particles, which are embedded in the cells of cyanobacteria, green algae and plants. A high resolution crystal structure of PSII protein has been resolved in a resolution of 1.9 Å (Figure 1.2) (Umena et al., 2011). Nearly each of the atom positions is well defined (aside from the protons).

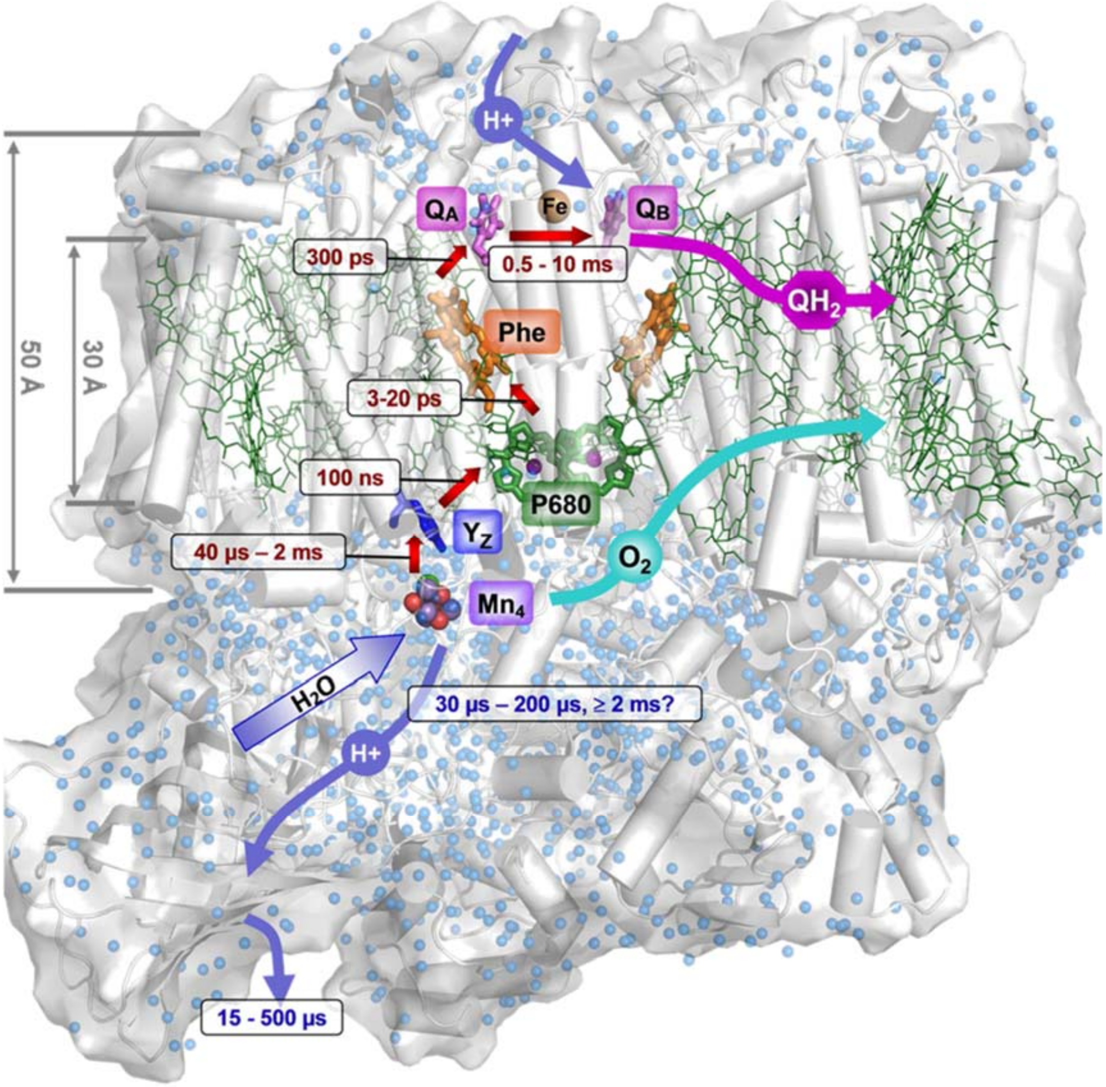

**Figure 1.2. Photosystem II structure based on Protein Data Base entry 3ARC (Umena et al., 2011) with indication of the key redox cofactors and dimensions of the PSII complex. The red arrows connect the redox cofactors of the electron transfer chain from the donor side including Mn-complex, a redox-active tyrosine ($Y_Z$) and the primary electron donor ($P_{680}$) to the acceptor side containing the primary pheophytin acceptor (Phe), the primary ($Q_A$) and secondary ($Q_B$) quinone acceptors. See further details in (Dau et al., 2012).**

It is a dimeric protein complex containing at least 20 subunits, including membrane-extrinsic and -intrinsic proteins. Among the intrinsic ones, the D1, D2, CP43 and CP47 (also called PsbA, PsbD, PsbC and PsbB) proteins function as the central core of the complex and facilitate photosynthetic water oxidation. In each monomer of PSII the functionality is supported by a number of cofactors, including for instance, 35 chlorophylls, 11 ß-cartotenoids, 2 pheophytin, 2 plastoquinones, 2 heme irons, 1 non-heme iron, 4 manganese atoms, 3 to 4 calcium atoms, 1 bicarbonate, 3 chloride, 23 lipids and more than 1,300 water molecules (Umena et al., 2011).

## 1.2.1 Photochemical Reaction and Electron Transfer

Photoabsorption by one of the roughly 200 chlorophylls in the light-harvesting complex (LHC) of PSII in plants results in formation of an equilibrated excited state ($Chl_{200}$*) and is followed by $P_{680}$ chlorophyll oxidation (formation of $P_{680}^+$) with a quantum efficiency close to unity (Dau & Zaharieva, 2009). This special pair of Chl-a is named $P_{680}$, since it absorbs maximally at a wavelength of 680 nm, thus its excited state energy is equivalent to 1.83 eV following

$$E = hc/\lambda\,, \tag{1.1}$$

where $E$ is the energy in unit of eV, $h$ is the Planck constant, $c$ is the speed of light in vacuum and $\lambda$ is the wavelength of a photon.

At the electron acceptor side, the photochemical reaction initiated by the photon absorption is an electron transfer from $P_{680}$ to pheophytin (Phe), forming the radical pair of $P_{680}^+Phe^-$ within 3 ps (Dau, 1994; Dau et al., 2012). And the electron transfer proceeds further to a firmly bound $Q_A$ within 300 ps thus forming $P_{680}^+Q_A^-$ (Dau, 1994; Dau et al., 2012). The $Q_A$ is subsequently oxidized by the $Q_B$ supported by a loosely bound heme iron ion. After accumulation of two electrons at the $Q_B$ side, two protons from the protein environment bind, forming $Q_BH_2$. $Q_BH_2$ leaves the PSII as shown in the scheme of Figure 1.2. See also the scheme in Figure 1.3 for simplicity.

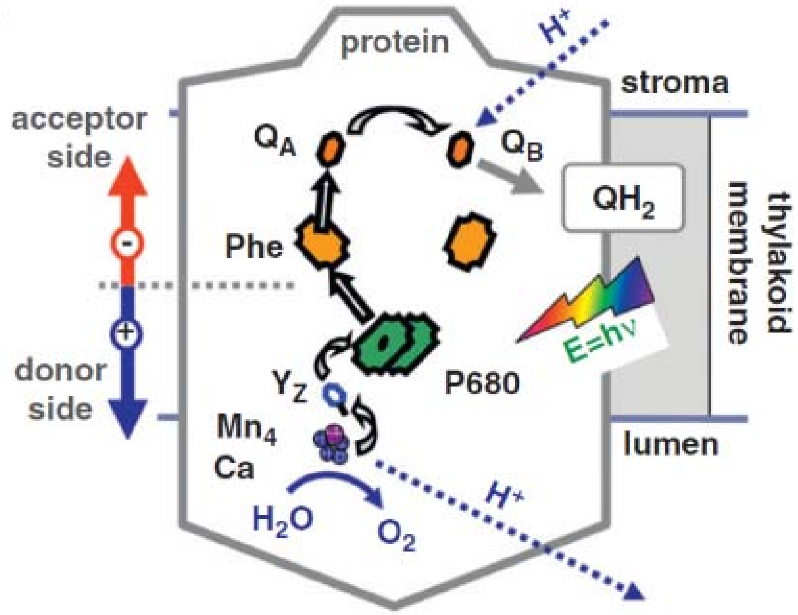

**Figure 1.3. Simplified scheme of the electron transfer path from the donor to the acceptor side within photosystem II (Dau et al., 2012).**

At the donor side, the $P_{680}^+$ is reduced by a redox-active tyrosine residue, denoted as $Y_Z$, within about 100 ns. And the $Y_Z$ gets reduced by the catalytic Mn-complex within 40 µs to 2 ms, depending on the oxidation states of the complex. Up to date, the precise structure of the OEC in specific states is still one of the most important unsolved questions.

### 1.2.2 Oxygen Evolving Complex and Water Oxidation

The oxygen evolving complex (OEC) contains tyrosine Z ($Y_Z$), several highly conserved amino acids of the D1 and the CP43 protein, which ligate the inorganic metal cluster ($Mn_4CaO_5$). The metal ions are coordinated to four water molecules, one histidine and carboxylate ligands (Figure 1.4). The Mn-complex functions as a catalyst and facilitates the water oxidation by accumulating four oxidation states after four photons absorption events, resulting in the splitting of two water molecules into four protons and electrons (reducing equivalents) as well as one di-oxygen molecule as byproduct:

$$2H_2O \rightarrow 4H^+ + 4e^- + O_2 .$$

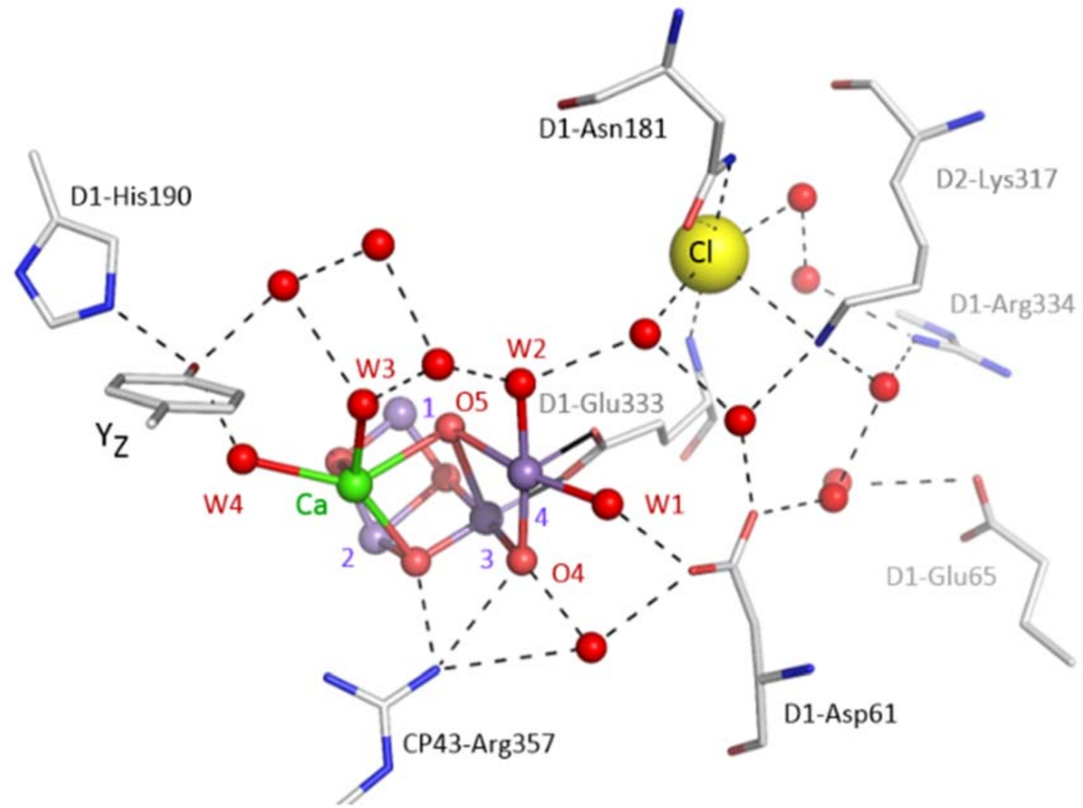

**Figure 1.4. Water-oxidizing manganese complex and redox-active tyrosine of photosystem II (PSII). The $Mn_4Ca(\mu\text{-}O)_5$ core of the Mn-complex is bound to amino acid residues of the D1 and of the CP43 protein (Klauss, Sikora, et al., 2012).**

For decades the scientific community has been dealing with the challenge of understanding the mechanism of this catalytic centre. One of the breakthroughs was back in 1970 when it was discovered that the oxidation states of the OEC follow a quaternary periodic pattern in a damped oscillation with maxima at the 3rd and the 7th and minima at the 1st and the 5th saturating light flashes (Kok et al., 1970). This oscillation cycle was interpreted as 5 semi-stable states, $S_i$ (i = 0 - 4) by taking into account also an intermediate state, nominated as $S_4$, which is a transiently formed state prior to oxygen formation. The dynamics of proton and electron transfer within the cycle were further extensively investigated and discussed, for instance, as can be seen in Figure 1.5 (Klauss, Haumann, et al., 2012). Up to date, progress has been achieved by resolving possible structures of the individual states ($S_0$ to $S_2$) (Askerka et al., 2017), for instance, by X-ray diffraction (Umena et al., 2011), X-ray free electron laser crystallography (XFEL) (Young et al., 2016) and extensive quantum mechanics/molecular mechanics (QM/MM) calculations (Shen, 2015). However, the structure of the $S_4$ state, from which one could get insight into the O-O bond formation, is still poorly understood (Vinyard & Brudvig, 2017).

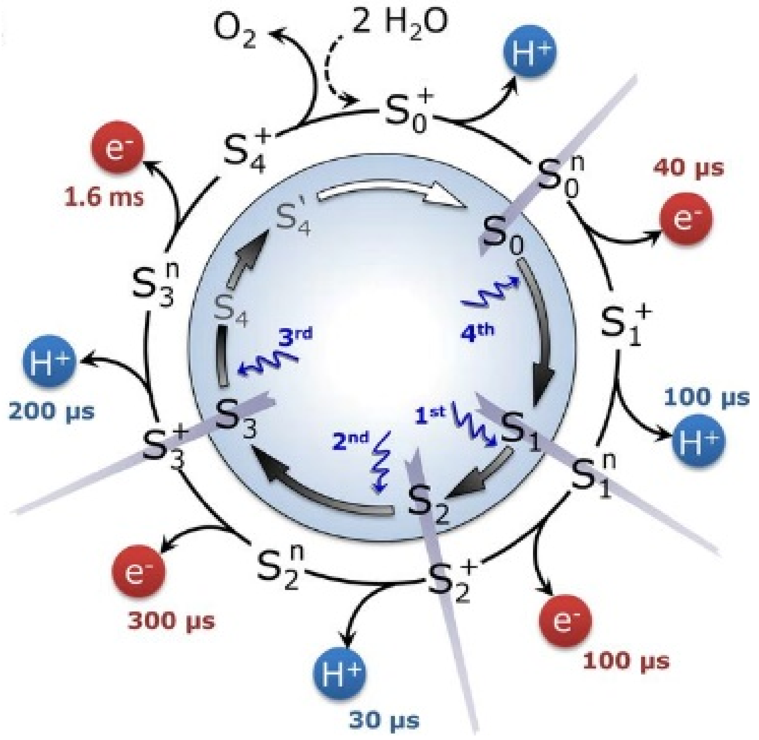

**Figure 1.5. Extended Kok cycle presenting alternating protonation and electron transfer between each S-state transition. The subscripts indicate the number of oxidation equivalents accumulated at the Mn-complex (starting from $S_0$) while the superscripts indicate the charge relative to the dark-stable $S_1$ state (+, positive; n, neutral) (Klauss, Haumann, et al., 2012).**

A cycle of four S-state transition can be summarized as follows (Dau & Haumann, 2008; Vinyard & Brudvig, 2017):

(i) $S_0$ to $S_1$

$S_0$ is the most reduced state, containing $(Mn^{3+})_3Mn^{4+}$. DFT and QM/MM studies suggest that, the oxidation states pattern for Mn1, Mn2, Mn3 and Mn4 are III, IV, III and III respectively (Pal et al., 2013; Siegbahn, 2013). See Figure 1.4 for atom numbering. The charge separation of $P_{680}$ induces the oxidation of $Y_Z$, forming $Y_Z^+$, which oxidizes $S_0$ to $S_1^+$, specifically oxidizing $Mn_3$ from $Mn^{3+}$ to $Mn^{4+}$. This change decreases the $pK_a$ of $O_5$ dramatically, and thus is followed by a deprotonation from $O_5$, forming $S_1^n$ with the oxidation states pattern as III, IV, IV and III (Koulougliotis et al., 1992).

(ii) $S_1$ to $S_2$

This transition involves only an electron transfer step but no proton release, i.e. the oxidation of one $Mn^{3+}$ to $Mn^{4+}$, forming $S_2^+$. The $S_2$ state has been intensively studied, for instance by electron paramagnetic resonance (EPR) spectroscopy (Haddy, 2007; Pokhrel & Brudvig, 2014). It contains two spin isomers:

1) A g = 4 EPR signal with a ground state of S = 5/2 with a Mn oxidation states pattern as IV, IV, IV and III as a closed cubane where the dangler Mn4 is a five coordinate $Mn^{3+}$ center and weakly bound to the other three Mn ions;
2) A g = 2 EPR signal with a ground state of S = 1/2 with a Mn oxidation states pattern as III, IV, IV and IV as an open cubane, where the Mn1 is a five coordinate $Mn^{3+}$ center and all Mn ions are connected by di-µ-oxo bridges (Haddy, 2007; Pantazis et al., 2012).

(iii) $S_2$ to $S_3$

An external water molecule is added to the OEC in this step, which involves deprotonation, Mn oxidation and water coordination (Klauss, Haumann, et al., 2012) and finally forming a Mn oxidation states pattern as IV, IV, IV and IV, i.e. $(Mn^{4+})_4$. However, the mechanism of this transition is still under debate, mainly among three models.

Starting from an open cubane, an external water molecule is added to $Mn_1$ as an additional ligand. This is proposed by DFT calculation and confirmed by EPR experiment (Cox et al., 2014; Siegbahn, 2013).

Alternatively, starting from a closed cubane, W3 moves to Mn4 followed by a water molecule (from the OEC external surrounding) taking the previous site of W3, proposed by computational calculations (Bovi et al., 2013; Krewald et al., 2016; Shoji, Isobe, & Yamaguchi, 2015). In another perspective, a water molecule from the second sphere, couples to the $Mn_4$ as a direct ligand by altering the position of W1 and W2 (Capone et al., 2016; Retegan et al., 2016).

(iv) $S_3 \rightarrow S_4$ to $S_0$

This is the most complex transition. It involves a proton and an electron transfer, forming an intermediate $S_4$ state with O-O bond formation, followed by oxygen release and water binding, and another proton transfer to form the $S_0$ state. The detail processes are introduced in the next section.

### 1.2.3 O-O Bond Formation

This is the energetically most demanding step of water oxidation, in which the Mn-complex advances from $S_3$ to the $S_0$ state via the transient $S_3Y_Z^{ox}$ and $S_4$ states ($S_3 \rightarrow S_3Y_Z^{ox} \rightarrow S_4 \rightarrow S_0$ transition) (Kern et al., 2014). In this step two substrate water molecules are oxidized by the OEC followed by the evolution of an $O_2$ molecule.

The mechanism of the O-O bond formation is not yet fully understood or verified. However, two conceivable mechanisms are suggested and supported by a number of experimental evidences and computations, namely oxo-oxyl radical coupling and nucleophilic water attack mechanisms, respectively; see review paper (Vinyard & Brudvig, 2017). Recently it was reported based on DFT calculations that the latter mechanism (nucleophilic water attack) is impossible due to the high energetic barrier (23.1 kcal/mol) in comparison to the efficient oxo-oxyl mechanism with a barrier of only 6.2 kcal/mol (Siegbahn, 2017).

The O-O bond formation has been probed by substrate and enzyme modifications, targeting to reveal the impact on kinetic and thermodynamic parameters. In the case of substrate modifications, substrate analogues and inhibitors were used. Typical analogues and cosolvents applied in the study of O-O bond formation have been reported, for instance (here only comparably recent references are cited):

(i) methanol (Dixon et al., 2012; Ho & Styring, 2008; Noring et al., 2008a, 2008b; Su et al., 2011),
(ii) ethanol (Åhrling et al., 2004),
(iii) ammonia (Dau et al., 1995; Hou et al., 2011; Navarro et al., 2013; Vinyard et al., 2016; Vinyard & Brudvig, 2015) and
(iv) glycerol (Dashnau et al., 2006; Fang et al., 2005; Gekko & Timasheff, 1981; Hussels & Brecht, 2011a, 2011b; Vagenende et al., 2009a, 2009b).

For example, in a recent crystallographic study ammonia was applied as a substrate analogue (Young et al., 2016). From the resolved atomic structure and combined data with EPR and oxygen evolving activity, it was suggested that ammonia may replace W2 from the $Mn_4$, but without inhibition of oxygen evolution. This led to the conclusion that W2 likely is not a substrate water. Accordingly, all the mechanisms involving W2 that explained the O-O formation are disfavored. This evidence helps to address the likelihood of the mechanism of O-O formation, even though it may contradict some other experimental findings and computations.

Regarding the enzyme modifications, natural PSII variants from different species or site-directed mutations of PSII have been used in comparative studies (Bao & Burnap, 2015; Cox et al., 2011; Rappaport et al., 2011). All these inspire the idea to probe the kinetics of O-O formation by substrate analogues/cosolvents (ammonia in Chapter 3 and glycerol in Chapter 4) as well as to compare the activation energy among different species (in Chapter 5), so that the impact factors for the O-O formation can be understood in a further step.

## 1.3 Activation Energy and Transition State Theory

### 1.3.1 Catalytic (Enzymatic) Mechanism and Activation Energy

In each chemical reaction, a certain energetic barrier has to be crossed in order to achieve a transiently formed higher energetic state (transition state), followed by a downhill reaction to generate the product (Figure 1.6). According to the transition state theory, the required effort to overcome this barrier is defined as activation energy. In a reaction an enzyme is able to accelerate the reaction rate by lowering the barrier, consequently initiating the reaction, for example, hundreds of times faster.

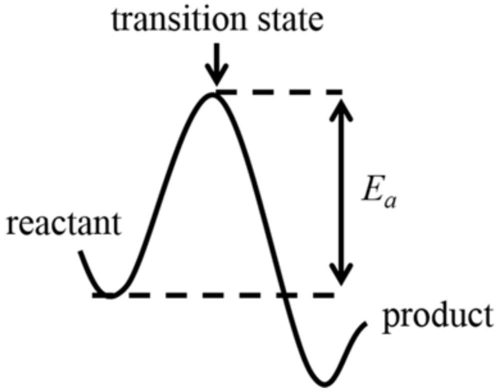

**Figure 1.6. Simplified scheme on transition state theory. Starting with the reactant, a chemical reaction happens by crossing an energetic barrier ($E_a$) thereby passing a transition state, which is followed by a downhill reaction to generate the product.**

## 1.3.2 Enthalpy Entropy Compensation

Enthalpy-entropy compensation (EEC) refers to a situation, where a change of enthalpy (decrease/increase) is compensated by an increase /decrease of entropy. It is a fundamental phenomenon, existing in chemical reactions from micro- to macro-molecular levels. See examples of EEC in certain proteins (Borsarelli & Braslavsky, 1998; Chodera & Mobley, 2013; Ferrante & Gorski, 2012; Losi et al., 2001). Nevertheless, it is under debate, because the reported EEC effects were often criticized to be the contribution from experimental errors and limitations (Chodera & Mobley, 2013).

Specifically in a protein environment, EEC has been widely and intensively investigated in both experimental and theoretical studies. In recent years, studies of protein-ligand associations have suggested certain forms of EEC effects to explain protein thermodynamics. However, it is still experimentally one of the biggest challenges to quantify the change of enthalpy and entropy precisely. One of the profound methods applied, for instance in PSII studies, is the photoacoustic technique, by which the enthalpy variation of the protein might be probed, but often protein volume changes dominate the signals and render the determination of the reaction enthalpy problematic (Hou & Mauzerall, 2011; Klauss et al., 2009; Krivanek et al., 2008). However, even if successful, these studies reveal only the total enthalpy and entropy of the reaction, which are not the enthalpy/entropy of activation that matter in transition state theory (TST).

Alternatively, the Arrhenius and Eyring plots are often used to express the correlation between the rate constant and temperature dependence of a specific chemical reaction. The details of these two approaches are presented in the next section.

## 1.3.3 Mathematical Method of Determining Activation Energy

### 1.3.3.1 Arrhenius Equation

The Arrhenius equation was firstly proposed by Svante Arrhenius back in the year 1889, based on the Van't Hoff's equation developed in 1884. The equation addresses the correlations between the rate constant of a chemical reaction and the temperature

$$k = Ae^{-E_a/k_BT} , \qquad \textbf{(1.2)}$$

where *k* is the rate constant, *A* the pre-exponential factor, $E_a$ the activation energy of a reaction, $k_B$ the Boltzmann constant and *T* the absolute temperature (in Kelvin). This leads to an alternative form in terms of natural logarithm on both sides of the equation, giving

$$\ln(k) = -E_a\left(\frac{1}{k_BT}\right) + \ln(A). \tag{1.3}$$

A plot of ln($k$) versus $1/T$ yields a curve that can be fitted with a linear regression, of the form "y = ax+b", from which the slope (a) and intercept (b) can be applied to determine the values of $E_a$ and *A* respectively:

$$E_a = -k_B\frac{dln(k)}{d\left(\frac{1}{T}\right)} \approx k_BT_0^2\frac{dln(k)}{d(T)}\,, \tag{1.4}$$

for temperatures in the vicinity of $T_0$; and

$$A = e^b\,. \tag{1.5}$$

### 1.3.3.2 Transition State Theory and Eyring Equation

For a chemical reaction, the transition state theory (TST) can be further well described by the Eyring Equation, which was developed by Henry Eyring in 1935 based on TST and the Arrhenius equation, correlating reaction rates to the temperature. The Equation is given by

$$k = \frac{k_BT}{h}e^{-\frac{\Delta G}{k_BT}} = \frac{k_BT}{h}e^{-\frac{\Delta H}{k_BT}}e^{\frac{\Delta S}{k_B}}\,, \tag{1.6}$$

where *k* is the rate constant, $k_B$ the Boltzmann constant and *T* the absolute temperature (in Kelvin), *h* the Planck constant, *ΔH* the enthalpy of activation, *ΔS* the entropy of activation and the Gibbs energy of activation $\Delta G$ $(= \Delta H - T\Delta S)$. Accordingly, by taking the natural logarithm on both sides, it gives:

$$\ln(k) = \ln(T) + \ln(\frac{k_B}{h}) + \frac{\Delta S}{k_B} - \frac{\Delta H}{k_BT} \tag{1.7}$$

$$\frac{dln(k)}{d(T)} = \frac{1}{T} + \frac{1}{T^2}\frac{\Delta H}{k_B}\,. \qquad \textbf{(1.8)}$$

Eq. (1.8) is based on the derivative of $k$ to $T$ from Eq. (1.7). The combination of Eq. (1.4) and (1.8) gives the correlation between activation energy and enthalpy for a specific temperature

$$E_a = \Delta H + k_B T_0\,. \qquad \textbf{(1.9)}$$

The value of $k_B T_0$ is about 25.3 meV at room temperature (20 °C).

The combination of Eq. (1.3) and (1.7) yields:

$$\frac{\Delta S}{k_B} = \ln(\frac{h}{k_B T}) + \frac{\Delta H}{k_B T} + \ln(k) = \ln(\frac{Ah}{k_B T}) + \frac{\Delta H}{k_B T} - \frac{E_a}{k_B T} = \ln\left(\frac{Ah}{k_B T}\right) - 1\,. \qquad \textbf{(1.10)}$$

Therefore, the entropy can be expressed as

$$\Delta S = k_B \ln\left(\frac{Ah}{k_B T}\right) - k_B\,. \qquad \textbf{(1.11)}$$

This means that the analysis of a plot of ln($k$) versus $1/T$ by linear regression yields a slope and an intercept, from which one can determine the values of $\Delta H$ and $\Delta S$, respectively.

## 1.4 Goal of This Study

Regarding the functionality of PSII there are still various open questions that need to be answered in order to understand such a complex system in full detail. One of the central challenges is to understand the mechanism of O-O bond formation in water oxidation, for instance, from a kinetic and energetic point of view. In this study three main perspectives are under investigation:

(i) Ammonia - identification of the substrate water

Ammonia, as a water analogue, has been used to probe the substrate water in PSII study for decades. Controversial evidence has been reported about whether ammonia inhibits the oxygen evolving activity or not. If yes, which place can be the binding site? (Andréasson et al., 1988; Andréasson &

Lindberg, 1992; Beck et al., 1986; Boussac et al., 1990; Oyala et al., 2015; Velthuys, 1975; Vinyard et al., 2016; Vinyard & Brudvig, 2015)

(ii) Glycerol - kinetic influence on proton and electron transfer

Glycerol, commonly used as a cyroprotectant and cosolvent in protein preparation, was resolved in the crystal structure of PSII. How does it affect the kinetics of proton and electron transfer in the water oxidation process as well as the O-O bond formation?

(iii) Activation energy of O-O bond formation - comparison among different species

Last but not least, the O-O bond formation from $S_3$ to $S_0$ transition is not yet fully understood from a thermodynamic point of view. Is the reaction driven by enthalpic or entropic factors? The comparison of activation enthalpy and entropy in this process among different species can supply more information to understand the mechanism.

# Chapter 2 Material and Methods

## 2.1 Biological Samples

First of all, it is necessary and worthwhile to appreciate that the PSII preparations from various biological sources are a joint effort, from spinach specifically including Monika Fünning, Philipp Simon, Dr. Matthias Schönborn, Dr. Ivelina Zaharieva, Dr. Petko Chernev and Jan Köhne while from cyanobacteria by a group of specialists in molecular biology headed by Dr. Yvonne Zilliges, constituted of Rebecca Christiana, Janis Hantke, Elena Laufer, Valentina Teresa Tovazzi and Hannah Davis to the best knowledge of the author.

All steps of the preparations, handling and storage of the PSII samples were done under dim green light in a cool room (4 ºC) or in an icy cold container. Therefore, the activity of the biological samples is preserved as far as possible by preventing their degradation and keeping the particles in the dark-adapted state. The composition of the relevant buffer are attached in Appendix A.

### 2.1.1 PSII-enriched Membrane Preparation from Spinach

PSII is enriched in grana stacks of thylakoid membrane inside the chloroplast of plants such as spinach. The method of extracting PSII-enriched membrane particles from spinach was established by Berthold, Babcock and Yocum (Berthold et al., 1981), thereafter short-named as BBY. The preparation was later on improved by Dau and co-workers (Schiller & Dau, 2000) by adding 1M Betaine in order to increase protein stability and thus achieve higher oxygen evolution activity (now commonly used in a number of laboratories in the PSII research community). To isolate the grana, the thylakoid membrane is required to be extracted by disrupting the chloroplasts. The preparation consists of mechanical chloroplasts disruption, detergent treatment and several rounds of differential centrifugations, with more details in the following:

Step I: mechanical cell breakage and chlorophyll isolation.

The spinach leaves (from organic farm) were gently washed in demineralized water and then put into a blender (containing buffer A). A mechanic approach was applied by breaking the cells in order to access the chlorophyll. The unbroken leaf tissues and the cellular debris were removed by filtering and differential centrifugation (in buffer A).

Step II: chloroplast breakage.

Osmotic shock by using a buffer containing 0.4M sucrose (buffer B).

Step III: thylakoid membrane isolation.

The thylakoid membrane embedded in the chloroplasts of the leaves was extracted with the help of differential centrifugation (in buffer B).

Step IV: separation of stacked PSII-enriched membrane particles from unstacked PSI.

The PSI-enriched membrane particles (as well as cytochrome $b_6f$) were dissolved in the detergent Triton-X100 (in buffer C) and removed by differential centrifugation. The process time of detergent treatment is critical due to its defragmentation of the insolubilized parts.

Step V: purification of PSII-enriched membrane particles from starch.

Finally, three to five centrifugation steps were applied (in buffer D) until the starches was completely removed from the pellet, giving the product of the PSII enriched membrane particles. The resulting activity was 1,000 - 1,200 µmol $O_2$ (mg Chl h)$^{-1}$ (at 25 $^{o}$C, pH 6.2) with a chlorophyll concentration of about 2 mg/mL while Chl-a to Chl-b ratio was about 2.5. The sample was aliquoted into individual reaction tubes and stored in the dark in a -80 $^{o}$C fridge.

### 2.1.2 Thylakoid Membrane Preparation from Cyanobacteria

The key procedures in principle were similar to the preparation from spinach. Cyanobacterial strains, namely *Thermosynechococcus elongatus* BP-1 (wild-type and PsbA3, also called $\Delta$*psbA*$_{1+2}$) and *Synechococcus* sp. PCC 7002 (wild-type, $\Delta$*psbA*1 and $\Delta$*psbA*2 mutants) were grown photoautotrophically in BG11 medium (Rippka, 1988) and in $A^+$ medium (Stevens & Porter, 1980) in 48°C and 38°C respectively, supplemented with $CO_2$-enriched air (1 % v/v) and continuous white light of 80 $\mu E \cdot m^{-2} \cdot s^{-1}$. See details of the mutation and protein preparation in (Schuth et al., 2017).

### 2.1.3 Sample Handling before Measurement

Before every experiment, the sample, i.e. PSII membrane particles (0.5 mL to 2 mL in reaction tubes) were taken from the -80 $^{o}$C fridge and thawed on ice for one hour. The sample was then centrifuged in 30 mL control buffer (see Table 2-1) at 4 $^{o}$C and 50,000 g (Rotor Sorvall SS-34, RPM 20,500) for 12 minutes, unless otherwise specified. Ice-cold buffer was used in this step in order to minimize denaturation of the protein. After centrifugation, the supernatant was discarded, thereby removing broken particles due to long time storage at low temperature. The pellet was resuspended in 1 mL to 2 mL of the same buffer and the chlorophyll concentration was measured. The sample solution was then calibrated into a chlorophyll concentration between 40 µg/mL to 130 µg/mL and kept on ice as a stock solution until measurement. The actual concentration depended on the corresponding detection system, experimental design and conditions.

**Table 2-1 A list of the control buffers used for the different chapters of this study, with the key difference at pH and in salt (NaCl) concentration. The samples denoted as BBY are the PSII enriched membrane particles from spinach, while cyano *T. el.* and *Syn. 7002 are* the thylakoid membrane particles from cyanobacterial *Thermosynechococcus elongates* BP-1 and *synechococcus* sp. PCC 7002 respectively. PF stands for prompt fluorescence, DF for delayed fluorescence and OP for oxygen polarography, the details of which are to be introduced in the following sections of this chapter. Full composition of all buffers are listed in Appendix A.**

| Chapter | sample | buffer | pH | NaCl [mM] | Method |
|---|---|---|---|---|---|
| 3: Ammonia Binding to the Water-oxidizing Manganese Complex of PSII | BBY, Cyano *T.el.* and *Syn.* 7002 | NaCl | 7.5 | 150 | PF, DF, OP |
| 4: Glycerol Effects in Kinetics of Protonation and Electron Transfer of PSII | BBY | D | 6.2 | 15 | PF, DF |
| 5: Activation Energy of O-O Bond Formation in PSII | BBY, Cyano *T.el.* and *Syn.* 7002 | ternary | 6.2 | 150 | PF, DF, OP |

## 2.2 Determination of Chlorophyll Concentration

For each measurement, 40 µL of membrane particles were dissolved into 10 mL of an acetone/water mixture (80%, 20%, v/v). The solvent was then centrifuged at 1,200 g (3,000 RPM) at room temperature for 4 minutes in a table centrifuge*[1] (see Table 2-2) in order to separate, for example, starch from the particles and thus obtain a fully transparent solution without side effects from light scattering due to turbidity. The absorbance of the remaining solution (i.e. the supernatant) was measured in a cuvette (1 cm optical path length) in a spectrometer*[2] (see Table 2-2) at 646 nm and 663 nm, which correspond to the maximum absorption wavelength of Chlorophyll a and b respectively. The chlorophyll concentration was then determined with the following equations (Lichtenthaler, 1987):

$$\mathrm{Chl}_a\ [\mathrm{mg/mL}] = 0.25 * [12.21 * A_{663} - 2.81 * A_{646}]\ ; \tag{2.1}$$

and

$$\mathrm{Chl}_b\ [\mathrm{mg/mL}] = 0.25 * [20.21 * A_{646} - 5.03 * A_{663}]\ , \tag{2.2}$$

where $A_{646}$ and $A_{663}$ denote the absorbance measured at 646 nm and 663 nm, respectively.

**Table 2-2 Supplementary information of experimental setup in determination of chlorophyll concentration.**

| Experimental setup | Type |
|---|---|
| *[1] Table centrifuge | Rotofix 32, Hettich |
| *[2] Spectrometer | Spectrometer, Varian Cary 50 UV-Vis spectrophotometer |

## 2.3 Prompt Fluorescence

The fluorescence emission follows a probability distribution from different fluorophores. So the distribution can be reconstructed by counting the emitting photons as a function of time, since the time course of each individual fluorophore follows an exponential decay. Based on this, the identification of the life time of the corresponding fluorophores can be determined (in terms of the rate constant) by curve fitting (Keith Wilson, 2010).

Fluorescence measurement is commonly used specifically in the study of biology to understand the physiological condition of the plants. In the research of photosystem the detection of variable fluorescence yield, denoted prompt fluorescence (PF) hereafter, has been applied in many PSII laboratories (Ananyev et al., 2005; de Grooth & van Gorkom, 1981; Goltsev et al., 2012; Sander et al., 2010; Thapper et al., 2009). The experimental setup has been commercialized, thus can be easily applied in vitro and vivo studies.

### 2.3.1 Principle of Prompt Fluorescence

Fluorescence emission that takes place within nano seconds after photoabsorption by a chlorophyll (Chl) molecule is called prompt fluorescence, which was first reported by Kautsky and Hirsch. Since then, this technique is commonly used in a few laboratories of photosynthesis research and has been summarized in extensive reviews (Dau, 1994; Papageorgiou & Govindjee, 2011; Shinkarev & Govindjee, 1993; Shinkarev et al., 1997).

Following each absorption of a photon and excitation of a Chl, there are three ways to distribute the energy (Figure 2.1) in terms of

(1) photochemical reaction followed by charge separation, forming radical pair of [$P_{680}^{+}Phe^{-}$] and [$P_{680}^{+}Q_A^{-}$] in a further step,
(2) non-radiative energy loss as heat dissipation, and
(3) decaying back to the ground state in terms of photoemission, i.e. fluorescence.

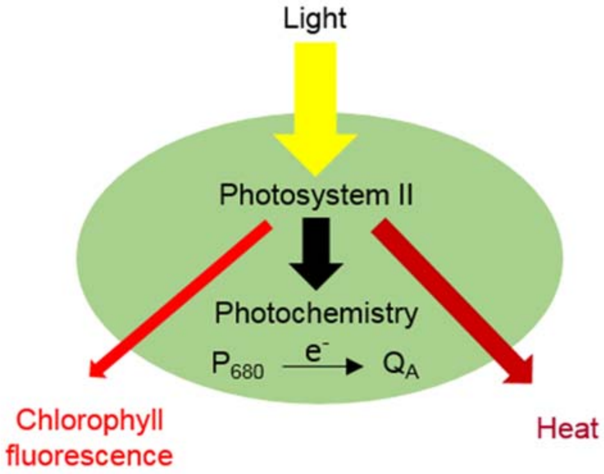

**Figure 2.1. Scheme of the energy distribution after photon absorption by chlorophyll, modified from reference figure in (Baker, 2008). Following each photoabsorption by a special pair of chlorophylls $P_{680}$ in photosystem II, there are three ways to distribute the energy terms of chlorophyll fluorescence (red arrow), heat (dark red arrow) and photochemical reaction (black arrow).**

The fluorescence takes place only within about 20 ns, since it is limited by the life time of the excited state of $P_{680}$ (Dau, 1994). This is a relatively fast process, therefore, it is called prompt fluorescence. It can be used as an indication of the redox state of the primary quinone ($Q_A$). Within approximately 300 ps after photon absorption and chlorophyll excitation, the $Q_A$ is reduced by an electron from $P_{680}$ via Pheophytin, as can be seen later in Figure 2.2. The yield of chlorophyll fluorescence is proportional to the population of reduced $Q_A$, thus the resulting PF signal makes the redox state of $Q_A$ visible (Dau, 1994). Therefore, the status of the $Q_A/Q_A^-$ can be approached by the PF signal. The PF signal is dominated by PSII, because the contribution of Photosystem I to the fluorescence emission is evaluated less than 5% at room temperature (Roelofs et al., 1992). It is thus especially useful in the study of PSII.

### 2.3.2 Data Acquisition of Prompt Fluorescence

The PF in this study was detected by a pump-probe technique, in which the PSII particles were pumped, i.e. excited by saturating (single turn-over) laser flashes through the S-state cycle. Between each individual S-state, the PSII particles were probed by a weak excitation light (625 nm). The measured intensity was correlated to the redox state of $Q_A$. The correlation between PF signal and the population of reduced $Q_A$, noted as $[Q_A^-]$ has been well studied in the past. See details in an intensive review (Dau, 1994).

Alternatively, instead of measuring the fluorescence intensity directly, the variable yield of PF was detected by a commercial fluorometer*[1] (see Table 2-3), in which a pair of LEDs probed the PSII samples by weak modulated excitation LED light*[2] (see Table 2-3) as a non-actinic excitation source without initiating the charge separation. When the $Q_A$ is reduced, the $P_{680}$ is blocked in such a way that the reaction center is not available to absorb a photon and to initiate charge separation. In contrast, if the $Q_A$ is oxidized, then the center is open and ready to absorb the incoming photon. So by using a non-actinic excitation light to probe PSII, fluorescence was induced and detected by a photodiode. The detailed introduction of this technique and setup can be found on the website of the fluorometer producer (http://www.psi.cz/).

Before the PSII dark-adapted particles were excited by a signal turn-over flash from a pulsed laser*[3] (see Table 2-3) from the top side of the cuvette, they were probed from two side windows five times in a spacing of 200 µs, giving an intensity of $F_0$ which refers to the status of fully oxidized $Q_A$. Subsequently, all the PSII particles were excited by a saturating flash, reducing all the $Q_A$ molecules and yielding a maximum intensity value, denoted as $F_M$. Therefore, the population of reduced $Q_A$ can be expressed as

$$\left[Q_A^-\right] = \frac{F_P(t) - F_0}{F_M - F_0} \quad . \tag{2.3}$$

The probe pulses were generated from 100 µs to 700 ms after the laser flash with an evenly distributed time spacing on a logarithmic scale, giving 6 pulses for each order of decay, thus 23 data points in total.

For temperature control, the cuvette holder was thermally regulated by a commercial circulator*[4] (see Table 2-3). The measurement started only after the sample temperature was thermally stabilized, which was observed by dipping a thermal sensor into the buffer in a sampling rate of 1 Hz, with precision of 0.1 °C. The overall thermal deviation through the detection was estimated to be less than ± 1 °C.

**Table 2-3 Supplementary information of experimental setup of prompt fluorescence.**

| Experimental setup | Type |
|---|---|
| *[1] Fluorometer | FL-3000, Photon System Instruments, by Czech Republic |
| *[2] LED light | 615 nm, HLMP-DH08, by Hewlett Packard |
| *[3] Pulse laser | 532 nm, Nd:YAG laser, by Continuum Minilite II |
| *[4] Circulator | Haake, DC50 |

### 2.3.3 Data Analysis

The PF decay is a multiphasic process, which is at least a tri-phasic decay (de Wijn & van Gorkom, 2001), including:

(1) a fast phase ($\tau < 1$ ms), refers to the electron transfer from $Q_A^-$ to $Q_B$ / $Q_B^-$ when the $Q_B$ is present in site and firmly bound;

(2) a medium phase (1 ms to 10 ms), associated with the binding process of $Q_B$ to the reaction centers followed by its reduction, and is dependent on the binding affinity of $Q_B$ / $Q_B^-$ to its own domain in PSII;

(3) a slow phase ($\tau > 10$ ms), connected to the charge recombination between the reduced $Q_A$ and oxidized factor, for example $P_{680}^+$ at the donor side.

Accordingly, the time course of PF is simulated by a sum of three exponential functions, which works as a base for the '$Q_A$ correction' of the delayed fluorescence decay (to be introduced in the next section):

$$F(t) = \left( \sum_{i=1}^{3} A_i \exp(-t/\tau_i) \right) + c \ , \tag{2.4}$$

where $A$ is the amplitude, $\tau$ the time constant, i.e. the reciprocal of the rate constant and $c$ the constant of the amplitude offset.

Consequently the rate constant (or half decay time, noted as $\tau_{1/2}$) of the electron transfer from $Q_A$ to $Q_B$ / $Q_B^-$ is accessible.

## 2.4 Delayed Fluorescence

The delayed fluorescence (DF), also called recombination fluorescence, refers to the fluorescence signal induced later than 20 ns after photon excitation because the rate constant of fluorescence emission of the excited chlorophyll in PSII antenna system is about $5*10^7$ $s^{-1}$ at room temperature (Dau, 1994). DF has been commonly used in photosynthesis research (Barber et al., 1977; Buchta et al., 2007; de Grooth & van Gorkom, 1981; Goltsev et al., 2009; Karge et al., 2014; Turzó et al., 2000; Van Gorkom et al., 1976; Venediktov et al., 1980). It was first reported in the 1950s (Strehler & Arnold, 1951) and then further analyzed and reviewed, for example by Govindjee and co-workers (Jursinic & Govindjee, 1977; Rutherford et al., 1984). Due to its sensitivity to the donor site of PSII, DF is an important tool to study the electron and proton movements kinetically and energetically (Buchta et al., 2007; Grabolle & Dau, 2005, 2007; Zaharieva et al., 2013).

### 2.4.1 Principle of Delayed Fluorescence

The delayed fluorescence (DF) is caused by the photon emission by the excited pigment $P_{680}$ due to charge recombination (back reaction of electron transfer). The emission spectrum of DF is highly similar to the one of PF (Dau & Sauer, 1996; Grabolle, 2005; Tsamaloukas, 2001) and peaks around 683 nm with a half width of 20 nm at room temperature (Dau, 1994). This suggests that both DF and PF are emitted from the same source, i.e. the same excited state(s) of the Chlorophyll a (denoted as Chl*) from the PSII antenna system. Whenever the Chl* population is increased due to a recombination process from the radical pairs, there are three possible ways the energy can be distributed (as introduced in Section 2.3.1).

The DF can be delayed on a time scale of ns to seconds after photon absorption by the antenna system. The repopulation of the Chl* in principle is governed by the differences of free energy between Chl* and different radical pair states, giving the DF intensity

$$F_D = S \cdot e^{\Delta G^*_{RP}/k_B T} \ , \qquad \textbf{(2.5)}$$

where S is a time independent sensitivity factor, determined by the amplification of the fluorescence detection system and the rate constant of fluorescence emission of the Chlorophyll (Grabolle & Dau, 2005); $\Delta G^*_{RP}$ refers to the Gibbs free energy difference between the given radical pair and excited chlorophyll (see scheme in Figure 2.2); $k_B$ is the Boltzmann constant; and $T$ is the absolute temperature in Kelvin. Therefore, the free energy difference between any two radical pair states can be resolved kinetically.

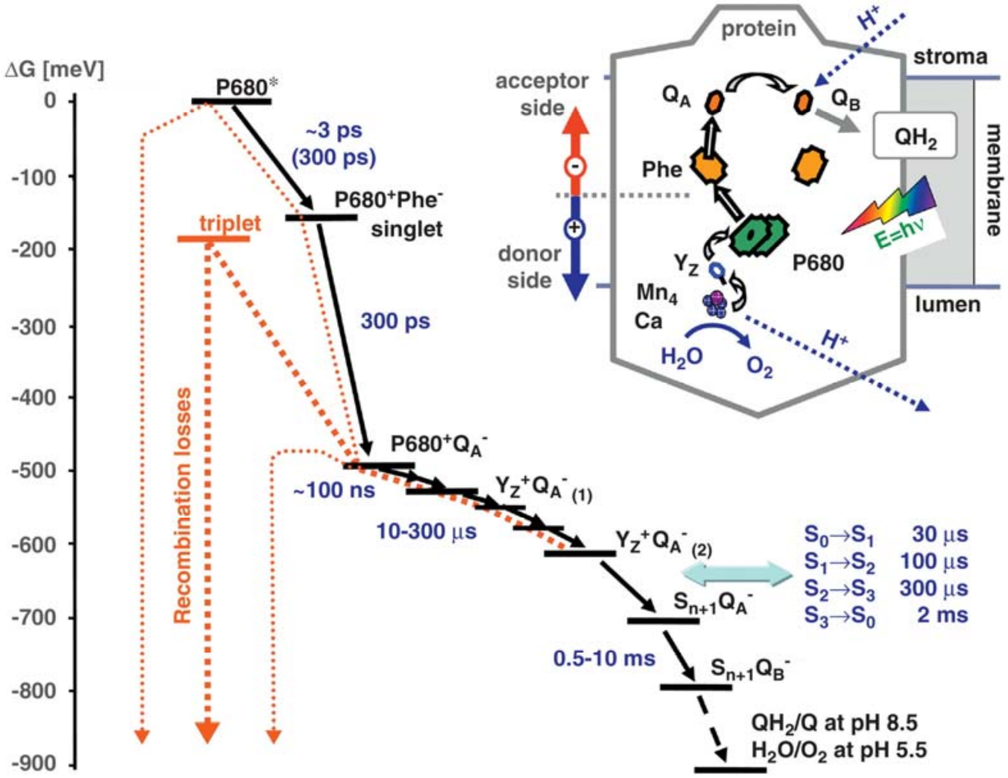

**Figure 2.2. The free-energy changes (Δ*G*) and time constants of the electron transfer reactions in PSII. Forward reactions are indicated by black arrows and charge recombination, as red-brown dotted lines. The Δ*G*-axis indicates the individual decays of all radical pair states formed after $P_{680}$* formation, in terms of free energy. The inset shows the arrangement of essential redox factors imbedded in the D1 and D2 protein subunits of PSII schematically, for details see (Dau et al., 2012).**

The intensity of DF signal can be expressed approximately by the population of oxidized P680 and reduced $Q_A$:

$$F_D = S \cdot e^{\Delta G^*_{RP}/k_B T} \left[ P_{680}^{\;+} \right] \cdot \left[ Q_A^{\;-} \right] \;, \tag{2.6}$$

where $\Delta G^*$ refers to the Gibbs free energy difference between the radical pair, $P_{680}^+Q_A^-$ and the excited chlorophyll state.

## 2.4.2 Data Acquisition of Delayed Fluorescence

For a delayed fluorescence (DF) measurement, the PSII sample particles (diluted in buffer) were pipetted into a cuvette and excited by saturating pulsed laser flash*[1] (see Table 2-4) with an intensity of 2 mJ/cm$^2$, a wavelength of 532 nm, and a full-width at half-maximum (FWHM) of 5 ns. The laser beam was aligned and widened by a group of lenses, yielding a homogeneous excitation area of 1 cm$^2$. The pulse intensity was determined and calibrated by a power meter*[2] (see Table 2-4).

The DF of highly active PSII membrane particles was measured in the time domain from 10 µs to 60 ms after each flash of a series of nanosecond laser pulses. Compared to the prompt fluorescence, the DF basically has the same emission spectrum, but a factor of about 100 lower in intensity (Buchta et al., 2007). The relatively strong PF emission is a fast process within less than 1 µs. Therefore, to avoid and filter the contribution from the PF in the detection system, a gated photomultiplier*[3] (see Table 2-4) was applied to detect the weakly delayed fluorescence signal. The shutter of the photomultiplier was in an open status but closed from 7 µs before to 3 µs after the laser flash during the detection. Possible scattered laser light was filtered by two long-pass filters*[4] (see Table 2-4), with a cut-off wavelength of 600 nm and 632 nm respectively.

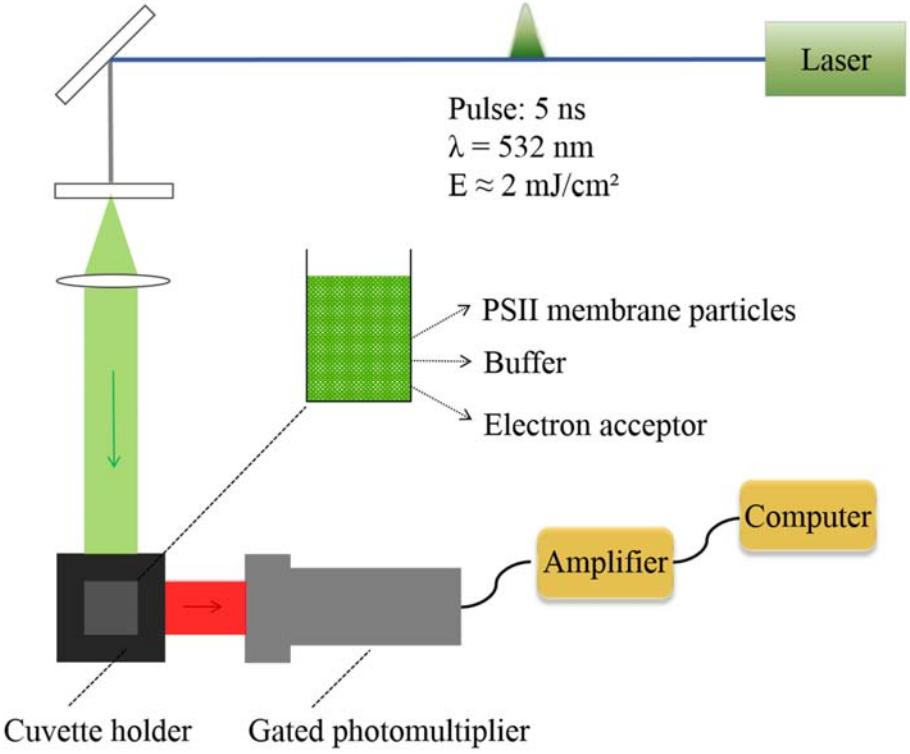

**Figure 2.3. Simplified scheme of delayed fluorescence setup. The PSII membrane particles (diluted in buffer with supplementary electron acceptor) were placed into a cuvette holder and excited by saturating pulsed laser flash with an energy of 2 mJ/cm$^2$, a wavelength of 532 nm, and a full-width at half-maximum (FWHM) of 5 ns. The laser beam was aligned and widened by a group of lenses, yielding a homogeneous excitation area. The delayed fluorescence was detected by a gated photomultiplier followed by an amplifier and data acquisition.**

It turned out to be a challenge to perform the analogue-to-digital (AD) conversion within the resolution limit, since the DF signal decayed by a factor of about $10^5$ from 10 µs to 56 ms. To cross this barrier, the signal was distributed into two channels, one (namely the slow channel) was guided through a preamplifier with an amplification factor of 30. See details of this solution in (Grabolle, 2005). Then both channels were coupled into an oscilloscope*$^5$ (see Table 2-4) and amplified. It was sampled at 1 MHz by a 12 bit PC card*$^6$ (see Table 2-4) from 200 ms before to 56 ms after the laser flash. The sampling rate resulted in a time resolution of 1 µs. Both channels were then merged into one decay, in which the range before 500 µs was from the fast channel while the one after 500 µs was from the slow channel. To reduce the number of data points, the size of the data file and the noise level, the decay was logarithmic averaged during the data acquisition process by a home-made program. The averaging resulted in a series of data points with constant spacing on a logarithmic time scale, giving 18 points per order of the signal decay. Specifically, 12 points from 200 ms to 5 µs before the laser flash, 15 points from 6 µs before to 10 µs after the laser flash and 70 points from 11 µs to 60 ms were acquired, resulting in a total number of 97 data points. It is worthwhile to note that, in the given detection resolution the DF signal after 10 ms was strongly interfered by 50 Hz noise, which likely came from the electricity power network.

**Table 2-4. Supplementary information of experimental setup of delayed fluorescence.**

| Experimental setup | Type |
|---|---|
| *[1] Laser | Continuum Minilite II |
| *[2] Power meter | Ophir Photonics, PE25-C |
| *[3] Gated photomultiplier | Hamamatsu R2066; PMT gated socket assembly C1392-55; Anode 1,000 V and Gating 250 V |
| *[4] Long-pass filters | DT-red and DT-magenta by Linos photonics |
| *[5] Oscilloscope | Tektronix AM502 |
| *[6] PC card | Adlink, PCI 9812 |

### 2.4.3 Data Analysis of Delayed Fluorescence

Scattering laser or strong PF emission from PSII particles can induce an additional fluorescence signal from the glass and cathode material of the photomultiplier. This additional signal was subtracted from the acquired DF transients, in a so called laser artefact correction as described in (Buchta et al., 2007; Grabolle & Dau, 2005).

In addition, according to Eq. (2.6) the decay of DF intensity was proportional to the population of $P_{680}^{+}$ and $Q_A^{-}$. Nevertheless, in the time range from 10 µs to 10 ms, the DF signal decays about three orders of magnitude while the PF decays only less than a factor of 4. It means that in the given time range, the DF signal was dominated by $P_{680}^{+}$. Equivalently, the contribution of $Q_A^{-}$ was smaller but not negligible. Hence a $Q_A$-correction was performed so that the decreased population of $Q_A^{-}$ was taken into account with the following equation, as developed earlier in (Buchta et al., 2007; Karge et al., 2014):

$$F_D^{corr}(t) = \frac{F_D(t)}{\left[Q_A^{-}\right]} = F_D(t)\left(\frac{F_M - F_0}{F_P(t) - F_0}\right) \quad , \tag{2.7}$$

where $F_M$ is the maximum and $F_0$ is the minimum of the PF signal. The $Q_A$ corrected DF signal is equivalent to

$$F_D^{corr}(t) = Se^{\Delta G^*_{RP}/k_BT}\left[P_{680}{}^{+}\right] . \tag{2.8}$$

To access the flash pattern, which was an indication of the oscillation cycle of S-state transition, the DF signal was analyzed at 2 ms (averaged from 1 ms to 3 ms). During the oxygen-formation step in the dark adapted samples induced by the third flash, the formation of an $S_4$ intermediate is a multiphasic process, coupled with proton movements from the manganese complex of PSII to the aqueous bulk phase and followed by the onset of O-O bond formation. To model the multiphasic process of the $S_3 \rightarrow S_4 \rightarrow S_0$ transition which involved three or more likely sequential steps, the DF time course excited by the third applied flash was simulated by a sum of three exponential functions by a least-square fit as following

$$F(t) = \left(\sum_{i=1}^{3} A_i \exp(-t/\tau_i)\right) + c \ . \tag{2.9}$$

The mean time constant of the transition $S_3$ to $S_4$, which is assigned to the deprotonation process (Haumann et al., 2005), is calculated as in (Buchta et al., 2007).

$$\tau_{mean} = \frac{\sum_{i=1}^{2} A_i \tau_i}{\sum_{i=1}^{2} A_i} \ , \tag{2.10}$$

while the Gibbs free energy of which, is calculated as

$$\Delta G = -k_B T \ln \frac{\sum_{i=1}^{3} A_i + c}{A_3 + c} \ . \tag{2.11}$$

The time constant $\tau_3$ is related to the electron transfer of the transition of $S_4$ to $S_0$, which is equivalent to the process of O-O bond formation, thus denoted as $\tau_{ox}$. Therefore, this method can provide, inter alia, quantitative insights in the functionally important inner-protein proton movements and electron transfer, which are coupled to a decrease of the free energy level, especially to the kinetics of the O-O bond formation step. In the end, by analyzing the prompt and delayed chlorophyll fluorescence, certain kinetics of the acceptor and donor sides as well as the free energy level between radical pairs (or intermediate states) can be resolved, see details in (Buchta et al., 2007).

## 2.5 Time-resolved Oxygen Polarography

Polarography is a common technique, invented by Jaroslav Heyrovsky from the Czech Republic back in 1922 and was rewarded with a Nobel prize in 1959 (Zoski, 2007). It can be classified as a branch of voltammetry, in which the characteristics of electrolysis between two electrodes can be studied by applying a polarized voltage and detecting the redox current.

### 2.5.1 Principle of Time-resolved Oxygen Polarography

In the current research methods, there are a few approaches to detect the oxygen yield (Renger & Hanssum, 2009). The ones used nowadays in the photosynthesis community can be classified into two types.

One is the Clark-type electrode, which was invented in 1953 (Renger & Hanssum, 2009); a recent detailed introduction can be found in (Baranov et al., 2004). It detects the absolute amount of oxygen molecules (after calibration, for instance taking reference from the oxygen diffusion in water) by a charged bare platinum electrode through a semi-permeable membrane which let through the oxygen but isolate the protein particles and the highly reduction active electrode surface. This is typically used in the detection of oxygen activity of the PSII membrane and core particles after preparation, also in this study mentioned in Sections 2.1.1 and 2.1.2. However, the time resolution is limited to the second(s) range (Baranov et al., 2004; Clausen et al., 2004; Renger & Hanssum, 2009).

Another one, the Joliot-type electrode (Joliot & Joliot, 1968) is able to detect the oxygen in a higher time resolution, functioning in a reaction rate of micro seconds (Lavorel, 1992) even though lacking the information of the absolute scale of oxygen yield (Bao & Burnap, 2015; Clausen et al., 2004; Dilbeck et al., 2012). Accordingly, from the time-resolved oxygen signal, the kinetics in sub milli-second range among intermediate states could be identified. The platinum (Pt), working as cathode, reduces the oxygen at the surface following

$$O_2 + 2H_2O + 4e^- \rightarrow 4OH^- . \qquad \textbf{(2.12)}$$

While the silver (Ag), working as anode, where the oxidation reaction takes place in a buffer solution with chloride irons and complete the second half of the chemical reaction cycle, according to

$$\mathrm{Ag} + \mathrm{Cl}^- \rightarrow \mathrm{AgCl} + \mathrm{e}^- . \qquad \textbf{(2.13)}$$

So the full reaction could be expressed as

$$4\mathrm{Ag} + 4\mathrm{Cl}^- + \mathrm{O}_2 + 2\mathrm{H}_2\mathrm{O} \rightarrow 4\mathrm{AgCl} + 4\mathrm{OH}^- . \qquad \textbf{(2.14)}$$

The reduction rate on the platinum is sufficiently fast given a potential voltage (-0.60 to -0.95 V) relatively to the anode and the oxygen yield is proportional to the accumulating electron charges (Hoff & Amesz, 1995). So the rate of oxygen yield is proportional to the floating and thereafter detecting redox current, i.e.

$$\frac{\Delta O_2}{\Delta t} \propto \frac{\Delta Q}{\Delta t} = I \ . \qquad \textbf{(2.15)}$$

## 2.5.2 Data Acquisition of Time-resolved Oxygen Polarography

The experimental setup was designed and engineered by Jung-Soo Kim in 2009, coordinated by Prof. Dau and constructed mainly in the workshop of physics department in Freie University Berlin. It was later on improved and optimised by Oliver Karge, Nils Schuth and Matthias Schönborn in the research group.

As shown in Figure 2.4, the flash was passed through an optical long pass filter*[1] and a liquid-light-guide*[2] in 3 meter length, with transmission close to 80% in the visible light range, i.e. between 400 nm to 700 nm from a Xenon flash lamp*[3] with maximum intensity of 4.5 J per flash and FWHM of 10 µs, and excited the PSII membrane particles which were deposited on top of the electrode surface after centrifugation in a swing bucket rotor*[4].

The polarization voltage was supplied and the redox current was detected by a home-made potentiostat through a higher pass filter (with two optional time constants, 0.1 and 1 second respectively), trigger by a Transistor-transistor-logic (TTL) pulse. See details of electronic layout in the diploma thesis of Kim Jung-Soo 2009 in physics department, FUB. At the output of the potentiostat, the signal was optionally amplified by a factor of 1 to 10 followed by a low-pass filter ranging from 0.1 kHz to 5 kHz and then analogue to digital processed by a multi-function data acquisition (DAQ)*[5] and recorded through a Labview program into the computer. From the program, certain key variable factors could be chosen as a specific value based on the individual experimental settings, such as the number of flash cycles, polarization time before measurement, recorded time before flash and additional time before specific flash number. The data was recorded in the rate of 1 MHz and then averaged over every 40 points, giving a resolution of 40 µs. Therefore, the reoxidation kinetics of the sub-millisecond to milliseconds range could be well resolved.

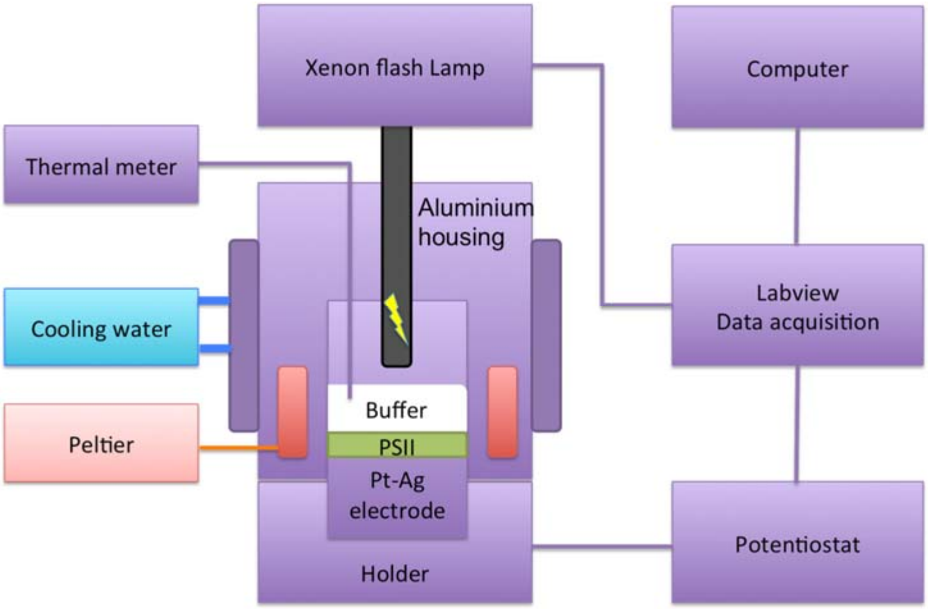

**Figure 2.4. Scheme of oxygen polarography setup. A layer of PSII membrane particles is deposited on the surface of a platinum/silver electrode by centrifugation. The electrode is placed onto the holder and connected to the potentiostat, from which a polarized voltage of -0.95 V is applied (platinum as cathode). The PSII is excited by a Xenon flash lamp through a Lightguide, which is positioned on top of the electrode. The electrode is covered by an Aluminium housing, which is thermally regulated by a pair of peltiers coupled with circulating cooling water. A sensor of thermal meter is placed within the buffer so that the real-time temperature of the PSII layer can be observed. The operational function is controlled by a Labview program, in which the trigger of flash lamp as well as the data acquisition is processed.**

The electrode was covered by an aluminium housing which is thermally synchronized by a pair of peltier elements*[6] with a precision of 0.1 °C coupled with a thermal sensor which was dipped into the buffer solution on top of the membrane particles without blocking the flash. Therefore, the temperature control and fluctuation of the sample could be observed during the whole experimental process. The final temperature uncertainty was estimated to be within ± 0.3 °C. And thanks to the closed environment and sufficient thermal conductivity between the electrode and peltier elements, the sample temperature could be regulated between -10 °C to 45 °C.

For each measurement, the PSII membrane particles were deposited in a platinum silver electrode by centrifugation (12,000 g, 12 minutes, 4 °C) forming a homogeneous thin layer (thickness in micrometres range) on top of the platinum and silver surface in order to minimize the diffusion time.

In this way, the kinetics could be resolved, without limited by the diffusion factor. A polarized voltage (-0.95 V) was applied onto the electrode 15 seconds prior to the trigger of flash in order to reduce all the containing oxygen molecules within the buffer. And then the sample was exposed to a series of single turnover flashes in a time spacing of 900 ms (otherwise specified). The data was recorded 20 ms before (as a baseline of the following signal) and 480 ms after the individual flashes respectively. A Gaussian function was fitted into each transient, giving a maximum value of the peak, which was proportional to the oxygen yield, therefore, resulting an oscillation pattern as a function of the flash number. Hence, by comparing the maximum value of the transient, for example after the third flash, the capability of oxygen production could be estimated.

The resulting data was labelled as arbitrary unit amplifying from converting the current that was proportional to the production rate of the oxygen (from water oxidation) into the voltage. Therefore, the corresponding oxygen volume produced equalled to the integral of the whole transient. Meanwhile, the peak of the transient is proportional to the scale of the volume. Kinetically, by having the time-resolved oxygen transients, one could get more insight into the multi-process from the $S_3$ to $S_0$, in which the deprotonation and electron transfer steps are coupled, relating to the most critical step, i.e. O-O bond formation.

**Table 2-5. Supplementary information of experimental setup of time-resolved oxygen polarography.**

| Experimental setup | Type |
|---|---|
| *1 Filter | OG 570, by ITOS, Germany |
| *2 Liquid-lightguide | Serie 380, by Lumatec, Germany |
| *3 Xeon flash lamp | FX 134, by EG&G Heimann Optoelectronics, Germany |
| *4 Rotor | HB-4, Sorvall, by Thermo scientific, USA |
| *5 DAQ | USB-6251 BNC, by National Instrument, USA |
| *6 Peltier element | PKE 72 A 0021, by Peltron, Germany |

### 2.5.3 Data analysis of Time-resolved Oxygen Polarography

To resolve the kinetics, the individual transient was fitted by a home-made simulation program, namely '$O_2$ diffusion' program written by Dr. Ivelina Zaharieva with brief introduction in a previous study (Dilbeck et al., 2012). The interface of the program is shown in Figure 2.5.

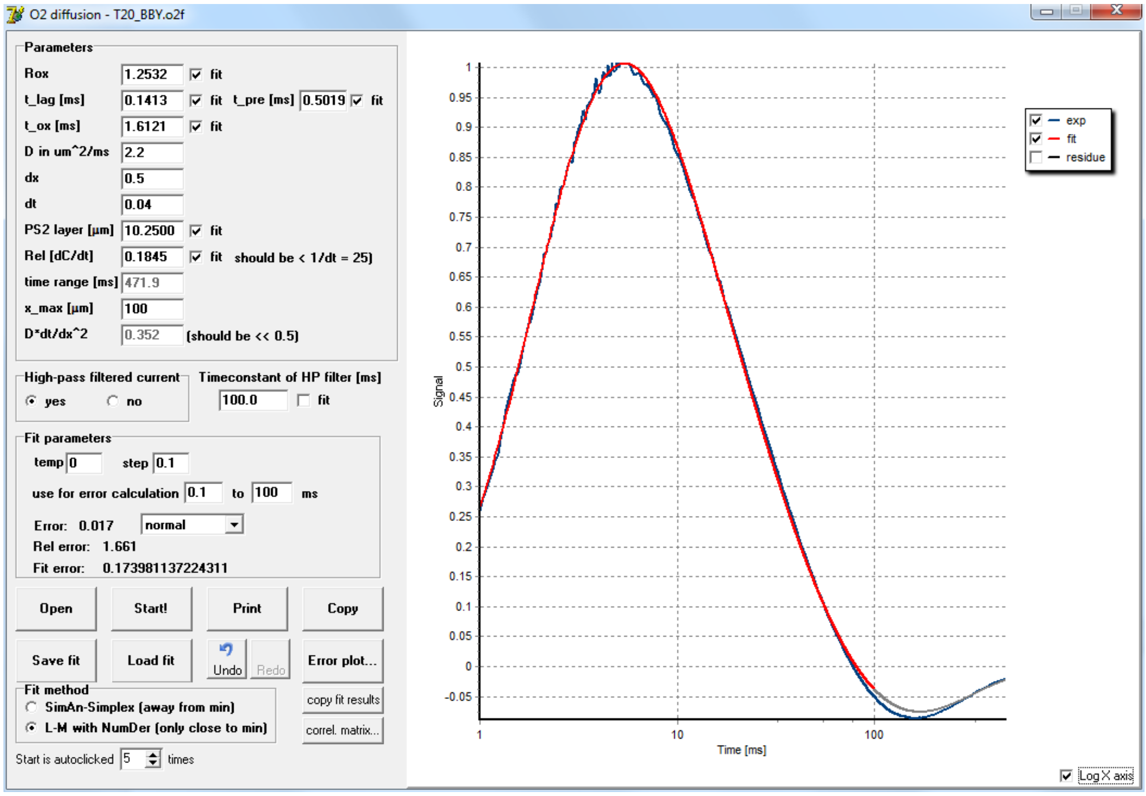
O2 diffusion - T20_BBY.o2f

Parameters
Rox 1.2532 ☑ fit
t_lag [ms] 0.1413 ☑ fit t_pre [ms] 0.5019 ☑ fit
t_ox [ms] 1.6121 ☑ fit
D in um^2/ms 2.2
dx 0.5
dt 0.04
PS2 layer [µm] 10.2500 ☑ fit
Rel [dC/dt] 0.1845 ☑ fit should be < 1/dt = 25)
time range [ms] 471.9
x_max [µm] 100
D*dt/dx^2 0.352 (should be << 0.5)

High-pass filtered current ● yes ○ no
Timeconstant of HP filter [ms] 100.0 ☐ fit

Fit parameters
temp 0 step 0.1
use for error calculation 0.1 to 100 ms
Error: 0.017 normal
Rel error: 1.661
Fit error: 0.173981137224311

Fit method
○ SimAn-Simplex (away from min)
● L-M with NumDer (only close to min)

Start is autoclicked 5 times

☑ exp
☑ fit
☐ residue

☑ LogX axis

**Figure 2.5. Interface of the oxygen diffusion program, simulating the transient detected from the oxygen polarography.**

Briefly, in this program a mathematical model (Lavorel, 1976, 1992) was implemented by dividing the sample volume (containing both PSII membranes and buffer) into discrete layers (thickness of *dx*) and taking into account:

(i) oxygen production from the PSII membrane layer;
(ii) oxygen diffusion in both PSII membrane and buffer layers (whole aqueous volume); and
(iii) oxygen consumption by the electrode from the very closest PSII membrane layer to the electrode surface.

The three processes above are then described by the following differential equations and then solved by numerically integration.

Firstly, after each single turn-over flash, the oxygen evolution is the result of water splitting through the $S_3$ – $S_4$ – $S_0$ transition as a function of time

$$\left[O_2\right]^{t}_{x=0} = \frac{k_1 k_2}{k_1 - k_2}\cdot\left[S_3^0\right]\cdot\left[e^{-k_2(t-t_{lag})} - e^{-k_1(t-t_{lag})}\right]\cdot\Delta t \ , \tag{2.16}$$

where $k_1$ is the rate constant between $S_3$ to $S_4$;

$k_2$ is the rate constant between $S_4$ to $S_0$;

[$S_3^0$] is the population of the PSII in $S_3$ state at t = 0;

$\tau_{lag}$ is the time delay of the onset; and

$\Delta t$ is the time discrete put into simulation, chosen to be 40 μs in this study.

Secondly, the oxygen concentration in the bottom layer (x = 0) is calculated by considering the diffusion from the layer above (x = 1)

$$\left[O_2\right]^{t}_{x=0} = \left[O_2\right]^{t-\Delta t}_{x=0} + \left(\left[O_2\right]^{t-\Delta t}_{x=1} - \left[O_2\right]^{t-\Delta t}_{x=0}\right)\cdot\left(\frac{D}{\Delta x}\right)^2 \Delta t \ . \tag{2.17}$$

Thirdly, the oxygen at the bottom layer consumed by the electrode

$$\left[O_2\right]^{t}_{x=0} = -R_{el}\left[O_2\right]^{t-\Delta t}_{x=0}\Delta x \ , \tag{2.18}$$

where $R_{el}$ refers to the characteristic speed of oxygen reduction of the electrode.

As a result, by combining the three equations above, the oxygen concentration at the bottom layer could be summed up as

$$\begin{aligned} \left[O_2\right]^{t}_{x=0} &= \left[O_2\right]^{t-\Delta t}_{x=0} + \left(\left[O_2\right]^{t-\Delta t}_{x=1} - \left[O_2\right]^{t-\Delta t}_{x=0}\right)\left(\frac{D}{\Delta x}\right)^2 \Delta t \\ &+ \frac{k_1 k_2}{k_1 - k_2}\left[S_3^0\right]\left[e^{-k_2(t-t_{lag})} - e^{-k_1(t-t_{lag})}\right]\Delta t - R_{el}\left[O_2\right]^{t-\Delta t}_{x=0}\Delta x \ . \end{aligned} \tag{2.19}$$

This simulation model applied to the oxygen transients of wild-type (WT) and mutants gave a very reasonable fitting results in previous investigations (Bao & Burnap, 2015; Dilbeck et al., 2012; Ishikita et al., 2006) and the study herein. Consequently, six key variables in total were taken into account for further analysis, including:

(1) $R_{ox}$, population of the [$S_3^0$], equivalent to the scale of oxygen evolution yield, proportional to the peak value of the transient;
(2) $R_{el}$, oxygen reduction rate of the electrode;
(3) $d$ [μm], thickness of the PSII membrane;
(4) $\tau_{lag}$ [ms], the time delay of the onset;
(5) $\tau_{pre}$ [ms], equivalent to $1/k_1$; and
(6) $\tau_{ox}$ [ms], equivalent to $1/k_2$.

It is noteworthy that in order to simplify the simulation process and minimize the degree of variables, the oxygen diffusion in water was assigned to be $2.2 \times 10^{-5}$ cm$^2$ s$^{-1}$ as a constant in this study, even though the actual value is relatively temperature-dependent, for example, ranging from $0.95 \times 10^{-5}$ cm$^2$ s$^{-1}$ to $3.05 \times 10^{-5}$ cm$^2$ s$^{-1}$ in the temperature between 0 $^o$C to 45 $^o$C (given $2.2 \times 10^{-5}$ cm$^2$ s$^{-1}$ in 30 $^o$C) (Han & Bartels, 1996). Nevertheless, this value was compensated and thus reflected by the oxygen reduction rate of electrode, i.e. $R_{el}$ in the given simulation model. The fit error was determined by the sum of squares deviation between the experimental data and the fit. It was a solid reference of the quality of the fitting results.

# Chapter 3 Ammonia Binding to the Water-oxidizing Manganese Complex of PSII

Complemented by additional information this entire chapter has been published as:

“Inhibitory and Non-Inhibitory NH3 Binding at the Water- Oxidizing Manganese Complex of Photosystem II Suggests Possible Sites and a Rearrangement Mode of Substrate Water Molecules”.

Nils Schuth#, Zhiyong Liang#, Matthias Schönborn, André Kussicke, Ricardo Assunção, Ivelina Zaharieva, Yvonne Zilliges, and Holger Dau (2017), Biochemistry 56(47):6240-6256.

# These authors contributed equally.

http://pubs.acs.org/doi/abs/10.1021/acs.biochem.7b00743

N. S. and Z. L. performed oxygen polarography experiments;

Z. L., performed fluorescence experiments;

M. S. and A. K. performed FTIR experiments;

R. A. performed Clark electrode experiments;

I. Z. wrote the simulation program of oxygen diffusion model;

Y. Z. performed cyanobacteria mutagenesis; and

N. S., Z. L., M. S., Y. Z. and H. D. co-wrote the article.

In the process of photosynthetic water oxidation, four accumulative oxidation states of the manganese complex are formed before the O-O bond formation and finally one dioxygen molecule is evolved. In the complex, one of the highly probable candidates as O-donor is oxygen five (O5) and either water one or two (W1 or W2) is likely to be the second donor. See Figure 1.4 in Section 1.2.2 for details. Because ammonia has similar electronic and structural characteristics as water, it is often used as a tool to study the catalysis of water oxidation in PSII. The atomic structure models of both ammonia and water can be seen in Figure 3.1.

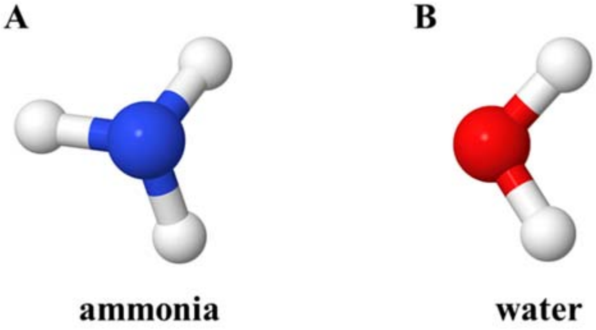

**Figure 3.1. Atomic structure model of (A) ammonia and (B) water molecule ($C_3H_8O_3$). The nitrogen atom is in blue, hydrogen in white and oxygen in red.**

Relevant studies have been reported since the 1970s, of which some show that ammonia inhibits the oxygen activity in PSII, while other studies show the opposite. Even though the detailed mechanism of ammonia-binding is not yet understood and it is unclear, whether ammonia or ammonium plays a bigger role. How does the binding affect the OEC and specifically the O-O bond formation kinetics? When does the binding take place and what is the binding site? Does the binding have an inhibiting or non-inhibiting effect on the oxygen evolution?

Some previous studies suggested, for instance, the oxygen inhibition by ammonia for various wavenumber ranges in an Fourier-transform infrared spectroscopy study (FTIR) (Tsuno et al., 2011), specific binding sites to the OEC at either O5 or W1 by NH3 (Navarro et al., 2013), a competitive binding in the chloride ion in the second sphere and then in the first sphere (Vinyard et al., 2016), binding to either W1 or W2 studied by X-ray free electron laser (XFEL) (Young et al., 2016).

Therefore, to understand the details in further step and answer the relevant open questions, the ammonia effects were investigated by time-resolved oxygen polarography (see details in Section 2.5), in which the kinetics of the O-O bond formation were observed in the range of micro- to milliseconds and the oxygen yield was compared numerically giving the same amount of the PSII centres.

In addition, to gain more insight about both the acceptor and donor sites, the variable prompt fluorescence (PF) and recombination delayed fluorescence (DF) techniques were also applied. See technical details in Chapter 2 Material and Methods. The reoxidation state and kinetics of both $Q_A$ and $Q_B$ (for instance electron transfer from $Q_A$ to $Q_B$) as well as the charge recombination due to the gradient energy difference from various radical pairs were resolved.

## 3.1 Experimental Details

The PSII sample was stored on ice in NaCl buffer. The PSII sample, additional NaCl buffer and ammonium buffer of equal pH (see detail composition in Appendix A.2) were pipetted onto the electrode right before the centrifugation (12000 g, 12 min, 4 °C) in a total volume of 375 µl. The amounts of both buffers were such that a chlorophyll concentration of 270 µg/ml (for $O_2$ polarography) or 10 µg/ml (for PF and DF) as well as the required ammonium concentration (0 - 120 mM) was achieved.

The PSII membrane particles were deposited on a bare platinum electrode by centrifugation of a Pt/Ag-electrode assembly, which was previously filled with PSII particles suspended in aqueous buffers containing $NH_4Cl$ and NaCl at various molar ratios. The concentrations of $NH_4Cl$ and NaCl were varied such that the sum concentration equaled 150 mM, resulting in a constant ionic strength and constant chloride concentration (of 170 mM chloride). For ensuring optimal intactness and long-term stability of the PSII particles, all buffers contained 1 M glycine betaine and all measurements were performed at 10 °C.

## 3.2 Results and Discussion

In previous studies, the inhibition of photosynthetic water oxidation by ammonium often had been investigated by detection of the rate of $O_2$ formation upon continuous illumination with light of saturating intensity. This approach did not allow for a discrimination between gradual inhibition resulting from slowing down of the $O_2$-formation step (increase in the time constant of $O_2$-formation, which typically is close to 2 ms), decreased S-state transition efficiencies (increased miss factor) and complete on/off inhibition of the photosystems. Moreover, the reactions of both $Q_A$ and $Q_B$ at the acceptor side of PSII also could affect the $O_2$-formation rates detected under continuous illumination in a potentially misleading way. To overcome those problems, I employed time-resolved $O_2$-polarography for excitation of PSII membrane particles by a sequence of saturating light flashes.

### 3.2.1 Ammonia Inhibition by Time-Resolved Oxygen Polarography

Since high-salt treatment has been used for removal of extrinsic PSII polypeptides and Mn depletion of PSII particles (Allakhverdiev et al., 1994; Blankenship et al., 1975), I performed in a series of control experiments to verify the absence of any deleterious effects of suspending PSII membrane particles in the buffer solutions of comparably high ionic strength and long storage time (Figure 3.2). It should be noted that a concentration of 150 mM NaCl corresponds to the concentration of monovalent salts that facilitates optimal functioning of PSII membrane particles, whereas lower or higher NaCl concentrations resulted in a moderate reduction of the quantum efficiency (increased Kok-cyle miss factor), a minor slow-down of $O_2$-formation at the PSII donor side, and significantly slower quinone oxidation at the PSII acceptor side (Karge et al., 2014).

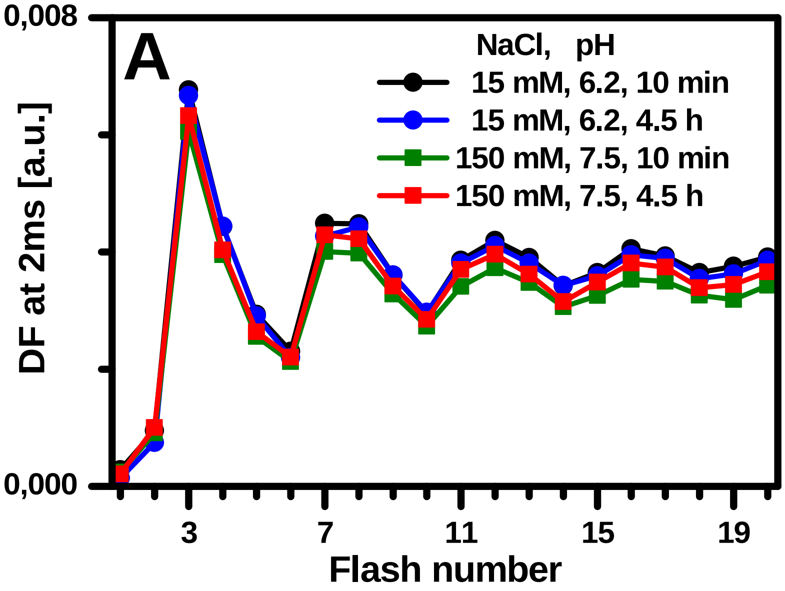

**Figure 3.2. The impact of high-salt and long-storage time on PSII oxygen evolution activity. It is compared in terms of flash patterns of the DF intensity at 2 ms (averaged from 1 ms to 3 ms after application of the saturating laser flash). The plant PSII membrane particles were stored either in low-salt, standard pH buffer (15 mM NaCl, pH 6.2) or high-salt, high-pH buffer (150 mM NaCl, pH 7.5) for 10 minutes or 4.5 hours respectively. The sample were stored on ice (ca. at 4 °C) in the dark and measured at 10 °C. The period-of-four oscillations were essentially identical verifying the absence of PSII degradation by prolonged storage in the high-salt buffers.**

Dark-adapted PSIIs were exposed to a sequence of saturating microsecond flashes of visible light spaced by 900 ms (provided by a Xenon flash lamp). Starting in the dark-stable $S_1$-state, a maximum of the $O_2$-formation yield ideally is observed on the 3rd, 7th, and 11th flash, due to synchronous cycling of the PSII donor side through its reaction cycle.

In the data shown in Figure 3.3B, the $O_2$-evolution maxima on the 7th and 11th are largely invisible because of exhaustion of the electron-acceptor pool of native plastoquinone molecules which are present in the preparation of PSII membrane particles (employment of an artificial electron acceptor is critical because of redox reactions at the bare metal electrodes). Figure 3.3A shows that (i) there is a clear ammonium inhibition and (ii) a major fraction of PSII (around 45%) remain uninhibited even at an ammonium concentration of 100 mM. The inhibition relates exclusively to the amplitude (or area) of the $O_2$-signal, whereas the time constant of dioxygen formation remains unaffected (unchanged rise time of the $O_2$-signal, Figure 3.3A). The partial inhibition effect might be explainable by (i) two different binding sites, with one inhibit and another one non-inhibit; (ii) differential binding, such that different binding effects at different time-points of S-state transition due to changing configurations of the OEC.

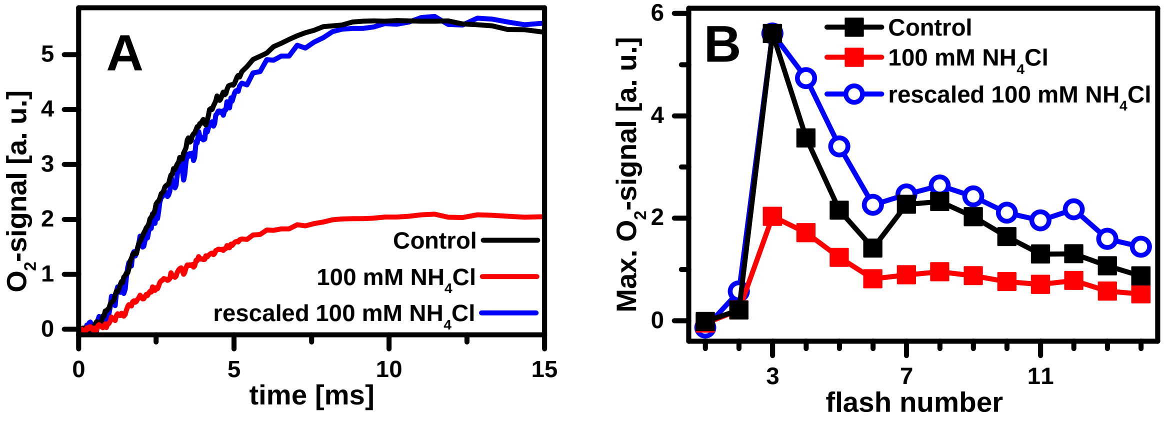

**Figure 3.3. Time-resolved detection of $O_2$-formation for PSII membrane particles driven through the water-oxidation cycle (S-state cycle) by sequences of saturating light flashes. (A) $O_2$-transients in the absence (control, black line) and presence (100 mM $NH_4Cl$, red line) of ammonium. Ammonium exposure reduces the amplitude of the shown 3rd flash transient; for visual comparison of the rise times, a rescaled transient is shown (blue line). (B) Amplitudes of the $O_2$ transients (reached at about 10 ms, see A) for flash sequences detected in the absence (black) and presence (red) of ammonium. To facilitate comparison of the damping of Kok-cycle oscillations of the $O_2$-formation yield, the amplitudes detected in the presence of 100 mM $NH_4Cl$ are also shown after rescaling (blue).**

Differential binding of ammonium to PSII in different S-state has been reported before, typically based on flash-sequence experiments with variations of the time period between flashes. In reference (Boussac et al., 1990), for instance, non-inhibitory ammonium binding in the $S_2$-state of the Mn-complex, clearly slower inhibitory binding in the $S_3$-state, and ammonium unbinding in the $S_1$-state was suggested, similar to results obtained in an earlier study (Velthuys, 1975). To assess whether slow ammonium binding affects the results of Figure 3.3, the flash spacing was varied from 150 ms to 30 s, for all flashes or individually for PSII poised either in the $S_2$-state or in the $S_3$-state (Figure 3.4). See corresponding flash pattern and oxygen transients in Figure 0.1 in Appendix. The influence of the increased flash spacing on the extent of ammonium inhibition is found to be insignificant. It suggests that, for the herein used experimental conditions and PSII preparation, inhibitory ammonium binding either is completed within clearly less than 1 s, with a characteristic time constant below 150 ms, or occurs already in the dark-adapted PSII ($S_1$-state).

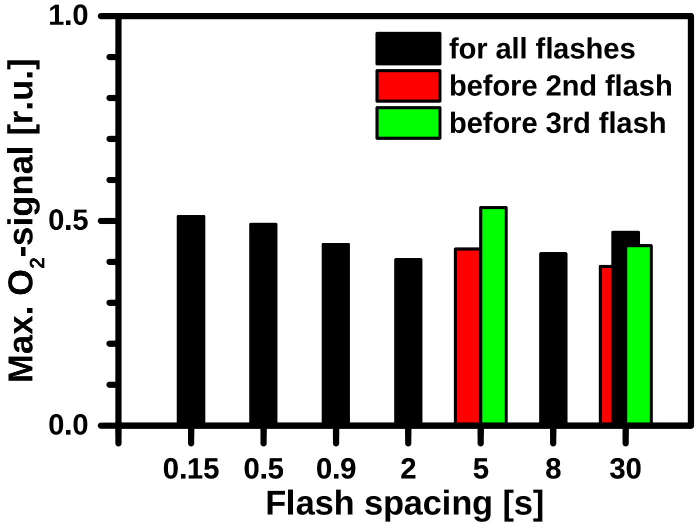

**Figure 3.4. Time-resolved detection of $O_2$-formation for PSII membrane particles driven through the water-oxidation cycle (S-state cycle) by sequences of saturating light flashes. Fraction of uninhibited PSII (at 100 mM $NH_4^+$) for variation of the flash spacing from 150 ms to 30 s. To minimize the influence of miss events, the $O_2$-signal amplitudes were averaged from 3rd to 6th flash (and normalized to the averaged amplitudes detected in the absence of ammonium for the same flash protocol). The colored bars indicate experiments where the flash spacing was increased specifically before the 2nd flash ($S_2$-state enriched, red) and before the 3rd flash ($S_3$-state enriched, green), but was 900 ms for all other flashes.**

### 3.2.2 Absence of Ammonium Influence on PSII Acceptor Side

The rate of oxygen evolution is affected not only by donor side processes, but also by the reaction kinetics of $Q_A$ and $Q_B$ at the acceptor side of PSII. However, in past research the inhibitory effect of ammonium often has been assessed using detection of the rate of $O_2$-formation under continuous illumination in the presence of an artificial electron acceptor by Clark-type electrode. That limits the possibility to distinguish acceptor and donor-side contributions. Therefore, in order to assess the acceptor side influence, I recorded changes in the yield of the PSII fluorescence.

Upon laser-flash application, the fluorescence signal first rises to a maximum value ($F_M$) followed by a multi-exponential decay that reflects the re-oxidation of the primary quinone acceptor, $Q_A$, by electron transfer to the secondary acceptor, $Q_B$, and possibly recombination of $Q_A^-$ with the 'hole' at the PSII donor side in PSII lacking bound $Q_B$ (at t > 100 ms). For the first flash applied to dark-adapted PSII, that $Q_A^-$ re-oxidation kinetics are not affected by $NH_4Cl$ addition, verifying the absence of $NH_4^+/NH_3$ influences on the PSII acceptor side (Figure 3.5). See Figure 0.2 for the corresponding 2nd and 3rd flash data in Appendix C.

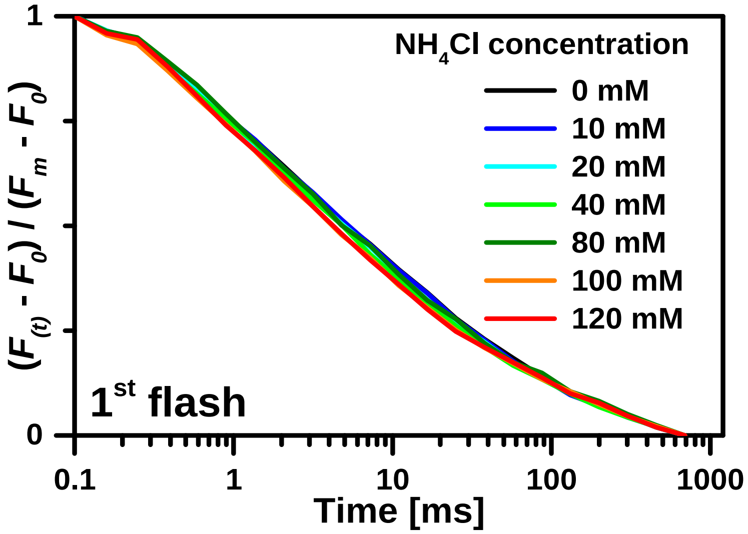

**Figure 3.5. Ammonium influence on acceptor side of PSII membrane particles assessed by detection of the variable PSII fluorescence yield (prompt fluorescence, PF). The PSII membrane particles were excited with sequences of 24 laser flashes spaced by 900 ms in a NaCl /$NH_4Cl$ buffer at pH 7.5. The PF time courses, which reflect the kinetics of the electron transfer at the PSII acceptor side, detected after the 1st flash applied to dark-adapted PSII.**

### 3.2.3 Ammonium Influence on Delayed Fluorescence

Time courses of the delayed PSII fluorescence (DF) emitted after laser-flash excitation were recorded and analyzed as described in (Buchta et al., 2007; Grabolle & Dau, 2005). In uninhibited PSII, a clear period-of-four oscillation pattern is typically observed for the DF intensity record within 0.5 ms to 5 ms after the laser flash, which is closely related to the flash pattern of oxygen evolution. The typical pattern of the 2 ms fluorescence observed in the absence of ammonium (black data points in Figure 3.6A) is increasingly modified upon exposure to ammonium. Period-of-four oscillations are still discernible but superimposed by a continuous rise in the fluorescence intensity that is indicative of PSII with a defective donor side. This rise is explainable by accumulation of the oxidized form of the redox-active tyrosine residue, which in PSII with a fully functional OEC is rapidly and completely re-reduced within milliseconds after laser-flash excitation. To reduce the influence of this rise, the difference in the DF level for two subsequent flashes was calculated. In the resulting flash pattern (Figure 3.6B) an oscillatory pattern is discernible also at higher flash numbers, but with a reduced amplitude suggesting that roughly half of the PSII undergoes S-state transitions also after the third flash and thus is not inhibited by ammonium exposure.

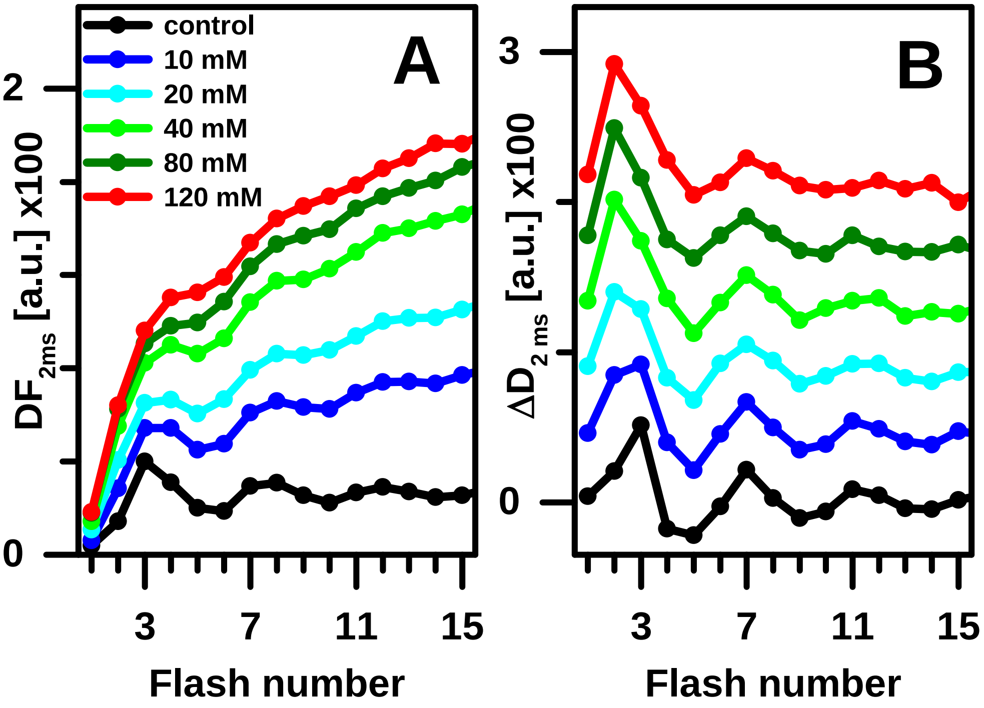

**Figure 3.6. Ammonium influence on donor side of PSII membrane particles assessed by detection of the recombination fluorescence transients (delayed chlorophyll fluorescence, DF). The PSII membrane particles were excited with sequences of 24 laser flashes spaced by 900 ms in a NaCl/$NH_4Cl$ buffer at pH 7.5. (A) Flash pattern of the DF intensity at 2 ms after the laser flash. (B) Differences of the DF intensities of subsequent flashes (vertical offset for clarity).**

The inhibition $K_M$-values determined for this rise after the 2nd flash and after the 24th flash are (30 ± 6) mM and (22 ± 2) mM (Figure 3.7A and B), evaluated by curve-fitting of the transients based on the standard equation for non-cooperative ligand binding (see Equation 0.1 in Appendix D). An ammonium influence is detectable already at 10 µs after the 1st laser flash and thus clearly before onset of the $S_1$-state to $S_2$-state transition (Figure 3.7C). This observation supports $NH_4^+$/$NH_3$ binding already in the dark-stable $S_1$-state, albeit possibly with reduced affinity. A binding constant ($K_M$) of (120 ± 50) mM is formally obtained. Note that, as opposed to the other $K_M$ values determined in this study, the value of 120 mM is highly uncertain as indicated by the large 1σ-confidence interval (67% likelihood) of ± 50 mM (2σ interval for 95% likelihood of ± 100 mM).

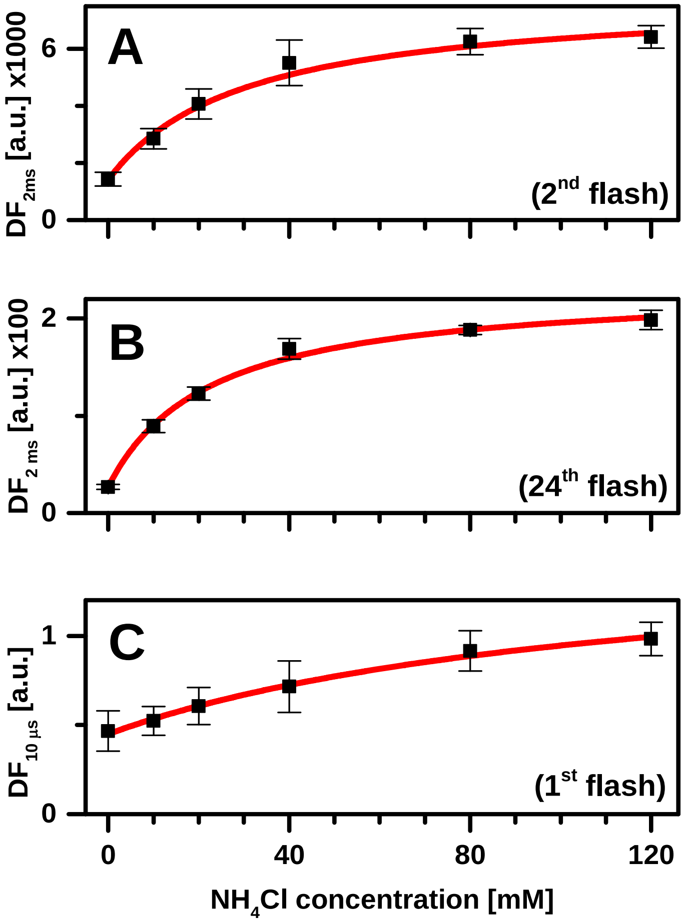

**Figure 3.7. Ammonium influence on donor side of PSII membrane particles assessed by detection of the recombination fluorescence transients (delayed chlorophyll fluorescence, DF). The PSII membrane particles were excited with sequences of 24 laser flashes spaced by 900 ms in a NaCl/$NH_4Cl$ buffer at pH 7.5. (A and B) Increase in DF at 2 ms after the 2nd and 24th flash with $K_M$ values of 30 ± 6 mM and 22 ± 2 mM, respectively. (C) DF at 10 µs after the 1st laser flash ($K_M$ of 120 ± 50 mM).**

The DF data facilitates the following conclusions:

(i) Not only in the time-resolved $O_2$-evolution experiment, but also for the changed experimental conditions of the DF experiment (film of highly concentrated PSII on bare platinum electrode versus highly diluted PSII particles in solution; with and without artificial electron acceptor), partial inhibition of advancement in the S-state cycle is observed; the $K_M$ of this partial inhibition is close to 25 mM in both experiments. Note that, the $K_M$ determined from the data of $O_2$-evolution is not shown herein, but with details in the published results (Schuth et al., 2017).

(ii) The rise of the DF intensity after the 2nd flash demonstrates that this transition is affected by ammonium exposure, even though the extent of electron transfer from the OEC to the tyrosine residue is unchanged.

(iii) The clear ammonium influence on the DF intensity detected 10 µs after the first flash suggests that either ammonium (or ammonia) binds already in the $S_1$-state to the OEC or the binding occurs within clearly less than 10 µs after the laser flash initiating the $S_1$ to $S_2$ transition.

### 3.2.4 Time-resolved $O_2$-evolution for Cyanobacteria with D1 Protein Variants

Recently, the ammonium binding has been investigated by advanced EPR spectroscopy combined with computational chemistry for PSII core complexes from *Thermosynechococcus elongatus,* for which crystallographic models of the PSII structure have been obtained (for *T. elongatus* or the closely related *T. vulcanus*) (Ferreira et al., 2004; Suga et al., 2017; Umena et al., 2011; Young et al., 2016; Zouni et al., 2001). The rate of substrate water exchange had been compared between control and ammonium-treated PSII by mass spectroscopic detection of the evolved dioxygen (Navarro et al., 2013), which has not provided any indications for a significant inhibitory effect of ammonium treatment. The contrasting results prompted me to compare ammonium binding in plant and cyanobacterial PSII.

I investigated the flash-induced $O_2$-formation for thylakoid membranes prepared from *T. elongatus* and a mesophilic cyanobacterium (S*ynechococcus* PCC 7002), where I analyzed the wild-type PSII and genetic variants containing only two of three D1 isoforms. In this series of measurements, the level of inhibition in the presence of 120 mM $NH_4Cl$ (at pH 7.5) was consistently close to the level observed in PSII particles prepared from spinach (Figure 3.8). In conclusion, partial inhibition of $O_2$-formation is observable for PSII from several organisms and also for various D1 isoforms of the cyanobacterial PSII.

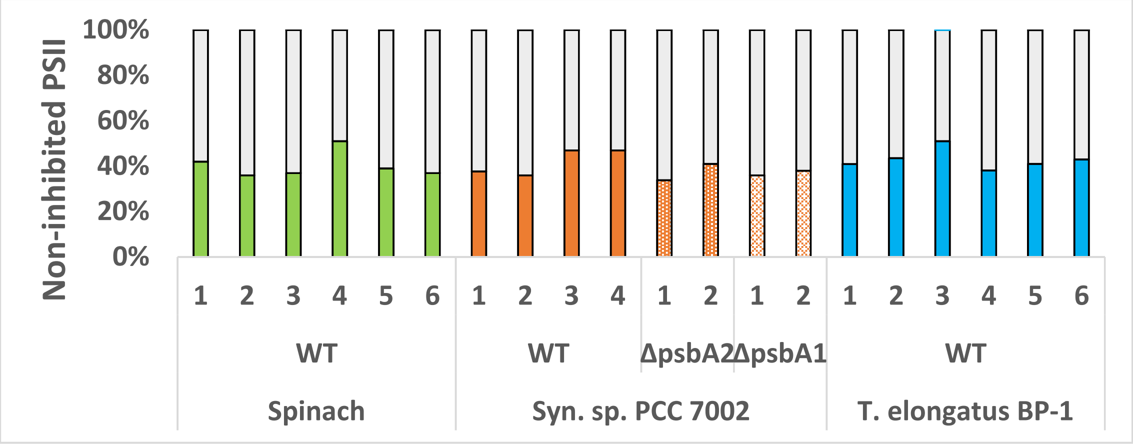

**Figure 3.8. Fraction of PSII from plants and various cyanobacteria that is not inhibited by 120 mM ammonium (at pH 7.5 and 10°C). To illustrate the extent of reproducibility, 6 replicas are shown for PSII from spinach, 4 replicas for a mesophilic cyanobacterium (*Synechococcus sp.* PCC 7002), 2x2 replicas for genetic variants of PCC 7002 lacking either the *psbA*1 or the *psbA*2 genes (multiple gene copies of the D1 protein of PSII), and 6 replicas for the thermophilic cyanobacterium *Thermosynechococcus elongatus* BP-1. After averaging the amplitudes of the $O_2$-evolution transients of the 3rd to 6th flash, the resulting values for PSII in 120 mM $NH_4Cl$ buffer were divided by the corresponding value in the absence of ammonium (in 120 mM NaCl buffer), to obtain the percentage of non-inhibited PSII for each investigated species.**

### 3.2.5 Anti-Cooperative Ammonia Binding Sites

The $K_M$-values for inhibitory $NH_4^+/NH_3$ binding are around 25 mM, but only about half of the PSII is inhibited at 120 mM ammonium. In addition, the FTIR experiment indicates non-inhibitory binding with a similar $K_M$-value, data not shown, with details in the work of M.S. (Schuth et al., 2017). To explain both partial inhibition and very similar $K_M$-values for inhibitory and non-inhibitory $NH_4^+/NH_3$ binding, an anti-cooperative binding mechanism is proposed. In a way that binding occurs either to the inhibitory site or to the non-inhibitory site, but within the herein considered range of ammonium concentrations, never to both sites simultaneously. The anti-cooperative binding model predicts one joint (identical) $K_M$-value for both sites; pronounced dissimilarities in the rate constants of binding to the individual sites would result in predominance of binding to one of the two sites and thus render the anti-cooperative binding experimentally undetectable. This model of anti-cooperative binding thus can explain the experimental findings only, if the two binding sites are similar regarding the rate constants for $NH_4^+/NH_3$ binding and unbinding.

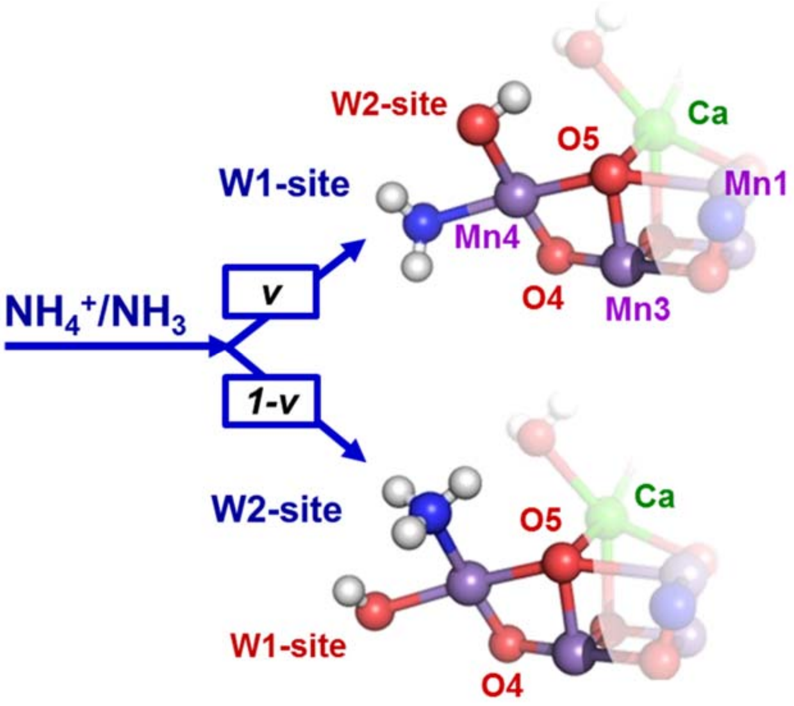

**Figure 3.9. Proposed model of anti-cooperative ammonia binding to the 'dangler manganese' (Mn4) of the $Mn_4Ca$-oxo cluster of photosystem II. Ammonia binds by replacing a water molecule either at the W1 site or at the W2 site. (In the upper scheme, the third ammonia hydrogen is hidden behind the nitrogen atom and thus not visible for the here used viewing angle.) The branching factor, ν, may depend strongly on experimental details, but was found, in the present investigation, to be always close to 50%. Binding at the W1-site (or W2-site) does not inhibit $O_2$-formation (non-inhibitory binding site), whereas binding at the W2-site (or W1-site) results in a complete blockage of the reaction cycle after reaching the $S_3$-state (inhibitory binding site). It is still unclear whether W1 or W2 represents the non-inhibitory ammonia binding site, but the balance of evidence is (slightly) inclined towards the W1-site.**

Spectroscopic, crystallographic and computational investigations support ammonia binding at either the W1 or the W2 site, both being water molecules (or hydroxide) coordinated to the same manganese ion, i.e. the 'dangler manganese' denoted as Mn4 (see Figure 3.9) (Navarro et al., 2013; Oyala et al., 2015; Schraut & Kaupp, 2014; Young et al., 2016). When comparing potential ammonia binding sites of the $Mn_4Ca$ cluster, anti-cooperative binding and similar binding kinetics are especially plausible for ammonia binding at the W1 and W2 site. Indeed, the calculated ammonia binding energies of these two sites are similar (Schraut & Kaupp, 2014).

Whether this assignment is fully robust against all conceivable complexities remains to be shown, especially in the light of the herein proposed anti-cooperative ammonia binding to the W1 and W2 site. In conclusion, the non-inhibitory ammonia binding to the W1 site is favoured by spectroscopic results, but assignment of W2 to the non-inhibitory binding site cannot be excluded fully definitively.

Diverging conclusion have been drawn regarding the inhibition of $O_2$-formation by $NH_3$ binding. Herein I report that for PSII membrane particles from spinach and thylakoid membranes from cyanobacteria with various copies of the D1 protein, consistently 55-65% of the PSII are inhibited by about 100 mM $NH_4Cl$ at pH 7.5 with a $K_M$ for inhibitory ammonium binding well below 100 mM. The proposed model of anti-cooperative ammonia binding renders it plausible that also comparably minor changes in experimental conditions (e.g. buffer composition and temperature, all the experiments were done at 10°C) could shift the ratio between inhibitory and non-inhibitory ammonia binding towards either less extensive or more complete inhibition, in close analogy (and possibly related) to variations of the equilibrium between the g2-form (Mn1 is a five-coordinate $Mn^{3+}$ ion) and g4-form (Mn4 is a five-coordinate $Mn^{3+}$ ion) of the $Mn_4Ca$-oxo cluster in its $S_2$-state.

## 3.3 Summary

The results and discussion presented in this chapter suggest that there may exist two anti-cooperative binding sites for ammonia to W1 and W2. Assuming only one of the water molecules is a possible candidate for the substrate water, this alternative binding mechanism would result in a partially inhibiting and partially non-inhibiting effect on the oxygen evolution activity (Figure 3.9).

In conclusion, the anti-cooperative binding model explains the herein reported results and reconciles many aspects of the large body of experimental results on ammonia binding to PSII reported since 1975. Several facets of the rich phenomenology are not covered by this two-binding-sites model. Also the relation of the two here discussed inhibitory and non-inhibitory binding sites to the four or even six $NH_4^+/NH_3$ sites suggested in early EPR studies remains partially unclear. Nonetheless, taking into account the complexity of the situation, also inhibitory ammonia binding at the W1 site cannot be excluded definitively at the present stage.

The above discussion implies that either W1 or W2, but not both, could be a substrate water molecule participating in O-O bond formation. However, also more intricate scenarios than the simple exchange of either W1 or W2 by $NH_3$ may be of relevance. A specific alternative option for non-inhibitory ammonia binding has been proposed by Brudvig, Batista and coworkers, inter alia supported by computational chemistry (Askerka et al., 2015; Vinyard et al., 2016).

All in all, the mechanism of O-O bond formation is one of the most challenging tasks in PSII study. The methods presented here do not yet fully cover all the possible perspectives in clarifying the details of the oxygen formation process. Thus, further studies are presented in the following chapters. In Chapter 4, glycerol is used as a hydrophilic cosolvent for PSII, to gain further insight, while in Chapter 5 the kinetics as well as the activation enthalpy of the O-O bond formation are discussed and compared among various species.

# Chapter 4 Glycerol Effects in Kinetics of Protonation and Electron Transfer of PSII

In protein dynamics, the folding and unfolding equilibrium in aqueous solution is affected by the addition of small organic molecules, such as methanol, ethanol and glycerol, which are known as cosolvents (Canchi & Garcia, 2013). Glycerol is often used in protein stabilization and prevention from aggregation (during refolding), while it orientates at the protein surface due to electrostatic interaction and thus slightly decreases the surface tension of water (Gekko & Timasheff, 1981). The atomic structure model of a glycerol molecule can be seen in Figure 4.1. The addition of glycerol into the protein environment may also affect the conformational coordinates and free energy level (Vagenende et al., 2009a). Glycerol is often used as a cryoprotectant, for instance during PSII purification procedures, to protect the protein from freezing damage due to ice formation and to preserve its activity of water oxidation. In the ground-breaking PSII crystal structure of Shen and coworkers, a few protein-internal glycerol molecules were resolved (Figure 4.2), in which the concentration of glycerol was 25% in the final buffer of their post-crystallization dehydration procedure (Umena et al., 2011).

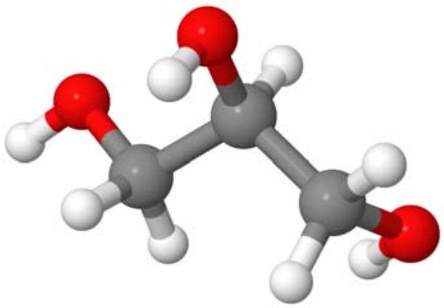

**Figure 4.1 Atomic structure model of a glycerol molecule ($C_3H_8O_3$). The carbon atom is in brown, hydrogen in white and oxygen in red.**

An electron paramagnetic resonance (EPR) study has suggested that glycerol can interact with the manganese cluster in intact PSII. Addition of glycerol caused a change in the spin state of the Mn cluster (Zimmermann & Rutherford, 1986). Increasing the viscosity, due to the addition of glycerol, has the potential to slow the rate of chemical reactions that are diffusion limited or involve large scale translational motion (Heimann et al., 2000). However, there is no electron or proton transfer reaction in PSII that is known to involve such a large-scale translational motion. Therefore, it is unlikely that an increase in viscosity alone can account for the decrease in PSII activity. Another study suggested that a glycerol content of more than 30% could cause inhibition of oxygen evoluting activity in intact PSII (Sachs et al., 2003). Surprisingly, in photosystem I (PSI) glycerol is able to directly bind inside the protein, thus interfering with the protein function (Hussels & Brecht, 2011b). In another PSI study, it was shown that the protein prepared in glycerol/buffer mixtures yields a high homogeneity for all chromophores. This indicates a more compact protein conformation but less structural variability (Hussels & Brecht, 2011a). This poses the question whether the same effect could be observed in PSII.

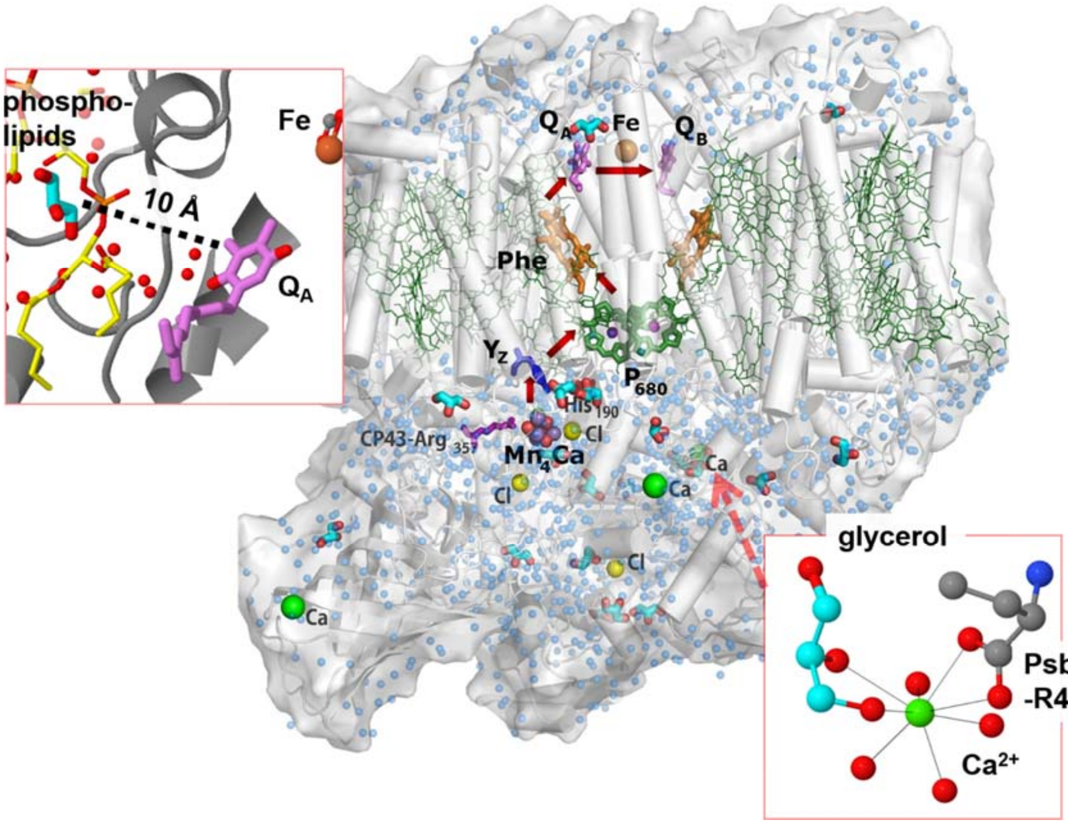

**Figure 4.2. PSII crystal structure and glycerol molecules resolved at 1.9 Å resolution (Umena et al., 2011). Crucial redox cofactors are indicated, including the primary electron donor ($P_{680}$), the primary pheophytin acceptor (Phe), the primary ($Q_A$) and secondary ($Q_B$) quinone acceptors, and at the electron donor side, a redox-active tyrosine ($Y_Z$), the inorganic $Mn_4Ca(\mu\text{-}O)_n$ core of the protein-bound Mn-complex. Additional Ca ions (light green) are also shown. Water molecules resolved in the crystallographic model are shown as blue spheres. The glycerol molecules are presented with two colors: light blue (carbon atoms) and red (oxygen atoms).**

Therefore, it is of fundamental interest to understand how glycerol may affect individual reaction steps in PSII, especially in the water oxidation process. It could help discover more details of the O-O bond formation.

In this study, I investigated how the glycerol affects individual reaction steps in PSII by analyzing time courses (after ns-laser flash excitation) of delayed fluorescence (10 μs - 10 ms, DF) and by analyzing the prompt fluorescence yield (100 μs - 700 ms, PF). The PSII membrane particles were isolated from spinach and supplemented by DCBQ as electron acceptor. The study focuses on:

(1) the oxygen evolution step ($S_3 \rightarrow S_4 \rightarrow S_0 + O_2$) at the donor side, and

(2) the electron transfer between $Q_A$ and $Q_B$ at the acceptor side of PSII.

## 4.1 Experimental Details of Sample Preparation

As introduced in Section 2.1.3, the PSII particles (namely BBY) were calibrated into a chlorophyll concentration of 100 μg/ml as stock solution in the control buffer (buffer D) and stored on ice until used for the fluorescence measurements. Right before the measurement, the particles were diluted to 10 μg/mL chlorophyll in an optical one-way cuvette (optical length of 1 cm) using a mixture of buffer D and glycerol buffer (67% v/v, see table of buffer composition in Appendix A.2.1) and supplemented with artificial electron acceptor DCBQ (20 μM). The content of glycerol in the buffers was varied, resulting in glycerol/buffer ratios of 0 to 50% (v/v) with an increment of 5%. It should be noted that the glycerol buffer has the same composition as buffer D, but with additional glycerol content. The DCBQ was dissolved in DMSO in a stock concentration of 4 mM and stored in 1 mL reaction tubes in -20 $^{o}$C fridge up until one hour before starting the measurement.

## 4.2 Results and Discussion

### 4.2.1 Kinetics of Protonation and Electron Transfer Affected by Glycerol on Donor Side

The PSII enriched thylakoid membrane fragments (BBY) were detected by both prompt fluorescence (PF) and delayed fluorescence (DF) measurements in a buffer solution containing 0 to 50% glycerol at pH 6.2 at room temperature (20 $^{o}$C ± 1 $^{o}$C) after saturating laser flashes. It is worthwhile to note that higher concentrations of glycerol were also tested (up to 60% glycerol, data not shown) but it was hard to fully dissolve DCBQ in those solutions with the given approach.

The resulting time courses of the DF intensity from the first to the fourth flash respectively are shown in Figure 4.3, in which only the control (0%) and 50% glycerol conditions are plotted in order to highlight the differences between both extreme conditions. Starting from 10 µs, the DF intensity is increased by the glycerol treatment for all four flashes.

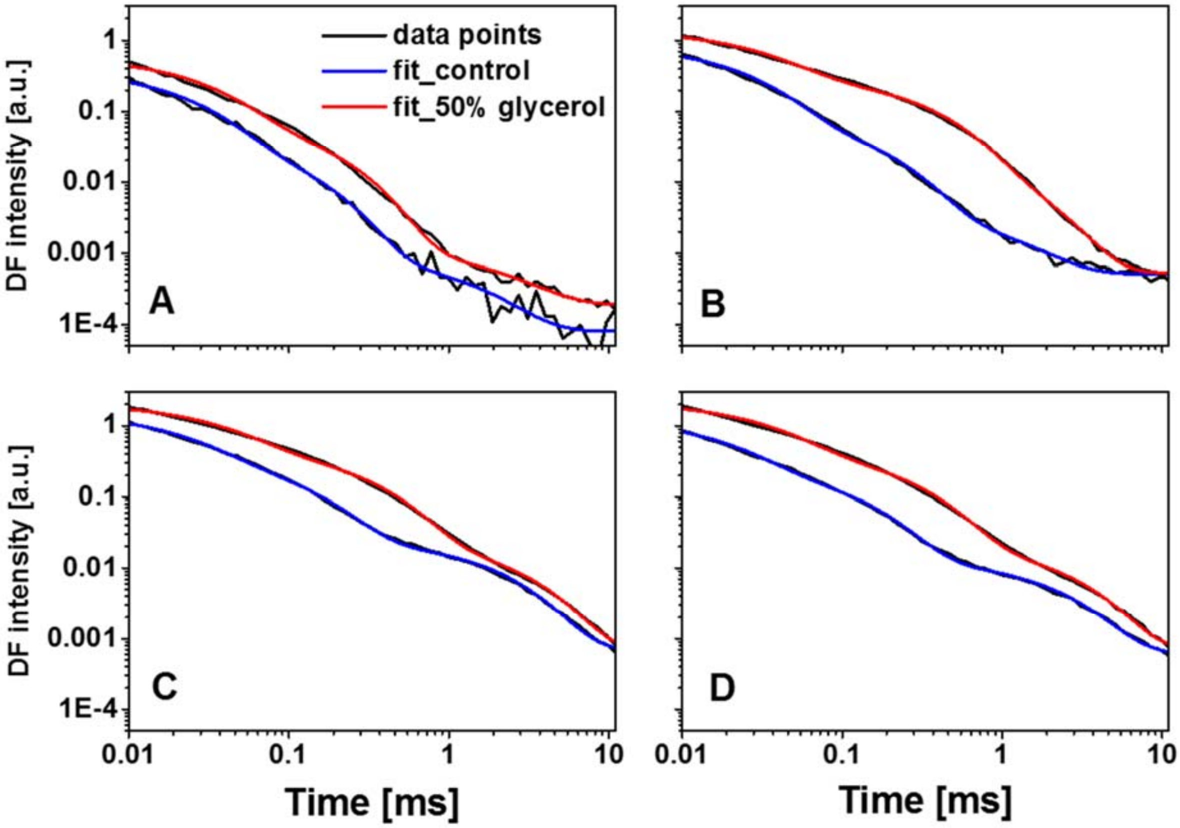

**Figure 4.3. The time course of DF decay on a double logarithmic scale of PSII enriched membrane fragments after the first to fourth (panel A to D) saturating laser flash (pH 6.2, 20 °C). The data points are shown in black, the fit of the control, i.e. 0% glycerol in blue and the fit of the 50% glycerol sample in red. All shown data are the average of six repeated measurements.**

For the first and forth flash, the DF decays of the glycerol treated and the glycerol free PSII are quite similar to each other kinetically (Figure 4.3A and D). These two decays correspond to the $S_1$ to $S_2$ and $S_0$ to $S_1$ transitions of the Kok cycle. However, the kinetics are strongly affected after the second and third flash, which correspond to the $S_2$ to $S_3$ and $S_3$ to $S_0$ transitions, respectively. The mechanisms of these two steps, i.e. $S_2$ to $S_3$ to $S_0$ are still highly under debate, since the crystal structures of individual states are not yet well resolved. Nevertheless, two favourable mechanisms are highly discussed as introduced in Sections 1.2.2 and 1.2.3. Therein the Kok cycle is introduced, presenting both of the $S_2$

to $S_3$ and $S_3$ to $S_0$ transitions, which cycle through alternative proton and electron transfer. Therefore, these significant kinetic effects from the treatment of glycerol may help to further understand the protonation and electron dynamics in the corresponding critical steps.

In order to highlight the effects from glycerol in the $S_3$ to $S_0$ transition, the DF decay after the third saturating flash is presented in Figure 4.4, including the treatments in all glycerol concentrations performed in this study, i.e. from 0 to 50% with an increment of 5%.

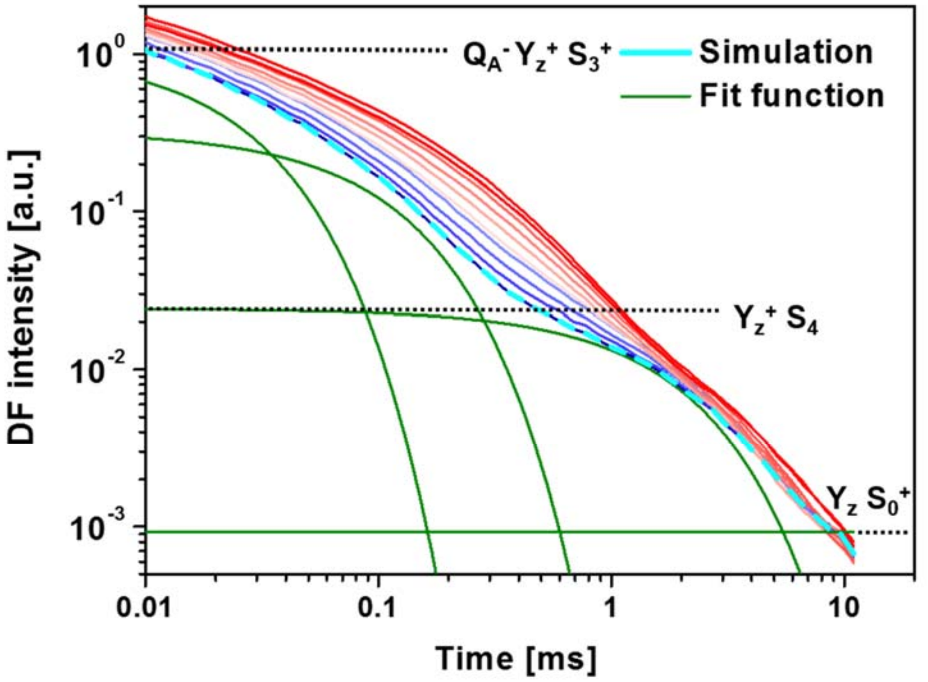

**Figure 4.4. The time course of DF decay (10 µs to 10 ms) on a double logarithmic scale after the third laser flash (pH 6.2, 20 °C), simulated with a sum of three decaying exponential functions. The gradient blue and red colors refer to the detected DF intensity in various glycerol concentration treated PSII particles (from 0 to 50%, left to right orientation following dark blue, light blue, light red to dark red), while the cyan dotted curve is the simulation of the control measurement (0% of glycerol) and green ones stand for the fit function of each exponential factor plus the constant offset. The dotted black lines are the assignments to the corresponding intermediate radical pairs state following the free energy decay. The signals are averaged over six repeated measurements in each condition.**

In Figure 4.4, the presence of glycerol alters the time course of the DF transients significantly with a gradient concentration dependence from 0 to 50%. The Gibbs free energy can be seen from the DF decay by dropping approximately two orders of magnitude during the transition $Y_Z^+S_3^+ \rightarrow Y_Z^+S_4$. To evaluate the kinetics of the fast (denoted as $\tau_{mean}$) and slow phase ($\tau_{ox}$) quantitatively, a tri-exponential function is fitted to the time courses, as introduced in Section 2.3.3. The fit parameters from the fitting functions are listed in Table 0-1 (Appendix D). The two fast phases correspond to the free energy difference between the $Y_Z^+S_3$ and $Y_Z^+S_4$ state while the slow phase refers to the one between $Y_Z^+S_4$ and $Y_ZS_0$ state.

In the kinetics of the control sample (glycerol free), a value for $\tau_{mean}$ of 42 µs and for $\tau_{ox}$ of 1.72 ms were obtained (Figure 4.5). Both values are in line with previous studies, in which they were reported as 41 - 49 µs and 1.7 ms respectively for spinach PSII (Grabolle, 2005; Zaharieva et al., 2013). The $\tau_{mean}$ is a mean weighted valued life time calculated according to Eq. (2.10) taking into account both fast phases from the tri-exponential function. It corresponds to the deprotonation step (Buchta et al., 2007). The deprotonation process is linearly decelerated by increasing glycerol concentration from 42 µs (in control) to 91 µs (in 50% glycerol). It suggests that the glycerol, as a co-solvent, may perturb the water molecules, for instance in the second sphere around the manganese complex, thus altering the proton channel(s). This is likely because in aqueous form, all three hydroxyl groups of glycerol are involved in intramolecular hydrogen bonding (Mario Pagliaro, 2010). For detail studies of the proton channels, see examples in (Shoji, Isobe, Yamanaka, et al., 2015; Wraight, 2006).

Alternatively, the observed decelerated deprotonation process may come from the modified protein-protein interaction by glycerol, as suggested in a study in which the oscillation pattern of proton release (in core particles) is enhanced by addition of glycerol (Haumann et al., 1997). The glycerol addition causes a change in protonation dynamics even in small concentrations (for example 5% of glycerol) likely due to high sensitivity of PSII core particles compared to BBY. This is a sign that the proton path is more sensitive to the hydration of the protein in the aqueous environment, as a result of the change of hydration state by glycerol (Davis-Searles et al., 2001).

In contrast to $\tau_{mean}$, $\tau_{ox}$ refers to the electron transfer coupling to the O-O bond formation. It stays at a relatively consistent level (ca. 1.7 ± 0.1 ms) up to 30% glycerol, though starts to decelerate in higher glycerol concentration, for example up to 2.2 ms in 50% glycerol (Figure 4.5B). It suggests that the O-O bond formation is stabilized and even stimulated within 30% glycerol, but in contrast, it is inhibited at higher concentration. This biphasic behaviour is reported in the study of glycerol effects on PSII oxygen evolution, in which the transition point is also 30% glycerol, as determined by steady state oxygen activity (Sachs et al., 2003).

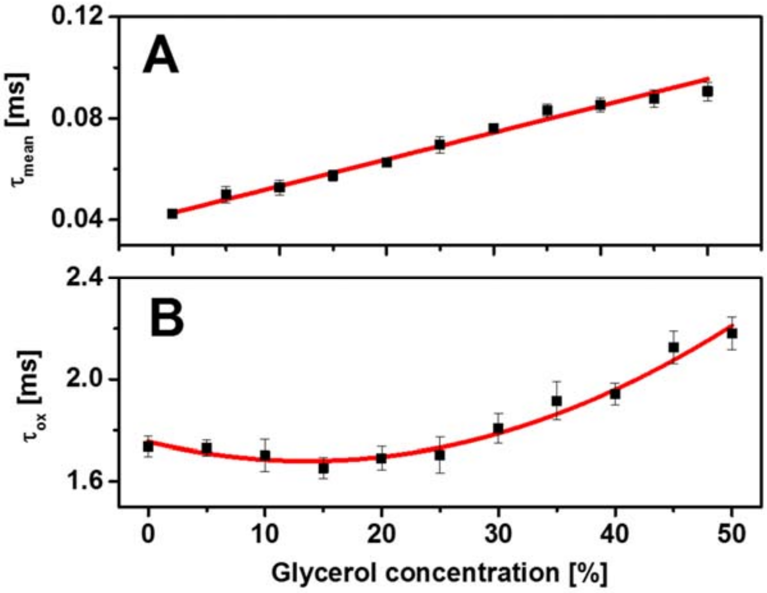

**Figure 4.5. The time constants of $\tau_{mean}$ and $\tau_{ox}$ as a function of glycerol concentration. The shown data are simulation results based on a tri-exponential function from Figure 4.4. (A) The mean time constant of the two fast phases correlating to the $S_3$ to $S_4$ transition and (B) the time constant of the slow phase, correlating to the $S_4$ to $S_0$ transition. The error bars represent the standard deviations of the repeated measurements.**

It is worthy to address that the deprotonation process prior to the formation of intermediate state $S_4$ is found to have a life time of up to 200 µs, as determined by various approaches (Gerencser & Dau, 2010; Haumann et al., 2005). Comparably, the time constant $\tau_{mean}$ discussed in this section and determined as 40 µs is not the deprotonation life time, but highly correlated to it.

Even though the kinetics of the proton and electron transfers are decelerated in presence of glycerol, the efficiency of the S-state transition is not highly affected even by 50% glycerol (Figure 4.6). Panel A of Figure 4.6 shows a flash pattern of the DF intensity at 2 ms (by averaging from 1 to 3 ms), a time scale at which the pattern reflects the redox state of the Mn-complex. The quaternary damping oscillation pattern of the control (0% glycerol) represents a typical Kok cycle with maximum at the 3rd, 7th, and 11th flashes respectively. It indicates a reasonable good level of efficiency, i.e. low miss factor (Karge et al., 2014). Assuming no double hit, a constant miss factor between each state transition and the distribution of $S_0$ and $S_1$ states in the dark-adapted PSII, the patterns are fitted by a matrix model as introduced in Section 1.2.2. It results in a series of miss factors in each glycerol condition with a minimum miss factor of 9%. Prior to the first flash, the initial population of $S_1$ state is close to 100% compared to the negligibly small population of $S_0$ state. Experimentally, in dark-adapted conditions, all OECs are presumably in the $S_1$ state since the $S_2$ and $S_3$ states are reduced by both tyrosine D, $Y_D$ from D2 protein (fast phase) and $Q_B^-$ from acceptor side (slow phase) while $S_0$ is oxidised by $Y_D^{ox}$ to $S_1$ state (Messinger et al., 1993; Rutherford et al., 1984; Styring & Rutherford, 1987). The high population of the fully dark-stable $S_1$ state, can be attributed to extensive dark adaptation during preparation of PSII membrane particles and washing-steps in low-salt buffer solutions. This is in line with a previous fluorescence study where the dark-adapted PSII particles were mostly in the $S_1$ state (Karge et al., 2014). The miss factors and initial populations of $S_0$ and $S_1$ states from the fit parameters can be seen in Table 0-2 (Appendix D). Accordingly, the quantum efficiency (η) of the S-state transition was determined by subtracting the miss factor (α) from unity, i.e. $\eta = 1 - \alpha$ (Figure 4.6B).

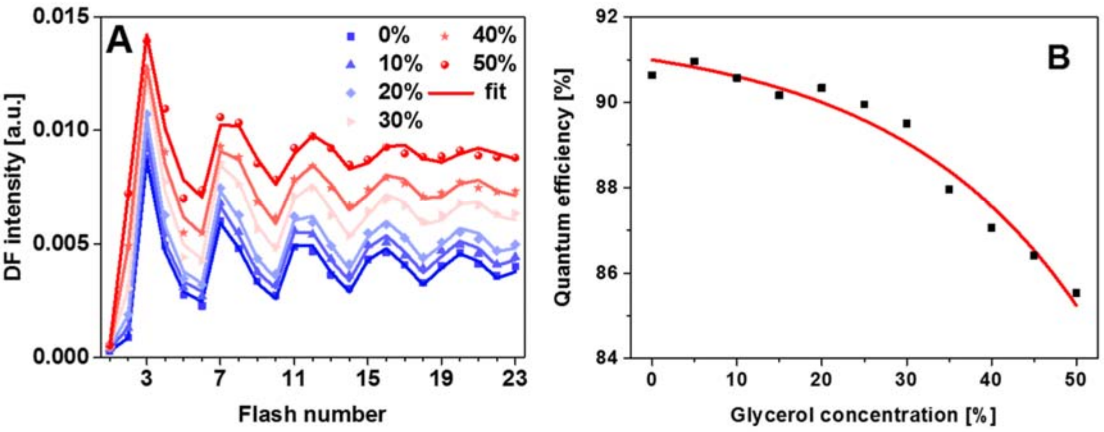

**Figure 4.6. Quantum efficiency of the S-state transitions in presence of glycerol. (A) Flash number dependence of DF intensity at 2 ms phase (by averaging from 1 to 3 ms) after saturating flashes were applied to the dark adapted PSII membrane particles. The dots are the experimental data while the lines are the fit. The data were fitted from the 3rd to 23rd flash applying a matrix model by considering a double hit rate of zero and initial populations of S0 and S1 in the dark-adapted state. The model details are introduced in Section 1.2.2. (B) Glycerol concentration dependence of the S-state transition efficiency, which is equivalent to subtracting the miss factor (obtained from the fitted oscillation pattern in panel A) from unity.**

The control (0% glycerol) shows an efficiency of about 91%, equivalent to a miss factor of 9%, which is consistent with the best known performance of PSII membrane particles with a miss factor of 8 - 10% (Buchta et al., 2007; Isgandarova et al., 2003; Karge et al., 2014). The factor is highly dependent on, amongst others, the protein environment, temperature, pH value and cosolvents. The efficiency of the S-state transition is still as high as about 85% in 50% of glycerol, which suggests that although the high concentration of glycerol may further perturb the water molecules around the Mn-complex, thus decelerating both proton and electron transfer, it does not significantly inhibit the redox reactions of the Tyrosine Z ($Y_Z$) (Figure 4.3). In comparison, the efficiency of oxygen evolution can be highly decreased down to 50% in 50% glycerol when the 18- and 24-kDa extrinsic proteins are lost (e.g. by washing in high salt buffer), as a result of increasing access of glycerol to the catalytic site (Halverson & Barry, 2003). See detail protein structure in Figure 1.2 of introduction section.

It is noteworthy to address that the miss factor is strictly S-state dependent, specifically with higher misses in $S_2$ to $S_3$ and $S_3$ to $S_0$ transitions compared to lower values in the other two transitions (Pham & Messinger, 2016). It may because of higher energetic barriers when two substrate water binds to the Mn-complex during $S_2$ to $S_3$ and $S_3$ to $S_0$ transitions, respectively. However, it is not the focus of this study, since the glycerol has no strong impact on the miss factor.

In addition to the quantum efficiency of S-state transitions, the free energy level is also influenced by glycerol treatment. It can be seen in Figure 4.4 that starting at 10 µs after photoexcitation the DF intensity is altered by the glycerol treatment. This fluorescence intensity correlates to the the free energy level of the recombination of the radical state of $Q_A^-Y_Z^+S_3^+$. Since the DF mechanism is based on Boltzmann distribution between various free energy levels formed by different radical pairs, it is important to address that not only the kinetics but also the Gibbs free energy levels (of intermediate formation) are slightly affected by glycerol treatment (Figure 4.7). It suggests that the glycerol potentially alters the interior protein environment and likely shifts the free energy level of the radical pair state $Q_A^-Y_Z^+S_3$ thus increasing the probability of charge recombination. Even though the glycerol influence on the exterior protein environment cannot be excluded fully definitively.

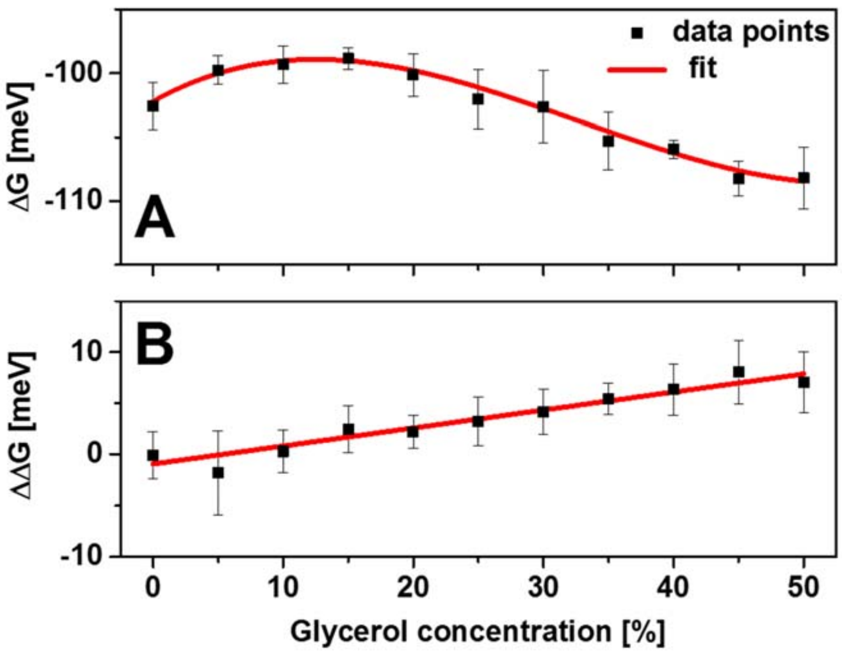

**Figure 4.7. The glycerol concentration dependence of the Gibbs free energy between the radical pair states $Q_A^-Y_Z^+S_3$ and $Y_Z^+S_4$. The free energy is determined based on (2.11). (A) The Gibbs free energy, fitted in a parabolic function (red line). (B) The difference of Gibbs free energy compared to the control (glycerol-free PSII), fitted in a linear regression.**

The free energy difference between the intermediate states $Q_A^-Y_Z^+S_3$ and $Y_Z^+S_4$, is determined based on Eq. (2.11). The biphasic phenomenon with a transition point at 30% glycerol also fits the one of the electron transfer (Figure 4.4B). The energy level is only slightly altered from -102 to -108 meV in 0% and 50% glycerol respectively (Figure 4.7A). The given value in the control condition is in line with the previous study, in which, a value of -104 meV is determined at pH 6.4 at room temperature (Grabolle, 2005; Haumann et al., 2005).

In addition to the most critical step of $S_3$ to $S_0$ transition, the dynamics of proton and electron transfers of the $S_2$ to $S_3$ transition after the second flash are also significantly decelerated due to glycerol addition (Figure 4.8). The deprotonation is followed by an electron transfer with a life time of about 30 µs and 300 µs respectively (Klauss, Haumann, et al., 2012). Similar to the approach discussed in the $S_3$ to $S_0$ transition (Figure 4.4, page 53), a sum of three exponential functions is fitted to the time courses of Figure 4.8 but from 0.01 ms to 2 ms, since the kinetics of the transfers are about five times faster than the $S_3$ to $S_0$ transition (fitted from 0.01 ms to 10 ms). The fit parameters from the fitting functions are listed in Table 0-3 (Appendix D). Both the fast and slow phases are linearly decelerated by the increasing addition of glycerol (Figure 4.9).

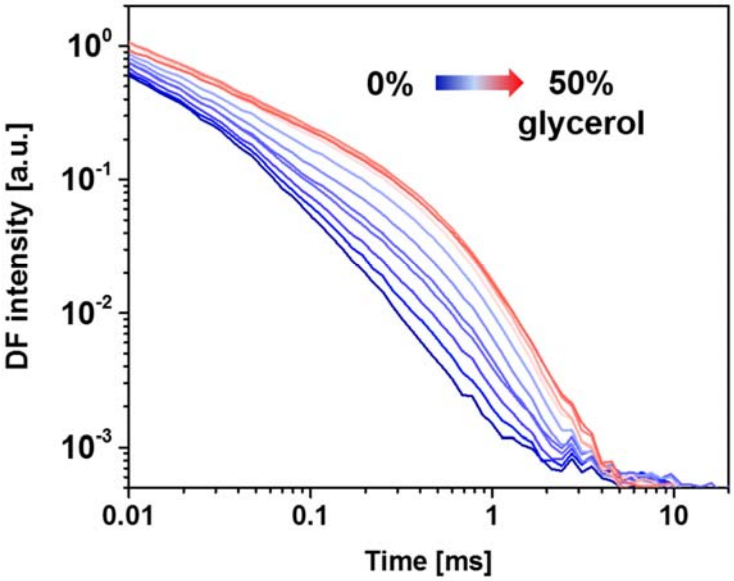

**Figure 4.8 The time course of DF decay in presence of glycerol (10 µs to 10 ms) on a double logarithmic scale after the second laser flash (pH 6.2, 20 °C). The gradient blue color refers to the experimental data of various glycerol concentrations (v/v from 0 to 50%, blue to right orientation following the arrow).**

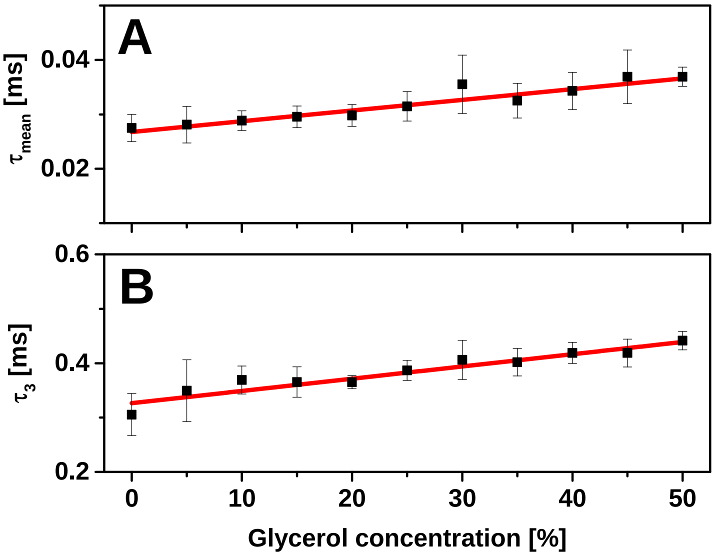

**Figure 4.9. The time constants of $\tau_{mean}$ and $\tau_3$ as a function of glycerol concentration. The shown data are simulation results from the DF transients after the second saturating flash as shown in Figure 4.8. (A) the mean time constant of the deprotonation and (B) the time constant of the electron transfer in the $S_2$ to $S_3$ transition. The error bars represent the standard deviations of the repeated measurements.**

### 4.2.2 Kinetics of Electron Transfer Affected by Glycerol on Acceptor Side

In addition to the donor side, the acceptor side plays also an important role in the kinetics of protonation and electron transfer. The primary and secondary quinones ($Q_A$ and $Q_B$) couple the electron transfer from $P_{680}$ through Pheophytin to $Q_A$ and then through a non-heme iron ion ($Fe^{2+}$/ $Fe^{3+}$) to the $Q_B$. After two accumulative reduction processes, the $Q_B^{2-}$ binds two protons and forms $Q_BH_2$, which diffuses to the quinone pool.

To further understand and approach the redox state of the primary quinone, the prompt fluorescence (PF) of PSII enriched membrane particles was detected from 0.1 ms to 700 ms after a series of 32 saturating laser flashes with a flash spacing of 700 ms (Figure 4.10). The PF intensity can be characterized by three major parameters:

(1) $F_0$, the relative fluorescence yield prior to the saturating flash. It corresponds to the open state of the reaction centre (RC) $P_{680}$ with fully oxidized $Q_A$.

(2) $F_{max}$, the maximum of the relative fluorescence yield after the saturating flash. It refers to the closed state of the reaction centre $P_{680}$ with fully reduced $Q_A$.

(3) $F_{min}$, the minimum relative fluorescence yield after the saturating flash and before the next excitation. It indicates the reoxidation level of the $Q_A^-$ in a time interval. In the given study, $F_{min}$ is the fluorescence yield 700 ms after the induced flash.

As can be seen in Figure 4.10A and C, the addition of glycerol reshapes the patterns, which in a way is comparable to measurements without addition of electron acceptors (data not shown), indicating accumulative $Q_B^{2-}$. Due to the fact that the reduced form of $Q_A$, i.e. $P_{680}^+Q_A^-$, has a stronger electrostatic effect that electrons will be transferred back to the primary donor, thus generating a higher amount of fluorescence. The addition of glycerol does not affect the dark-adapted oxidation state of the $Q_A$ ($F_0$), however it increases the maxima of the PF intensity ($F_m$) after each saturating flash, (Figure 4.11A and B). It may alter the quantum efficiency of the photochemical reaction (see $F_v/F_m$ in Figure 4.11 C), where $F_v$ is the difference between $F_m$ and $F_0$.

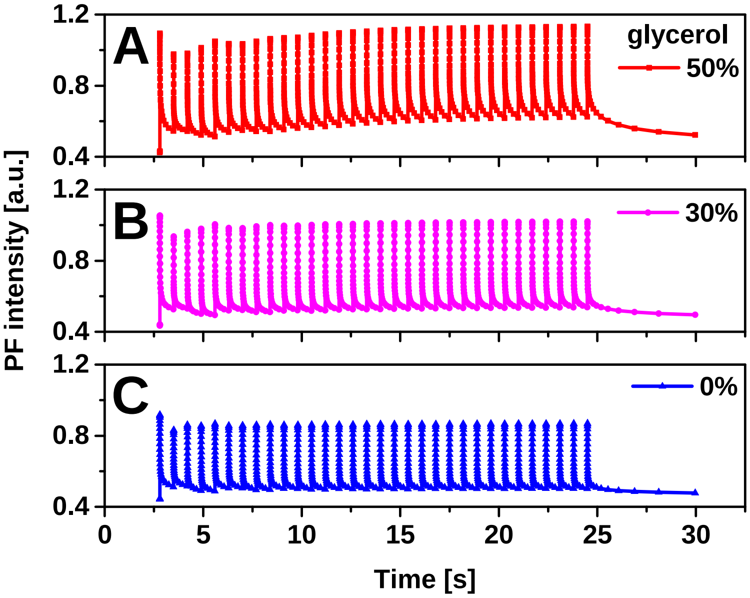

**Figure 4.10. The time course of PF decay of spinach PSII were detected from 0.1 ms to 700 ms after a series of 32 saturating laser flashes respectively (pH 6.2, 20 ºC). (A) Control buffer of 50% glycerol (in red); (B) of 30% glycerol (in magenta) and (C) of 0% glycerol treatment (in blue). They were averaged over six repeated measurements.**

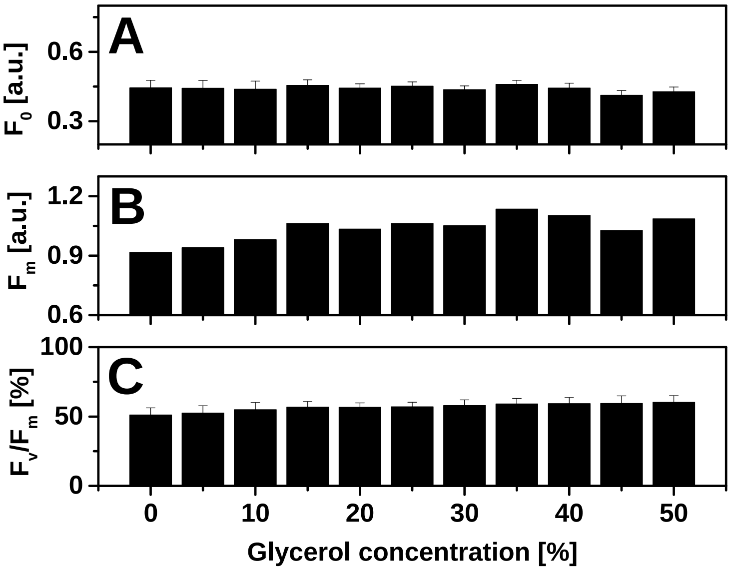

**Figure 4.11. The prompt fluorescence intensity of Figure 4.10 as a function of glycerol concentration dependence. (A) $F_0$, is the relative fluorescence yield prior to the saturating flash. (B) $F_m$ is the maximum of the relative fluorescence yield after the saturating flash. (C) $F_v/F_m$ is a normalized ratio representing the quantum efficiency of photochemical reaction of the PSII.**

In previous study, it was reported that high intensity of photo damage can partially blocked or strongly delayed the electron transfer between $Q_A$ and $Q_B$ even though the exact reason was not yet known (Lazar, 1999). Accordingly, this portion of blocked $Q_B$ limits the S-state transitions, thus malfunctions the water oxidation, i.e. the oxygen evolution. The ratio of blocked $Q_B$, denoted as $[Q_B]_{\text{blocked}}$ is determined according to

$$[Q_B]_{blocked} = \frac{F_{\min} - F_0}{F_m - F_0} \ , \qquad \textbf{(4.1)}$$

where $F_{\min}$ is the minimum fluorescence right before the next photoexcitation.

As shown in Figure 4.12, the fraction of the blocked centres stays at the level of 14% of the control sample, close to the minimum fraction reported before (Grabolle, 2005). It is barely affected by addition of up to 30% glycerol when the sample is only excited by a few flashes (see Figure 4.12 for an example of 1 and 10 flashes). As more $Q_B^-/Q_B^{2-}$ are accumulated, for instance after 30 flashes, stronger effect can be seen. In parallel, a higher content of glycerol may perturb the orientation of $Q_A$ and $Q_B$, and could therefore increase the number of blocked centres. This is in line with the previous evidences on the donor side, i.e. in Section 4.2.1 that the oxygen activity is not significantly affected by addition of 30% glycerol. In contrast, at higher flash numbers, the fraction of blocked $Q_B$ is affected to a higher degree. In order to approach further details of the glycerol effect on the kinetics of electron transfer between $Q_A$ and $Q_B$, the PF transients are shown in Figure 4.13.

It is suggested in Figure 4.13A that the dynamics of electron transfer from not only the donor side (see Section 4.2.1) but also from the acceptor side are affected by glycerol content (especially in higher concentration). As introduced in Section 2.3, the PF decay is a multiphasic process with at least three phases. So in order to access the kinetics, a tri-exponential function was applied to the PF decay and the time constant of half decay was obtained, as shown in Figure 4.13B. The half-time, $\tau_{1/2}$, corresponds to the electron transfer from $Q_A^-$ to $Q_B$, which is typically 1 ms to 10 ms in plants. The variations are caused mainly by the affinity of the $Q_B$ site and the protein environment, such as pH value and hydration levels. The electron transfer from $Q_A$ to $Q_B$ is relatively unaffected up to 20% glycerol ($\tau_{1/2} \approx 5$ ms) but decelerated by a higher mixture of glycerol. This glycerol influence is comparable to the electron transfer in the $S_3$ to $S_0$ transition. The deceleration is presumably due to the perturbation of both quinone-binding sites by higher population of glycerol molecules. It is noted that glycerol binding was resolved in the protein crystal structure, locating it approximately at 10 Å distance to the $Q_A$ (Figure 4.2).

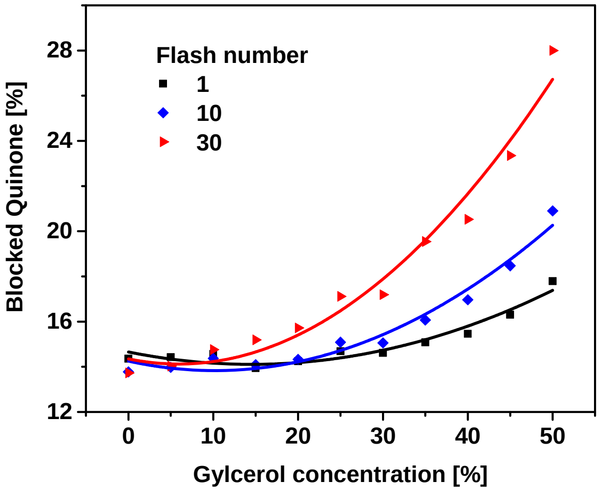

**Figure 4.12.The percentage of blocked $Q_B$ in spinach PSII detected by prompt fluorescence as a function of glycerol concentration dependence, determined based on equation (4.1).**

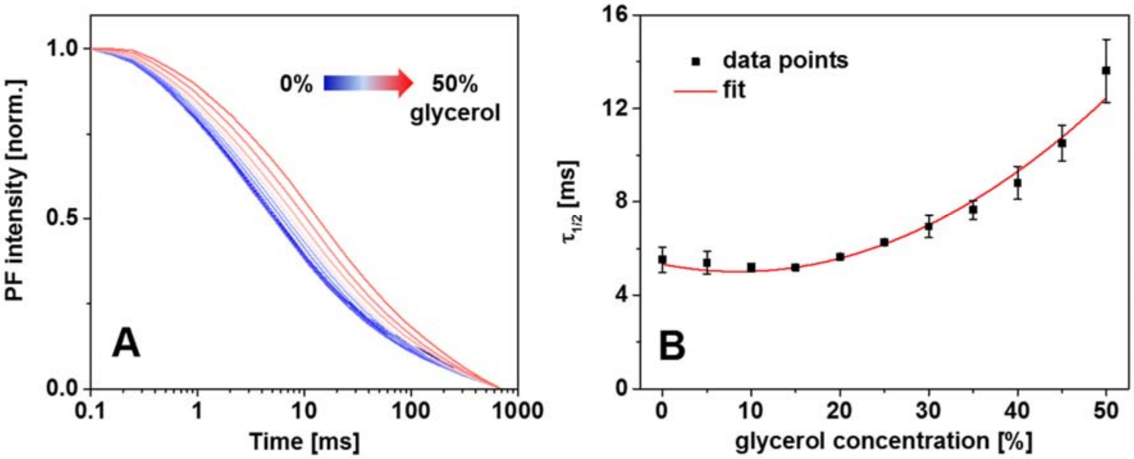

**Figure 4.13. Prompt fluorescence characteristics of spinach PSII as a function of glycerol concentration dependence after the first saturating flash (pH 6.2, 20 °C). The fluorescence intensity correlates to the redox state of the primary quinone, $Q_A$. (A) The time course of PF transients on a semi-logarithmic scale, from 0.1 ms to 700 ms in glycerol concentration from 0 to 50% (dark blue to dark red colour). (B) Time constants of the half decay, which are the fitting results by a sum of three exponential functions to the transients in panel A. The error bars represent the standard errors from six repeated measurements.**

It is suggested in Figure 4.13A that the dynamics of electron transfer from not only the donor side (see Section 4.2.1) but also from the acceptor side are affected by glycerol content (especially in higher concentration). As introduced in Section 2.3, the PF decay is a multiphasic process with at least three phases. So in order to access the kinetics, a tri-exponential function was applied to the PF decay and the time constant of half decay was obtained, as shown in Figure 4.13B. The half-time, $\tau_{1/2}$, corresponds to the electron transfer from $Q_A^-$ to $Q_B$, which is typically 1 ms to 10 ms in plants. The variations are caused mainly by the affinity of the $Q_B$ site and the protein environment, such as pH value and hydration levels. The electron transfer from $Q_A$ to $Q_B$ is relatively unaffected up to 20% glycerol ($\tau_{1/2} \approx 5$ ms) but decelerated by a higher mixture of glycerol. This glycerol influence is comparable to the electron transfer in the $S_3$ to $S_0$ transition. The deceleration is presumably due to the perturbation of both quinone-binding sites by higher population of glycerol molecules. It is noted that glycerol binding was resolved in the protein crystal structure, locating it approximately at 10 Å distance to the $Q_A$ (Figure 4.2).

As discussed from the here reported results (Figure 4.3 to Figure 4.13), the PSII activity was decreased along with decelerated dynamics in presence of glycerol. The following points could be an explanation for these findings:

(i) Higher viscosity can slow down the chemical reactions which are diffusion limited or contain large scale translational motion (e.g. 40 Å) (Heimann et al., 2000), however, no such a large scale motion in PSII regarding to the proton or electron transfer has been observed. Therefore, this is unlikely to play a role in this study.

(ii) Protein hydration (Davis-Searles et al., 2001) and 'solvophobic effect' in which glycerol may move from nonpolar regions into the bulk solvent (Arakawa & Timasheff, 1982). Further level in hydration can increase the destabilization of the certain PSII subunits which are functional associated.

(iii) Glycerol binds to the Mn cluster, suggested by comparing the inhibition effect of oxygen activity by glycerol in intact and salt-washed (i.e. without extrinsic subunits) PSII (Halverson & Barry, 2003), since the removal of the extrinsic subunits increases the access to the Mn cluster (Ghanotakis et al., 1984; Tamura et al., 1989).

(iv) Alteration of the surface tension cannot be neglected. In aqueous environments, protein – conformational flexibility, has a wide range of hydration states. The activity of water within its microenvironment is one of the important factors that determines the equilibrium between these states (Parsegian, 2002).

(v) Modification of the protein-protein interaction can also be an issue since the oscillation pattern of proton release is restored by addition of glycerol, as shown with evidence in PSII core complex (Haumann et al., 1997).

### 4.2.3 Glycerol Effect on Activation Energy of O-O Bond Formation

The kinetics of proton and electron dynamics in PSII are clearly decelerated with increasing content of glycerol. This raises the question whether it affects the O-O bond formation specifically by altering the energetic barrier. Higher concentration of glycerol in the buffer (>30%) inhibits the oxygen activity, as suggested in the steady-state rate of oxygen production (Halverson & Barry, 2003). In contrast, low content of glycerol shows hardly any effect on the kinetics. Therefore, a content of 30% glycerol was chosen in this study, so that the kinetics of the electron transfer between $S_3$ and $S_4$ state were hardly affected.

Based on the transition state theory and Arrhenius equation, the activation energy of a specific chemical reaction is determined from the rate constant as a function of temperature, as introduced in Section 1.3.3.1. The measurements were performed from 0 °C to 30 °C with an increment of 2.5 °C. Detection in a wider range of temperatures turned out to be difficult, since the thermal conductivity was limited by the transparent plastic cuvette, which was used in the experiment. The cuvette was placed within a copper holder in a half-open setup allowing the access of the excitation area (about 2 $cm^2$) from the laser flash on one side and the detection area on another side. The DF transients in the range between 1 ms to 11 ms are shown in Figure 4.14. This is to highlight the kinetics of the slow phase, which have a time constant of about 2 ms at ambient temperature (Cox et al., 2014; Siegbahn, 2017; Vinyard et al., 2015).

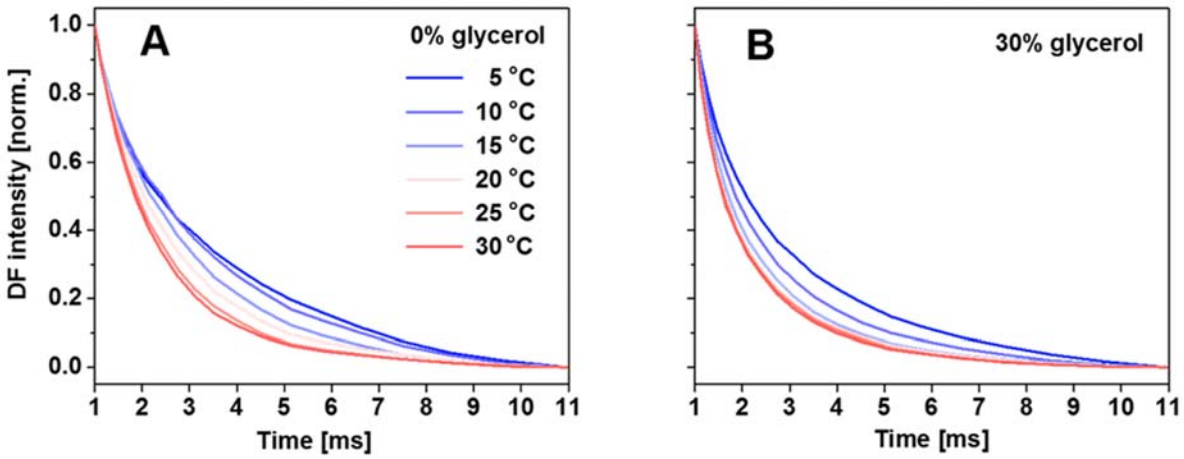

**Figure 4.14. DF signal of PSII enriched membrane fragments after the third saturating flash from 5 ºC to 30 ºC, with 5 ºC increment. (A) in control buffer (glycerol-free) and (B) in 30% of glycerol (v/v). The amplitude is normalized to [1, 0] from 1 ms to 11 ms.**

By applying the universal fitting of a tri-exponential function (from 10 µs to 11 ms) as introduced in Section 2.4.3 and discussed in Section 4.2.2, the slow phase which correlates to the rate constants of the electron transfer (after the third saturating flash) could be resolved. The fitting parameters are listed in Table 0-4 and Table 0-5 for 0% and 30% glycerol, respectively (Appendix D).

The slow phase, $\tau_{ox}$, is plotted as a function of the $1/k_BT$ based on the Arrhenius equation, which is commonly referred to as an Arrhenius plot (Figure 4.15). As introduced in Section 1.3.3, the slope of the semi-linear fit is proportional to the activation energy, resulting in a value of 230 meV in the control. This value is in line with earlier studies (Buchta et al., 2007; Grabolle, 2005; Grabolle & Dau, 2005), even though it may vary from preparation and methods (Isgandarova et al., 2003). Surprisingly, for PSII in 30% glycerol, the activation energy was determined to be 160 meV, which is significantly lower (70 meV ± 10 meV) than the control. This effect is similar to the functionality of enzyme, which is to lower the energetic barrier of a chemical reaction, e.g. by breaking a chemical bond and promoting a faster rate constant, or alternatively, accelerating a chemical reaction. So in comparison, it raises the question whether glycerol has similar characteristics as an enzymes in this regard. If not, what kind of role glycerol may play. To answer this question, further investigation has been performed by comparing the activation energy among different PSII variants in the next chapter.

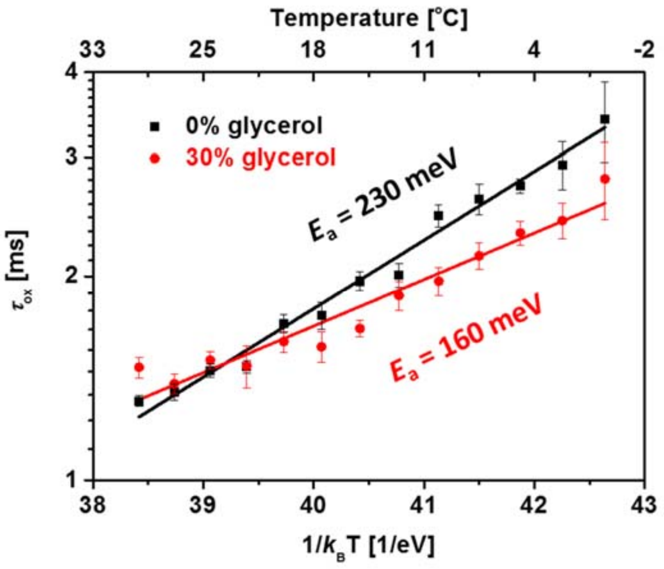

**Figure 4.15. Time constants of the slow phase, $\tau_{ox}$, in the $S_4$ to $S_0$ transition as a function of temperature from 0 °C to 30 °C on a semi-logarithmic plot comparing the control glycerol-free buffer condition (in black) and 30% glycerol buffer (in red). The linear line is a fit based on the Arrhenius equation. The bars are the standard errors. The fit parameters are listed in Appendix F.**

## 4.3 Summary

In this chapter, the kinetics of proton and electron transfers at the electron donor side of PSII (water oxidation) and at its acceptor side ($Q_A$ reduction) were observed after laser-flash excitation in the time domain of 10 µs to 10 ms (by DF) and 100 µs to 700 ms (by PF), respectively. By variation of the glycerol content (from 0% to 50%) in the otherwise aqueous buffer, a pronounced influence of glycerol on electron and proton transfer steps in water oxidation and $Q_A$/$Q_B$ reduction was detected.

The deprotonation step prior to O-O bond formation is found to be strongly affected by glycerol in the aqueous buffer even at relatively low concentration, while the rate constant of oxygen evolution and the quantum efficiency of S-state transitions is affected only at high glycerol concentration (above 30% volume percent). From the acceptor side, the electron transfer from $Q_A^-$ to $Q_B$ is also decelerated by glycerol addition.

It has been reported that addition of glycerol would weaken the hydrogen bonding among water molecules (Dashnau et al., 2006). Consequently, as a network like this the proton and electron transfer is slower (Polander & Barry, 2012). It is worthwhile to mention that glycerol has high viscosity compared to pure water, thus is known to slow down the chemical reactions which are diffusion limited or large scale translational motion (Heimann et al., 2000). However, no such a large scale motion in PSII has ever reported regarding to the proton or electron transfer. Therefore, the herein discussed glycerol effects causing the deceleration of both proton and electron transfer cannot be simply explained by the contribution of viscosity.

Moreover, first indications that activation enthalpies are strongly modified by the increasing glycerol concentrations have been reported. An analysis from the Arrhenius plot reveals that the activation enthalpy of oxygen evolution is strongly decreased in 30% glycerol buffer, whereas the influence on the rate constant at room temperature is negligibly small. With and without glycerol, the activation enthalpies are significantly lower than the energetic barriers obtained from a quantum chemical calculation (Siegbahn, 2013). The glycerol influence may result from disturbed protonation dynamics by specific binding of glycerol molecules within PSII. This is a surprising result which leads me to consider the possible reasons. Therefore, the following chapter investigates the activation energy of O-O bond formation of PSII from different species.

# Chapter 5 Activation Energy of O-O Bond Formation in PSII variants

Based on the knowledge from complete genomes and available databases, the evolution of oxyphotosynthetic organisms is known to be developed from prokaryotes (such as cyanobacteria) to unicellular eukaryotes (such as green algae) and multicellular plants, progressing from the process of primary endosymbiosis (De Las Rivas et al., 2004). During the time course of evolution, the major component of the intrinsic core complexes of PSII in all oxyphotosynthetic organisms remained highly conserved, especially the ligands bounding to the first coordination sphere of oxygen evolving centres (OEC) are conserved (Amunts et al., 2007; Glockner et al., 2013; Nield et al., 2000).

The comparative study of the functional difference between species is one of the most important topics in biophysics, for instance, from the evolutionary point of view, to develop insights by addressing the differences among cyanobacteria, green algae and plants. Regarding the essential function of water oxidation in PSII, it may provide more clues to understand this critical process by investigating the activation barrier difference in the O-O bond formation.

Several studies have been performed in which the kinetics of oxygen evolution were analyzed and where the activation energy was discussed. This has been done, e.g., for the D1-D61N and D1-V185N mutations at the second sphere of the Mn-complex of *Synechocystis* sp. PCC 6803 (Bao & Burnap, 2015). In addition, a comparison of cyanobacterial *Thermosynechococcus elongatus* to plant spinach was reported in (Isgandarova et al., 2003).

## 5.1 Experimental Details

The PSII particles (BBY from spinach and thylakoid membrane particles from cyanobacteria) were calibrated into a chlorophyll (Chl) concentration of 200 µg/ml (spinach) and 40 µg/ml (cyanobacterial PSII extracts), respectively, as stock samples and stored on ice until used (as introduced in Section 2.1). For each measurement, quantitative PSII sample (equivalent to 75 µg of Chl) was added onto each electrode and centrifuged at 4 °C for 12 minutes in a Sorvall HB-4 swing rotor. The sample was centrifuged at 20 °C for measurement conditions above 25 °C, in order to minimize the heating time and to achieve a better thermal stability. A control measurement confirms that the sample activity or kinetics are not affected by centrifugation at either 4 °C or 20 °C in the given time (data not shown).

As introduced in Section 2.5.1 of material and methods, the kinetics of the oxygen evolution from PSII can be determined by time-resolved oxygen polarography. For each measurement, the PSII particles of plant were excited by a series of 20 saturating flashes, while those of cyanobacteria were excited by 52 flashes. As can be seen in Figure 5.1, a series of 204 saturating flashes has been applied to the cyanobacterial thylakoid membranes, however, the oxygen-evolving activity starts to decrease significantly after about 30 to 50 flashes, presumably due to the competing photosynthetic and respiratory activities on the plastoquinone pool (Mullineaux, 2014).

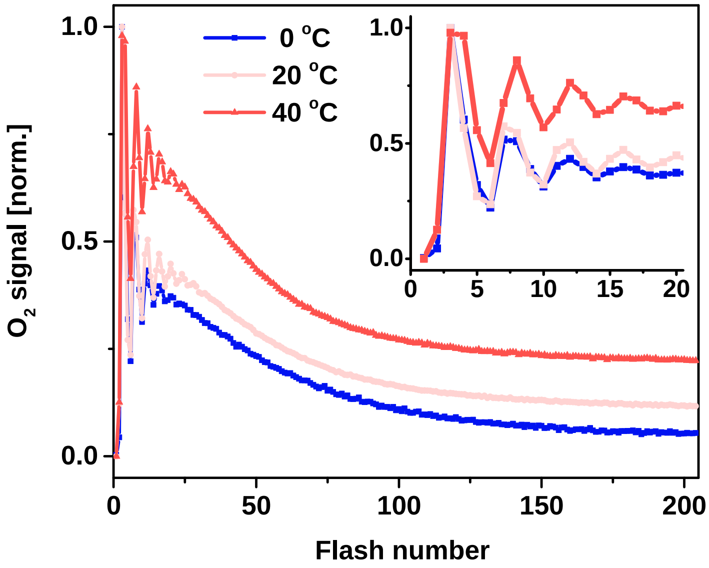

**Figure 5.1. Temperature dependence of oxygen evolution as a function of saturating flash number. The thylakoid membranes of *Thermosynechococcus elongatus* BP-1 (wild-type), were excited by 204 saturating flashes at 0 °C, 20 °C and 40 °C (in blue, light and dark red respectively). The $O_2$ signal was determined by the maximum of individual oxygen transients from polarography.**

In order to increase the signal to noise ratio and analyze the kinetics, the oxygen transients of *T. elongatus* were averaged from the 3rd to the 52nd flash. As can be seen in Figure 5.2, the averaged transient is consistent with the individual transient (e.g. the 3rd flash). This means that the accumulative flashes do not accelerate or decelerate the kinetics, thus the process of normalization and averaging data does not affect the kinetics. It helps to increase the signal to noise ratio by a factor of 7 approximately.

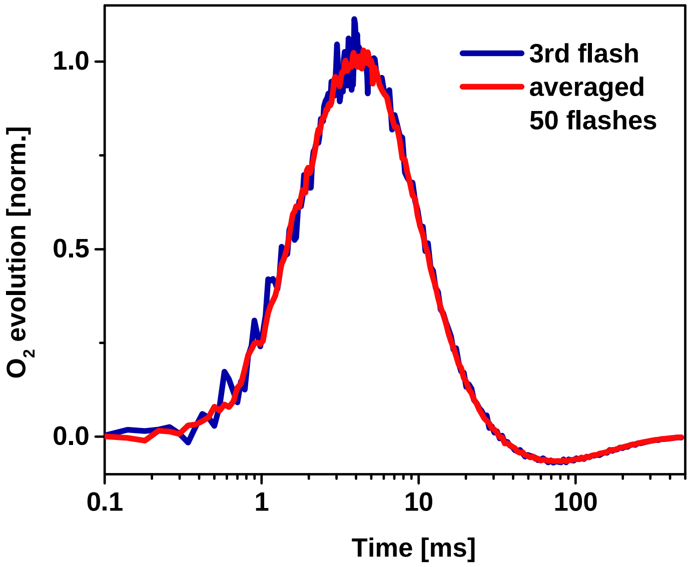

**Figure 5.2. Oxygen transients of thylakoid membrane of *Thermosynechococcus elongatus* BP-1 (wild-type). The membrane was excited by the 3rd saturating flash (in blue) and averaged over 50 flashes (from the 3rd to the 52nd) at pH 6.2 at 20 °C, detected by oxygen polarography.**

## 5.2 Results and Discussion

In the given study three species were compared, namely spinach as well as *Synechococcus* sp. PCC 7002 and *Thermosynechococcus elongatus* BP-1 (wild type and PsbA3). The basic characteristic of the species can be seen in Table 5-1, including the growth type, isolation place and time, genome size and difficulty-level of genetic manipulation.

The kinetics of oxygen evolution from each species were determined by oxygen polarography in temperatures ranging from -10 °C to 45 °C with an increment of 5 °C (only from 0 °C to 45 °C for PsbA3). In the following sections, the individual species are discussed, by presenting the oxygen transients, the fitting quality from the oxygen diffusion model, the key fit parameters and finally an Arrhenius plot summing up both fast and slow phases of the oxygen evolution from these species.

**Table 5-1. Characteristic of cyanobacterial *Synechococcus* sp. PCC 7002, *Thermosynechococcus elongatus* BP-1 and *Synechocystis* sp. PCC 6803, comparing the growth type, isolation place and time, genome size and difficulty level of genetic manipulation.**

| Species / Characteristic | *Synechococcus* sp. PCC 7002 | *Thermosynechococcus elongatus* BP-1 | *Synechocystis* sp. PCC 6803 |
|---|---|---|---|
| Growth type (optimal) | mesophilic,<br>35 °C - 38 °C | thermophilic,<br>55 °C - 60 °C | mesophilic,<br>28 °C - 30 °C |
| Isolation place and time | Magueys island, Puerto Rico in 1962 | Beppu, Japan in 1978 | Oakland, USA in 1962 |
| Genome size | 3.40 Mb, 3,235 Gene | 2.59 Mb, 2,528 Gene | 3.96 Mb, 3,725 Gene |
| Genetic manipulation | a few molecular techniques established | difficult | a few molecular techniques established |

### 5.2.1 Oxygen Evolution Transients of *Synechococcus* sp. PCC 7002

In order to compare the kinetics in a straightforward approach, the oxygen transients are normalized to unity and plotted semi-logarithmically. The data was detected from -10 °C to 45 °C with an increment of 5 °C (Figure 5.3). The temperature dependence of the onset delay from 0 ms to 2 ms is highlighted in the inset. Each averaged transient was fitted to the oxygen diffusion model in a simulation program (as introduced in Section 2.5.3), which gave a good fitting quality (Figure 5.4 and Figure 5.5). The fitted transients match the experimental ones to a high extent.

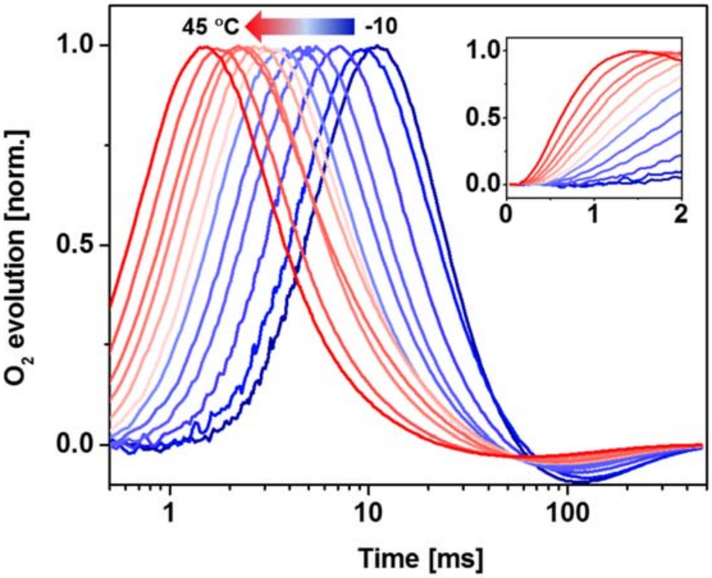

**Figure 5.3. Temperature dependence of oxygen evolution transients. They represent oxygen release kinetics ($S_3 \rightarrow S_4 \rightarrow S_0 + O_2$) from PSII of thylakoid membrane of *Synechococcus* sp. PCC 7002, measured at pH 6.2 from -10 °C to 45 °C (from dark blue to red) with an increment of 5 °C. The signals were averaged from the 3rd to the 52$^{nd}$ flash with 4 to 5 repeated measurements and normalized to unity.**

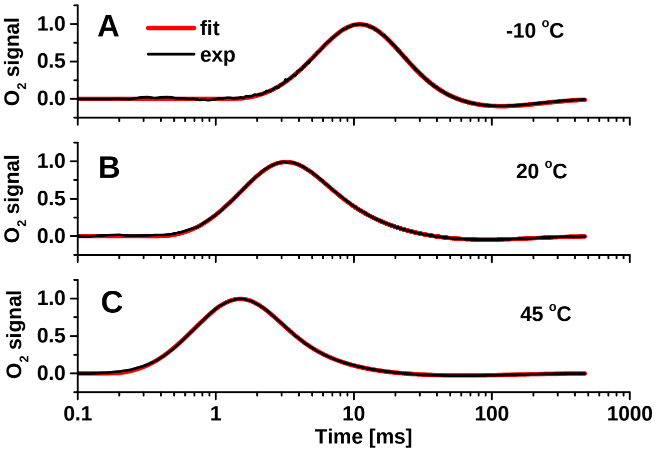

**Figure 5.4 Temperature-dependent transients of oxygen evolution of *Synechococcus* sp. PCC 7002 from Figure 5.3. The experimental data was fitted with the oxygen diffusion model (data in black and fit in red). Exemplary data for -10 °C, 20 °C and 45 °C are shown in panels A, B and C respectively. All the other fitted transients are attached in Appendix E.**

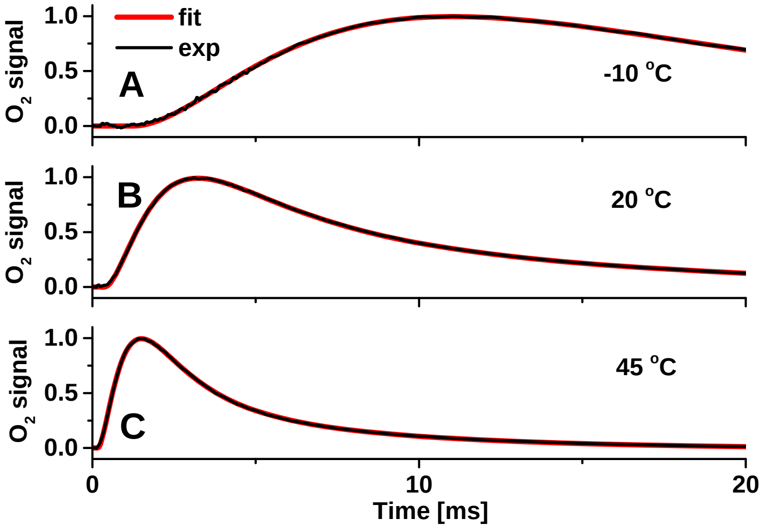

**Figure 5.5 Temperature-dependent transients of oxygen evolution of *Synechococcus* sp. PCC 7002 from Figure 5.3. The experimental data was fitted with the oxygen diffusion model (data in black and fit in red). Examplary data for -10 °C, 20 °C and 45 °C are shown in panels A, B and C respectively. They are presented on a linear scale from 0 to 20 ms, highlighting the rise time of the transients.**

The obtained results help to gain insight into the oxygen evolution and diffusion processes in PSII. As can be seen in Figure 5.6, a list of physical parameters was taken into account in the diffusion model (as introduced in Section 2.5.3):

(i) The effective membrane thickness is theoretically a constant value since the thylakoid membrane particles are present in the same amount in each measurement, i.e. 15 µg of chlorophyll. However, as can be seen in Figure 5.6A that the thickness tend to be slightly thinner at higher temperatures, mainly because this factor highly correlated to the speed of the electrode response, thus they both compensate each other. This can be well explained by the temperature-dependent diffusion coefficient.

(ii) The oxygen reduction rate at the platinum surface of the electrode. Its performance is faster at higher temperatures, a typical thermal characteristic of electrochemical reactions.

(iii) The population of the $S_3$ state, stays at about the same level, because the given transients are all normalized, i.e. they show the same amount of oxygen evolution.

(iv) The slow phase of oxygen evolution describes the kinetics of the electron transfer correlating to O-O bond formation, the very central parameter of this study. After the structural change of the O-O bond formation, the intermedia state $S_4^+$ is formed and a dioxygen molecule is released from the PSII particle.

(v) The delay time of the electrode response is also temperature dependent. This means the reduction rate of the oxygen on the platinum surface is not a constant but it is faster at higher temperatures.

(vi) The pre-phase of oxygen evolution, relates to the deprotonation of the $S_3^+$ to $S_3^n$ transition, which is a step prior to the oxidation of the Mn-complex.

(vii) The sum of both lag- and pre-phases (named fast phase) describes the delay of the onset of the electrode response and the deprotonation step. This parameter is useful because the separation between the strongly correlated lag- and pre-phases cannot be made reliably.

The plots in Figure 5.6viii and ix show parameters of both the slow ($k_{ox}$) and the fast phase ($k_{lag+pre}$) from -10 °C to 45 °C, respectively. The Arrhenius plot of both phases are presented in Figure 5.7, fitted with a linear regression, respectively. The fits are based on Arrhenius equation:

$$\ln(k) = \ln(A) - E_a/k_B T ,$$

where $k$ is the rate constant, $A$ is the pre-exponential frequency factor, and $E_a$ is the activation energy. $A$ and $E_a$ are determined from the intercept (y-axis) and slope, respectively. See detail fit parameters in Table 5-2 and Table 5-3 in Section 5.2.4.

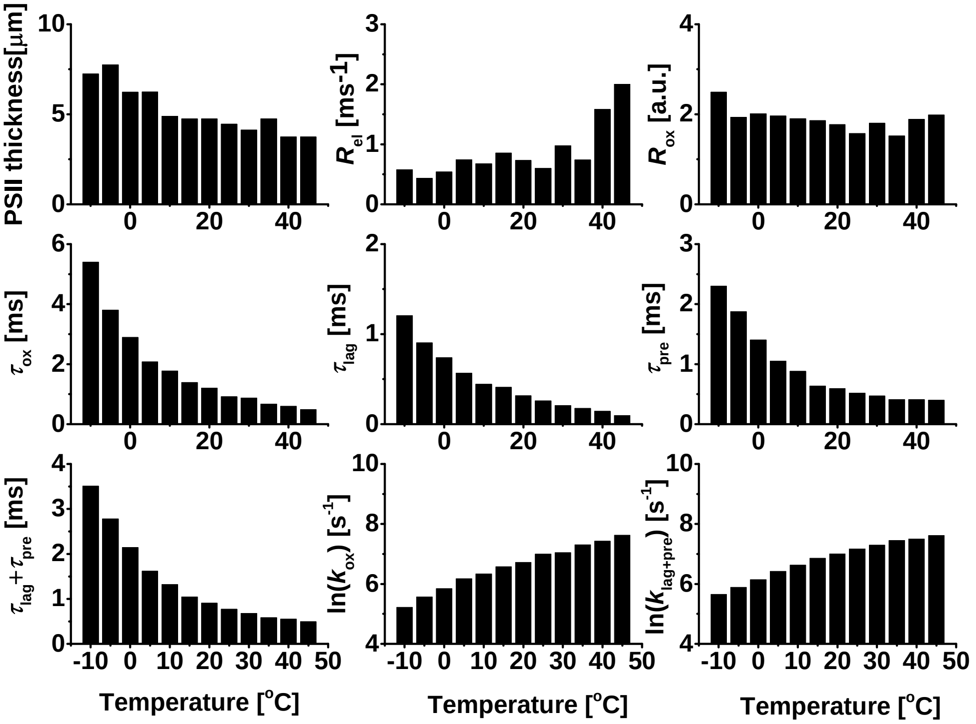

**Figure 5.6. Fit parameters of the diffusion model, applied to the individual oxygen transients of thylakoids of *Synechococcus* sp. PCC 7002. Orientation from upper left to lower right: (i) thickness of the thylakoid membrane layer deposited on the electrode surface; (ii) $R_{el}$, electrode constant of the oxygen reduction speed; (iii) $R_{ox}$, the population of the $S_3$ state; (iv) $\tau_{ox}$, the slow phase of oxygen evolution; (v) $\tau_{lag}$, the lag phase of the delay of electrode response; (vi) $\tau_{pre}$, the pre-phase of the delay of oxygen evolution; (vii) $\tau_{lag}+\tau_{pre}$, sum of the lag- and pre-phases; (viii) ln($k_{ox}$), rate constant of the slow phase on a logarithmic scale; and (ix) ln($k_{lag+pre}$), rate constant of the sum of the lag- and pre-phases on a logarithmic scale.**

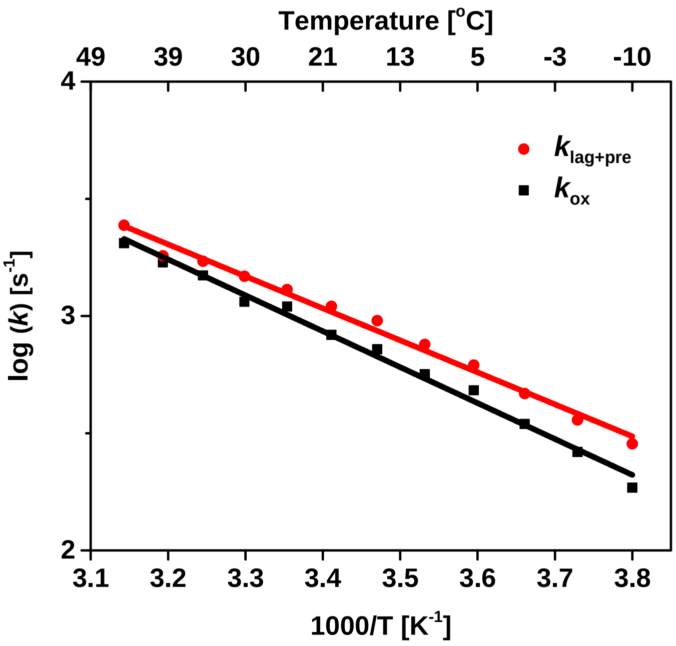

**Figure 5.7. Arrhenius plot of the rate constants of the the sum of lag and pre-phase (red) and oxygen phase (black) of *Synechococcus* sp. PCC 7002. Kinetics are resolved from the diffusion model of the simulation. The symbols represent the experimental data while the lines in corresponding colour are obtained from a linear fit of the data. The plot is based on Arrhenius equation $\ln(k) = \ln(A) - E_a/k_BT$, where $k$ is the rate constant, $A$ is the pre-exponential frequency factor, and $E_a$ is the activation energy. $A$ and $E_a$ are determined from the intercept (y-axis) and slope, respectively. See detail fit parameters in Table 5-2 and Table 5-3 in Section 5.2.4.**

### 5.2.2 Oxygen Evolution Transients of *Thermosynechococcus elongatus* BP-1

For cyanobaterial *Thermosynechococcus elongatus* BP-1, oxygen transients were detected from polarography analogously to the previous section (Figure 5.8 of PSII-wild type and Figure 5.9 of PSII-PsbA3). The simulations are similar to those in the previous section. The fitted transients and the fit parameters are presented in Appendix E. Each transient was fitted to the oxygen diffusion model as presented earlier (in Section 5.2.1). The Arrhenius plot of both fast and slow phases are presented in Figure 5.10 and Figure 5.11, where the rate constants, $\tau_{\text{lpre}}$, $\tau_{\text{lag+pre}}$ and $\tau_{\text{ox}}$, are fitted with a linear regression, respectively. See detail fit parameters in Table 5-2 and Table 5-3 in Section 5.2.4.

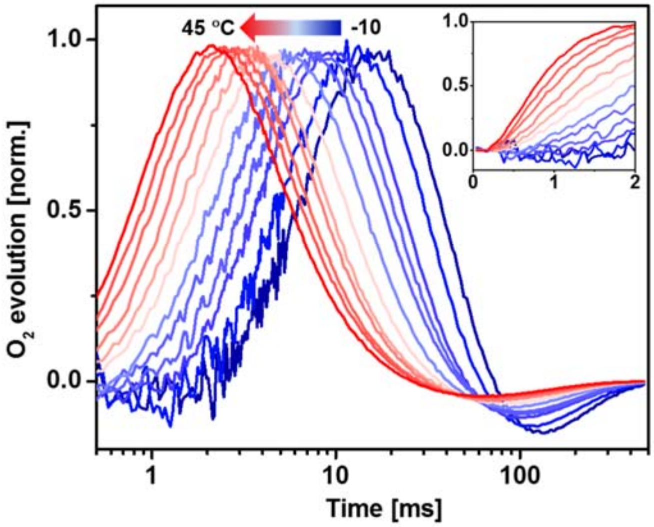

**Figure 5.8. Temperature dependence of oxygen evolution transients. They represent oxygen release kinetics ($S_3 \rightarrow S_4 \rightarrow S_0 + O_2$) from PSII of thylakoid membrane of *Thermosynechococcus elongatus* BP-1 wild-type, measured at pH 6.2 from -10 °C to 45 °C (only from 0 °C for PsbA3) with an increment of 5 °C. The signals were averaged from the 3rd to the 52nd flash with 4 - 5 repeated measurements.**

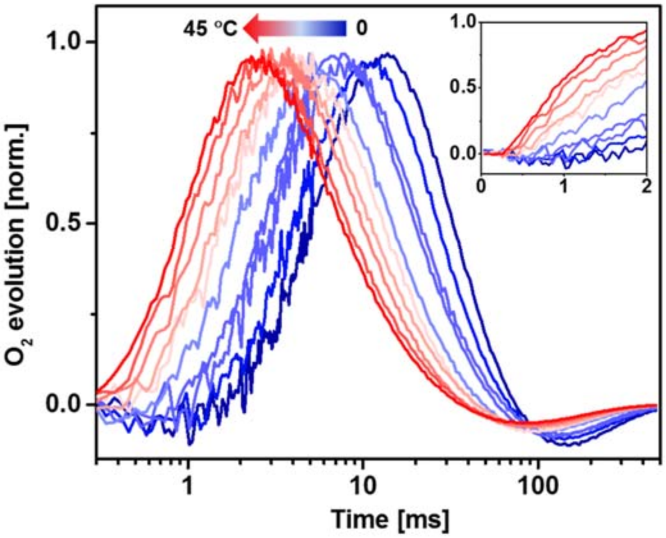

**Figure 5.9. Temperature dependence of oxygen evolution transients. They represent oxygen release kinetics ($S_3 \rightarrow S_4 \rightarrow S_0 + O_2$) from PSII of thylakoid membrane of *Thermosynechococcus elongatus* BP-1 PsbA3, measured at pH 6.2 from 0 °C to 45 °C with an increment of 5 °C. The signals were averaged from the 3rd to the 52nd flash with 2 - 3 repeated measurements.**

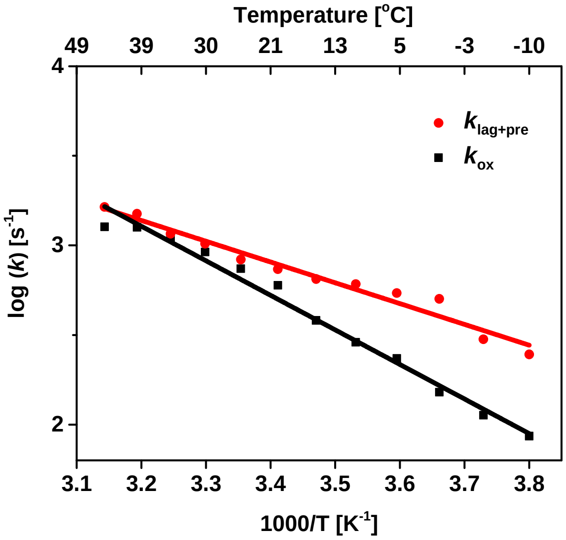

**Figure 5.10. Arrhenius plot of oxygen release rate constants of the sum of lag and pre-phase (red) and oxygen phase (black) of *Thermosynechococcus elongatus* BP-1 PSII wild-type. Kinetics are resolved from the diffusion model of the simulation. The symbols represent the experimental data while the lines in corresponding colour are obtained from a linear fit of the data. The plot is based on Arrhenius equation $\ln(k) = \ln(A) - E_a/k_BT$, where $k$ is the rate constant, $A$ is the pre-exponential frequency factor, and $E_a$ is the activation energy. $A$ and $E_a$ are determined from the intercept (y-axis) and slope, respectively. See detail fit parameters in Table 5-2 and Table 5-3 in Section 5.2.4.**

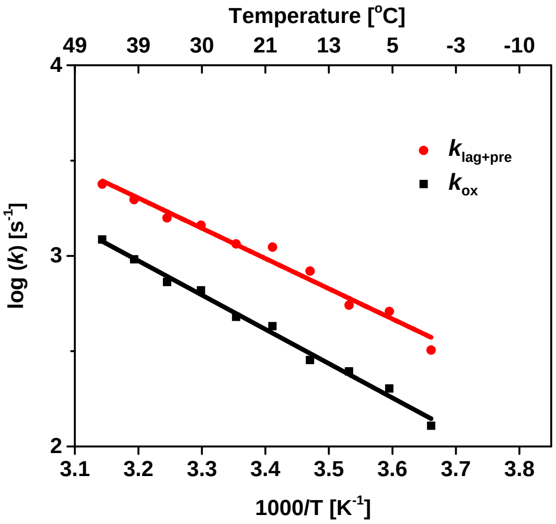

**Figure 5.11. Arrhenius plot of oxygen release rate constants of the sum of lag and pre-phase (red) and oxygen phase (black) of *Thermosynechococcus elongatus* BP-1 PSII-PsbA3 isoform. Kinetics are resolved from the diffusion model of the simulation. The symbols represent the experimental data while the lines in corresponding colour are obtained from a linear fit of the data. The plot is based on Arrhenius equation $\ln(k) = \ln(A) - E_a/k_BT$, where $k$ is the rate constant, $A$ is the pre-exponential frequency factor, and $E_a$ is the activation energy. $A$ and $E_a$ are determined from the intercept (y-axis) and slope, respectively. See detail fit parameters in Table 5-2 and Table 5-3 in Section 5.2.4.**

### 5.2.3 Oxygen Evolution Transients of Plant Spinach

In order to compare the oxygen transients in a straightforward way, all the transients are normalized to unity and plotted on a semi-logarithmic scale, as shown in Figure 5.12. The fitted transients and the fit parameters are presented in Appendix E.

Each transient was fitted to the oxygen diffusion model as presented earlier (in Section 5.2.1).The Arrhenius plot of both fast and slow phases are presented in Figure 5.13, fitted with a linear regression, respectively. See detail fit parameters in Table 5-2 and Table 5-3 in Section 5.2.4.

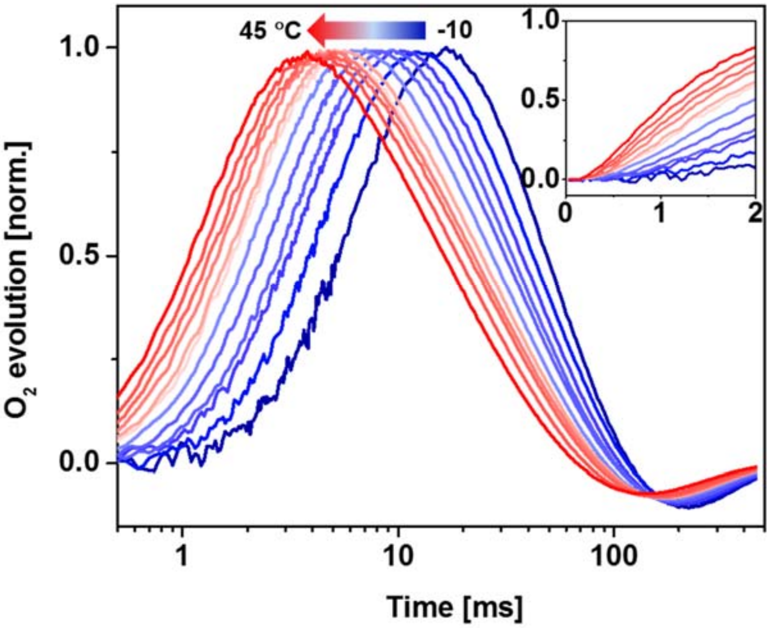

**Figure 5.12. Temperature dependence of oxygen evolution transients. They represent oxygen release kinetics ($S_3 \rightarrow S_4 \rightarrow S_0 + O_2$) from PSII of thylakoid membrane of spinach, measured at pH 6.2 from -10 °C to 45 °C (dark blue to red) with an increment of 5 °C. The signals were averaged from the 3rd to the 14th flash and across four repeated measurements.**

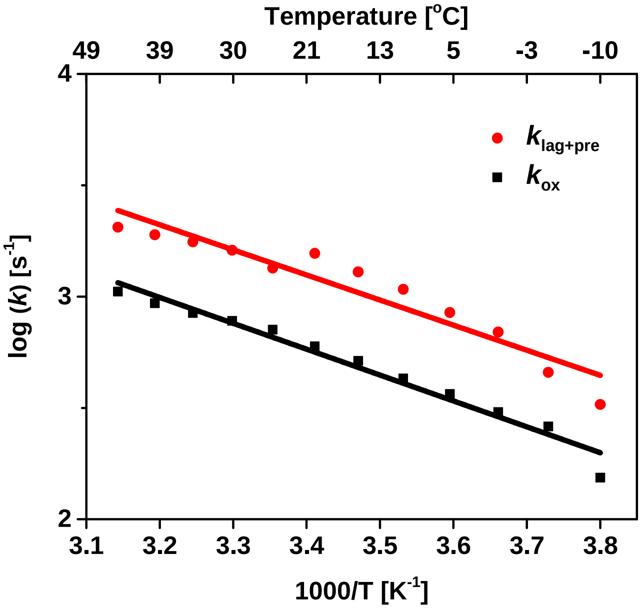

**Figure 5.13. Arrhenius plot of oxygen release rate constants of the sum of lag- and pre-phase (red) and oxygen phase (black) of spinach. Kinetics are resolved from the diffusion model of the simulation. The symbols represent the experimental data while the lines in corresponding colour are obtained from a linear fit of the data. The plot is based on Arrhenius equation $\ln(k) = \ln(A) - E_a/k_BT$, where $k$ is the rate constant, $A$ is the pre-exponential frequency factor, and $E_a$ is the activation energy. $A$ and $E_a$ are determined from the intercept (y-axis) and slope, respectively. See detail fit parameters in Table 5-2 and Table 5-3 in Section 5.2.4.**

### 5.2.4 Comparison of Activation Energy of O-O Formation among PSII variants

As presented in Sections 5.2.1 to 5.2.3, both the fast and slow phases were kinetically well resolved by the analysis of the oxygen diffusion model. The kinetics of oxygen evolution in cyanobacteria and spinach differ under the same temperature condition. Detail comparison is necessary in order to highlight the kinetic differences among those species, and to enable a comparison of the transients measured at 0 °C, 20 °C and 40 °C (Figure 5.14). In comparison, the oxygen evolution of spinach is faster at 0 °C but slower at 40 °C than that of *T. elongates* wild-type. This suggests that the oxygen evolution of spinach has smaller change in the same temperature range than the T. elongates wild-type. The corresponding Arrhenius plots of the fast and slow phase of each species will be presented in the following sections.

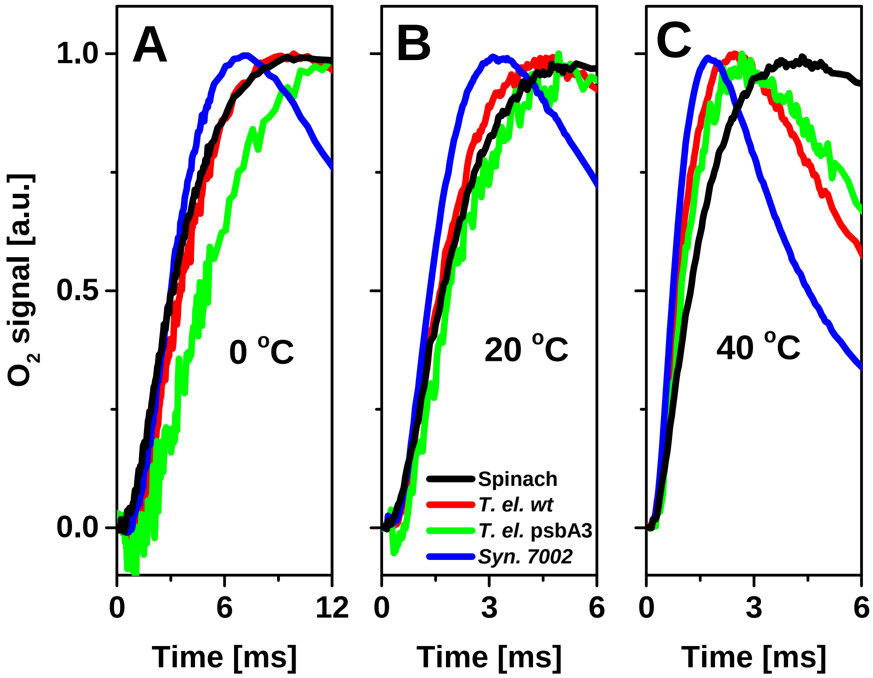

**Figure 5.14. Temperature dependence of oxygen evolution transients of *Synechococcus* sp. PCC 7002 (blue), *Thermosynechococcus elongatus* BP-1 wild-type and PsbA3 (red and green) and spinach (black). The transients were measured at (A) 0 °C, (B) 20 °C and (C) 40 °C respectively, shown from 0 ms to 6 ms or 12 ms in order to highlight the rise time.**

### 5.2.4.1 Rate constant of the fast phase

The classic Arrhenius plot is based on Arrhenius equation $\ln(k) = \ln(A) - E_a/k_BT$, where $k$ is the rate constant, $A$ is the pre-exponential frequency factor, and $E_a$ is the activation energy. $A$ and $E_a$ are determined from the intercept (y-axis) and slope, respectively. It shows in the natural logarithm of the rate constant versus the reciprocal of temperature in Kelvin (see figures in Appendix G).

In this section the Arrhenius plots are presented alternatively in a logarithmic scale of the time constant versus the reciprocal of temperature in Kelvin (Figure 5.15). The fit parameters are shown in Table 5-2. The activation energy (or enthalpy) is often reported in the unit of kJ mol$^{-1}$. In this study, the electron volt, i.e. eV, is used. Thus the units from the referenced sources were converted into eV with kJ mol$^{-1}$ = 10.36 meV, so that the energies can be compared on the same scale.

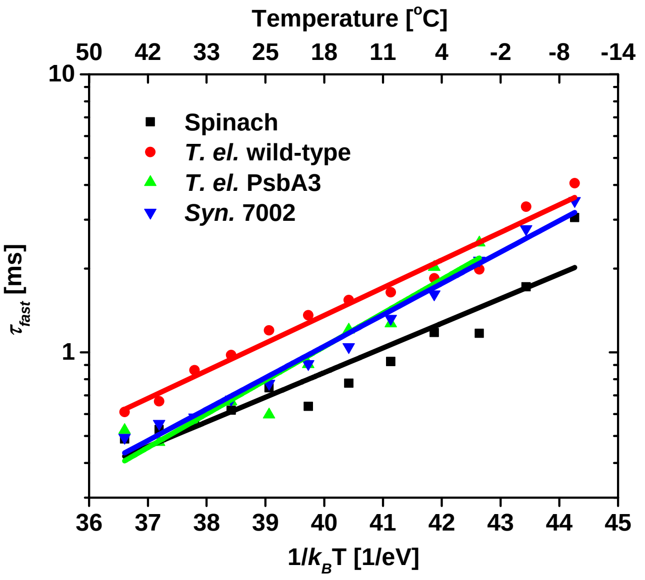

**Figure 5.15. Arrhenius plot of the time constants of the fast phase (a sum of the lag and pre phases), comparing PSIIs from *Synechococcus* sp. PCC 7002 (blue), *Thermosynechococcus elongatus* BP-1 wild-type (red) and PsbA3 (green) and spinach (black) from -10 °C to 45 °C, with increment of 5 °C. The lines are the linear fit of the data sets of corresponding colour. The classic Arrhenius plot in terms of rate constant $k_{\mathrm{fast}}$ can be found in Appendix G.**

**Table 5-2. Fit parameters of the Arrhenius plot (in Figure 5.15), comparing spinach, *Thermosynechococcus elongatus* BP-1 PSII-wild-type and PSII-PsbA3 and *Synechococcus* sp. PCC 7002. $\tau_{\mathrm{fast}}$ is the time constant of the fast phase at 20 °C; a and b are the slope and intercept from the linear regression, respectively, and $R^2$ is the fit deviation.**

| Species | $\tau_{\mathrm{fast}}$ at 20 °C [ms] | Slope (a) [K·s$^{-1}$] | Intercept (b) [s$^{-1}$] | $R^2$ |
|---|---|---|---|---|
| Spinach | 0.64 | 0.089 | -3.62 | 0.89 |
| *T. elongatus* PSII-wild-tpye | 1.36 | 0.100 | -3.85 | 0.97 |
| *T. elongates* PSII-PsbA3 | 0.91 | 0.121 | -4.82 | 0.93 |
| *Synechococcus* 7002 | 0.91 | 0.113 | -4.50 | 0.98 |

**Table 5-3. Fit parameters of the Arrhenius plot and the corresponding values of activation energy in comparison of *Synechococcus* sp. PCC 7002, *Thermosynechococcus elongatus* BP-1 wild-type and psbA3 and spinach. $\tau_{fast}$ is the fast phase measured at 20 °C at (a) pH 6.2 and (b) pH 6.5, *A* is the pre-exponential factor, $E_a$ is the activation energy, Δ*H* is the enthalpy, TΔ*S* is the entropic component (where T is absolute temperature in Kelvin), and Δ*G* is the Gibbs free energy. References: a is in this work and b is in (Bao & Burnap, 2015).**

| PSII source or variant | $\tau_{fast}$ at 20 °C [ms] | A [$s^{-1}$] | $E_a$ [meV] | $\Delta H^\ddagger$ [meV] | $- T\Delta S^\ddagger$ [meV] | ΔG [meV] | Reference |
|---|---|---|---|---|---|---|---|
| Spin. | 0.64 | $4.2*10^6$ | 205±23 | 180 | 384 | 564 | a |
| *Syn*. 7002 | 0.91 | $3.2*10^7$ | 261±10 | 236 | 333 | 569 | a |
| *Syn*. 6803 | 0.80 | $3.2*10^8$ | 321 | 297 | 273 | 571 | b |
| D1-V185N | 1.90 | $7.0*10^7$ | 311 | 289 | 309 | 598 | b |
| D1-D61N | 1.40 | $9.0*10^6$ | 250 | 223 | 365 | 588 | b |
| D1-D61A | 1.40 | $4.9*10^5$ | 173 | 148 | 438 | 586 | b |
| *T.el*. PSII-wt | 0.39 | $7.1*10^6$ | 230±13 | 205 | 371 | 575 | a |
| *T.el*. PSII-PsbA3 | 0.90 | $6.6*10^7$ | 279±27 | 254 | 314 | 568 | a |

### 5.2.4.2 Rate constant of the slow phase

Using the same approach as for the fast phase, the Arrhenius plot of the slow phase is presented in Figure 5.16 and the fit parameters are shown in Table 5-4.

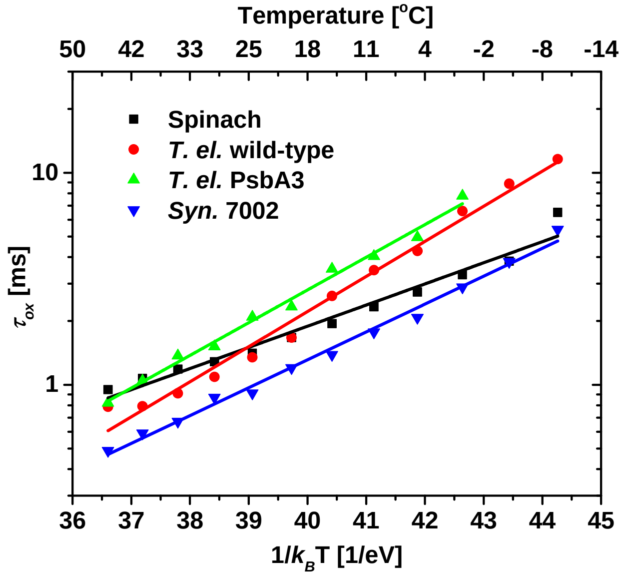

**Figure 5.16. Arrhenius plot of the time constant of the slow phase, comparing *Synechococcus* sp. PCC 7002 (blue), *Thermosynechococcus elongatus* BP-1 wild-type (red) and PsbA3 (green) and spinach (black) from -10 °C to 45 °C, with increment of 5 °C. The lines are the linear fit of the data sets in corresponding colour. The classic Arrhenius plot in terms of rate constant $k_{\text{fast}}$ can be found in Appendix G.**

**Table 5-4. Fit parameters of the Arrhenius plot (in Figure 5.16), comparing *Synechococcus* sp. PCC 7002, *Thermosynechococcus elongatus* BP-1 wild-type and PsbA3 and spinach. $\tau_{ox}$ is the time constant of the slow phase at 20 °C, a and b are the slope and intercept from the linear regression, respectively, and R$^2$ is the fit deviation.**

| PSII | $\tau_{ox}$ at 20 °C [ms] | Slope (a) [K·s$^{-1}$] | Intercept (b) [s$^{-1}$] | R$^2$ |
|---|---|---|---|---|
| Spinach | 1.67 | 0.067 | -2.43 | 0.93 |
| *T. elongatus* PSII-wild-tpye | 1.67 | 0.166 | -6.28 | 0.98 |
| *T. elongates* PSII-PsbA3 | 2.34 | 0.154 | -5.72 | 0.99 |
| *Synechococcus* 7002 | 1.20 | 0.099 | -3.71 | 0.99 |

The connection between kinetics and thermodynamics is usually explained by Marcus theory of electron transfer process (Marcus, 1993). Nevertheless, taking into account the evidence of this study and combining the report of *Synechocystis* sp. PCC 6803 (wild-type and D1 variants) and Ca-Sr exchange of the *Thermosynechococcus elongatus*, the correlation between activation energy and rate constant is not as strong as commonly acknowledged, see Table 5-5 for details. The basic characteristic of the cyanobacterial species can be seen in Table 5-1.

For the site-directed mutants D1-V185N, D61N and D61A the reactions are significantly slowed down (43 ms ± 8 ms) compared to the other wild type species (1.8 ms ± 0.6 ms), however, the activation enthalpies are relatively small. This suggests that the locally modified mutations affect the activation energy in different ways, but quantitatively in the same direction, i.e. they change the entropy contribution and lower the activation enthalpy. It is worthwhile to address that for both mesophilic cyanobacteria, as can be seen in Table 5-5, the activation energy ($E_a$) of *Synechococcus* 7002 in this study was determined as 307 meV in comparison to that of *Synechocystis* 6803 as 477 meV determined in (Bao & Burnap, 2015). This discrepancy is likely due to the different protein treatment of using one molar betaine (in *Syn*. 7002) rather than one molar sucrose (in *Syn*. 6803) prior to the measurement. Since the use of betaine instead of sucrose in the assay buffer was found to be able to increase the oxygen evolution activity by up to 40% (Schiller & Dau, 2000).

**Table 5-5. Fit parameters of the Arrhenius plot and the corresponding values of activation energy comparing *Synechococcus* sp. PCC 7002, *Thermosynechococcus elongatus* BP-1 wild-type and PsbA3 and spinach. $\tau_{ox}$ is the slow phase measured at 20 °C at (a) pH 6.2 and (b) pH 6.5, *A* is the pre-exponential factor, $E_a$ is the activation energy, $\Delta H$ is the enthalpy, T$\Delta S$ is the entropic component (where T is absolute temperature in Kelvin), and $\Delta G$ is the Gibbs free energy. References: a is in this work, b is in (Bao & Burnap, 2015), and c is in (Rappaport et al., 2011).**

| PSII variants | $\tau_{ox}$ [ms] | A [$s^{-1}$] | $E_a$ [meV] | $\Delta H^‡$ [meV] | - $T\Delta S^‡$ [meV] | $\Delta G$ [meV] | Ref. | Temp. range [°C] |
|---|---|---|---|---|---|---|---|---|
| Spin. | 1.67 | $5.2*10^6$ | 231 ± 13 | 206 | 379 | 584 | a | -10 - 45 |
| Spin.+ gly. | 1.60 | $3.4*10^5$ | 160 ± 13 | 135 | 459 | 594 | a | 0 - 30 |
| *T.el.* PSII-wt | 1.67 | $1.9*10^9$ | 383 ± 15 | 357 | 229 | 587 | a | -10 - 45 |
| *T.el.* PsbA3 | 2.34 | $5.3*10^8$ | 357 ± 12 | 332 | 262 | 593 | a | 0 - 45 |
| *Syn.* 7002 | 1.20 | $1.4*10^8$ | 304 ± 9 | 279 | 295 | 574 | a | -10 - 45 |
| *Syn.* 6803 | 1.70 | $5.2*10^{10}$ | 477 | 453 | 143 | 596 | b | 3 - 30 |
| D1-V185N | 45.4 | $1.9*10^5$ | 232 | 208 | 458 | 667 | b | 7 - 33 |
| D1-D61N | 35.5 | $1.5*10^9$ | 460 | 433 | 235 | 668 | b | 10 - 30 |
| D1-D61A | 50.8 | $3.3*10^7$ | 368 | 341 | 332 | 672 | b | 10 - 30 |
| *T.el.* Ca | 1.93 | $1.4*10^8$ | 317 | 342 | 295 | 586 | c | 5 - 40 |
| *T.el.* Sr ex. | 7.22 | $7.4*10^6$ | 275 | 300 | 369 | 619 | c | 5 - 40 |

It is surprising to find strong differences in the enthalpic and entropic contributions, even though the OECs of plants and cyanobacteria are reported to be highly conserved. Alignment of the amino acid sequences of the D1 protein subunit revealed a sequence identity of 84.7% (Glockner et al., 2013). This high conservation (especially in the vicinity of the OEC) suggests that the discovered variation in the activation enthalpy for the same chemical process of O-O bond formation is unlikely due to the structural differences in the subunits (both D1 and CP43). The enthalpy and entropy in different PSII variants (Table 5-5) suggest a linear correlation (with slope of -0.99 ± 0.03) between both components (ΔH and -TΔS) as can be seen in Figure 5.17.

This means the physiological optimum cold-adapted (or softer) PSIIs have a lower enthalpy and higher entropy (in negative sign) than the higher temperature adapted enzymes (e.g. thermophilic ones). This phenomenon was also suggested from earlier enzyme study (Siddiqui & Cavicchioli, 2006). As can be seen in Table 5-6, the characteristics of PSII species of cyanobacteria and plant presented in this study, in comparison with optimal growth temperature, ecosystem and protein treatment. Regarding spinach as a terrestrial species, the oxygen diffusion step evolving from PSII can be faster than the one from aquatic cyanobacteria, presumably because of the lower pressure from the surrounding water molecules.

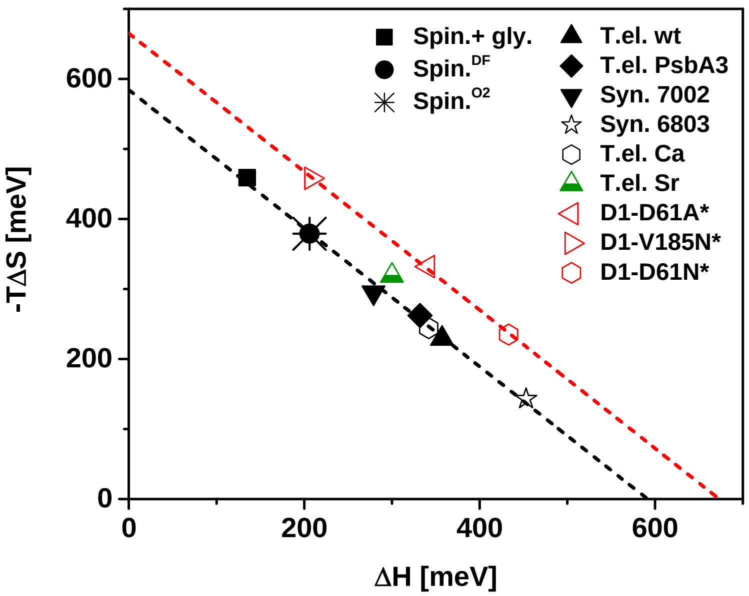

**Figure 5.17. Correlation of the change of entropic versus enthalpic components (ΔH vs. -TΔS) for PSII variants. The solid filled symbols represent the data from this study while the other legends are from the recalculated values from the reference sources.**

**Table 5-6. Characteristics of PSII species of cyanobacteria and plant, including *Thermosynechococcus elongatus* BP-1, *Synechococcus* sp. PCC 7002, *Synechocystis* sp. PCC 6803 and spinach in comparison with optimal growth temperature, ecosystem and protein treatment, respectively.**

| Characteristics | *T. elongatus* | *Syn.* 7002 | *Syn.* 6803 | spinach |
|---|---|---|---|---|
| Optimal growth | Thermophilic | Mesophilic | Mesophilic | Mesophilic |
| temperature | 60 °C | 38 °C | 30 °C | 20 °C |
| Ecosystem | Aquatic | Aquatic | Aquatic | Terrestrial |
| Protein treatment | Betaine | Betaine | Sucrose | Betaine |

## 5.3 Summary

In this chapter, the kinetics of O-O bond formation during the $S_3$ to $S_0$ transition of the different PSII variants were approached using the same method (time-resolved oxygen polarography) and measuring conditions. This avoids the uncertainties that are caused by comparing results using different techniques. Additionally, PSII from spinach (obtained by the same preparation protocol) was analyzed with another method (delayed fluorescence) and gave very comparable kinetics and the same activation energy. The given results indicate a likely isokinetic behaviour with divergent activation enthalpy among different PSII proteins, in such a way that the change of enthalpy is compensated by the variation of the entropy. This is defined as enthalpy-entropy compensation (EEC).

Intensive DFT calculations have shown that the O-O bond formation is rate limiting with a barrier of 11.3 kcal/mol (equivalent to 490 meV) from the resting $S_3^n$ to the $S_4^+$ state (Siegbahn, 2013) and the barrier could be possibly as low as 6.2 kcal/mol (equal to 269 meV) given the most efficient oxyl-oxo mechanism (Siegbahn, 2017). In contrast, various experimental evidence from studies of a few species as well as PSII-mutants revealed remarkable differences of activation energy (or enthalpy) in O-O bond formation; see details in Table 5-5 and Figure 5.17. This leaves an open question: Is it possible that this specific formation is not only dependent on the pure energetic barrier chemically, but also highly affected by the protein interior, particularly the water clusters?

The structure of the OEC is well conserved among cyanobacteria, green algae and plants. Therefore, the suggested differences in terms of the activation enthalpy or entropy cannot be probed by site-directed mutagenesis, which disturbs the water clusters by specific amino acid exchange. There may be reasons for those differences that are even more fundamental, especially when it comes to the formation of the transition states followed by the O-O bond formation. A hypothesis related to the transition state theory is under development and is to be discussed in the next chapter.

# Chapter 6 Mechanism of Enthalpy-Entropy Compensation

The phenomenon of enthalpy-entropy compensation (EEC) has been reported on micro- and macromolecular levels (such as proteins), despite frequent debates about its existence. There are several reports that provide experimental and theoretical evidence, for instance studies on protein-ligand association (Ferrante & Gorski, 2012; Lafont et al., 2007; Qian, 1998; Tzeng & Kalodimos, 2012). This fundamental thermodynamic behaviour can also be seen in the studies presented and discussed in Chapter 5. This brings me the opportunity to challenge and reveal the driving force of EEC in biological macro molecules.

In a recent review about EEC (Chodera & Mobley, 2013) based the calorimetric studies of the interaction between small molecules and biomolecular ligands, four basic mechanisms were summarized to explain the physical origin of the compensation as following: (i) solvent reorganization - a universal source, demonstrating a fundamental property of water-solvent interactions; (ii) conformational restriction of bound states, therefore sometimes EEC is not linear or severe; (iii) receptor flexibility, since the free energy change on the perturbation of the ligand or protein could be small, relative to the significant larger changes in enthalpy and entropy respectively; and (iv) the decomposition of free energy.

Classically, the cause of this phenomenon was analyzed from the thermodynamic quantities of enthalpy and entropy derived from either the Arrhenius or Eyring equation, see Section 1.3.3. Based on the classic transition state theory (TST), any chemical reaction has to cross a certain energetic barrier in order to achieve the transition state before the energetically downhill reaction forming the products. This barrier was usually determined by the transitional and vibrational movements (as well as the frequencies) of the conformational sub-states. However, there was a certain limitation to the accuracy of the classic TST, based on which a slope of an Arrhenius plot is proportional to the activation energy of the corresponding reaction kinetics. Even though a non-linear or bi-phasic behaviour of the Arrhenius plot was frequently and controversially reported, in which a discontinuity in terms of a kink between two temperature ranges (also called a breakpoint behaviour) was interpreted as evidence for the existence of an intermediate (Karge et al., 1997; Koike et al., 1987; Renger & Hanssum, 1992).

With regard to the kinetic and energetic correlation of the O-O bond formation in photosynthetic water oxidation, it has been reported as following:

(i) Altering the protein environment (non-local) by adding a cosolvent, e.g. 30% glycerol, resulted in a lower activation enthalpy (at room temperature), but had little effect on the kinetics. In Chapter 5, this iso-kinetic behaviour was also observed among different species, within which the OEC was highly conserved in the protein structure.

(ii) Local modifications related to the water cluster, such as Ca-Sr exchange and site-directed mutation at the second ligand sphere of the $Mn_4CaO_5$ cluster (D1-V185N, D61N and D61A), which may induce structural rearrangements, showed a significant lower rate constant, and a lower or unaffected enthalpy (Bao & Burnap, 2015).

This leads to the question whether the activation enthalpy is determined solely by the energetic barrier of the O-O bond formation step. If this is the case, any modification (e.g. site-directed mutations close to the OEC) that decelerates the reaction should accordingly increase the activation enthalpy. However, the enthalpy-entropy compensation was reported with drastic changes in activation enthalpy (see examples in Table 5-5), but, in contrast, with little variation of the rate constant around room temperature (as e.g. in this study). The following question would be, what could be the driving force of this phenomenon? Is this connected to the perturbation of the water clusters in the vicinity of OEC, particularly as each formation of oxygen is the contribution from two substrate water molecules (as can be seen in earlier Figure 1.4)?

In protein dynamics a large number of isoenergetic conformational substates could be formed following a complex energy landscape (Frauenfelder et al., 1991). Regarding the conformation of water clusters, any local or non-local perturbation of the water molecules may reshape the distribution of the sub-states, as well as the active conformation of the pre-transition state, called Pre-TS state hereafter. The classic scheme of transition state theory (Figure 1.6 in Section 1.3) is yet enough to explain the distribution of those conformational changes. Therefore, a semi-quantitative model is proposed in the following to explain the Pre-TS state in further details (Figure 6.1).

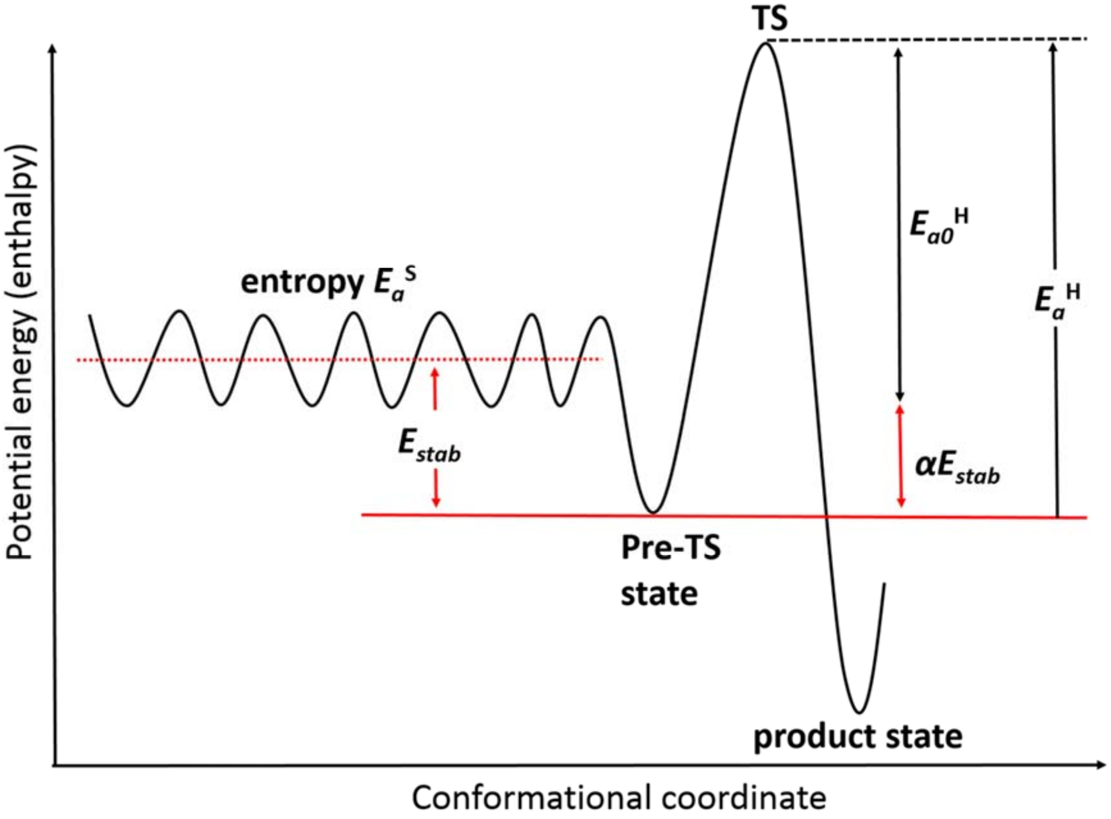

**Figure 6.1. A semi-quantitative model of potential energy (enthalpy) in correlation with conformational coordinate based on transition state theory. $E_a^S$ is entropy of activation, $E_{stab}$ is the energy between vibrational state and the stabilized activation conformation in Pre-TS, TS is transition state, $E_{a0}$ is the average internal energy of the reactant relative to the TS, α is a coefficient factor of $E_{stab}$, and $E_a^H$ is enthalpy of activation. More details are listed in Table 6 1.**

Assume N is the number of isoenergetic conformational sub-states, which are the local minima of the vibrational energy profile; $E_{a0}$ is the average internal energy of the reactant relative to the TS, $E_{Pre\text{-}TS}$ is the relative energy level of the Pre-TS state, and $E_{stab}$ is the energy difference between the vibrational energy and the stabilized Pre-TS state. Then the probability of the active conformation populating the Pre-TS state for a given stabilized energy ($E_{stab}$) is determined by

$$P = \frac{e^{-\beta E_{Pre-TS}}}{N \cdot e^{-\beta E_{a0}} + e^{-\beta E_{Pre-TS}}} = \frac{1}{1 + N \cdot e^{-\beta E_{stab}}}, \tag{6.1}$$

where the thermodynamic beta, β, is equivalent to $1/k_BT$. The total activation enthalpic barrier $E_a^H$ between the Pre-TS and TS state is the sum of $E_{a0}$ and $\alpha \cdot E_{stab}$, where α is a coefficient factor (see Figure

6.1 and Table 6-1). Then according to Eq. (1.6) in TST (introduced in Section 1.3) the rate constant of the reaction, $k$, is dependent on the vibrational frequency, activation barrier and the probability of achieving the pre-TS as following

$$\begin{aligned} k &= f \cdot e^{-\beta(E_{a0}+\alpha E_{stab})} \cdot P \\ &= f \cdot e^{-\beta(E_{a0}+\alpha E_{stab})} \cdot \frac{1}{1+N \cdot e^{-\beta E_{stab}}}, \end{aligned} \tag{6.2}$$

where $f = k_B T/h$, $E_a^S = -T\Delta S$, $h$ is the Planck constant, $k_B$ is the Boltzmann constant, T is the temperature, ΔS is the entropy change to form the transition state. So the rate constant is proportional to the Boltzmann distribution of the energy factor and probability of forming the active Pre-TS, which are highly dependent on the stabilized energy (an example of the correlations is shown in Figure 6.2). This suggests that the kinetics of the O-O bond formation is more complicated than the explanation of classic TST. However, a simple semi-quantitative model may help to address this mechanism in a reasonable approach.

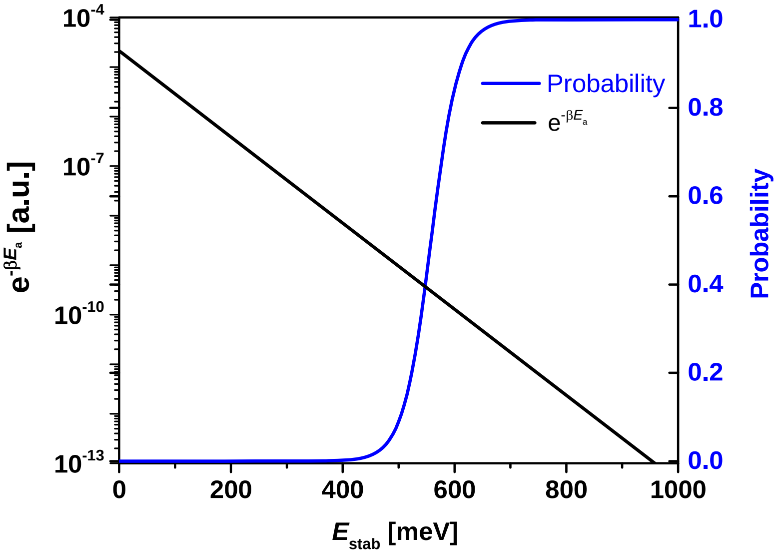

**Figure 6.2. An example of the correlation of activation energy factor and probability versus the stabilized energy of the activation, based on Eq. (6.1), (6.2), (6.6) and (6.7), assuming $N_0 = 5*10^9$, c = 0, $\alpha$ = 0.5 and $E_{a0}$ = 280 meV.**

The Eyring equation represents the contribution of enthalpic and entropic components of the activation energy to the rate constant:

$$\begin{aligned} k &= f \cdot e^{-\beta \Delta G} \\ &= f \cdot e^{-\beta E_a^H} \cdot e^{-\beta E_a^S} \ , \end{aligned} \tag{6.3}$$

which $\Delta G = E_a^H + E_a^S$. Accordingly, taking the natural logarithm of both sides of Eq. (6.3), it gives

$$\begin{aligned} \ln(k) &= \ln(f) - \beta(E_a^H) - \beta(E_a^S) \\ &= \ln(f) - \beta(E_a^H) + \frac{\Delta S}{k_B} . \end{aligned} \tag{6.4}$$

As introduced in Section 1.3.3, both functions of the enthalpy and entropy could be resolved by doing differential calculus of *k* to β, i.e. d(ln*k*)/dβ. This gives an expression of both functions where the slope is linear to the enthalpy, while the intercept correlates to the frequency factor as well as the entropy. The enthalpy of activation can thus be derived by:

$$\frac{d\ln(k)}{d\beta} = -E_a^H \ . \tag{6.5}$$

So by combining equations (6.2) and (6.5) it gives

$$\begin{aligned} E_a^H &= -\frac{d\ln(k)}{d\beta} \\ &= (E_{a0} + \alpha E_{stab}) + \frac{d\ln(P)}{d\beta} \\ &= (E_{a0} + \alpha E_{stab}) - (1 - P)E_{stab} \ . \end{aligned} \tag{6.6}$$

Derived Eq. (6.4) and combining it with Eq. (6.6), gives the entropy of activation

$$\begin{aligned} E_a^S &= \frac{\ln(f)}{\beta} - \frac{\ln(k)}{\beta} - E_a^H \\ &= \frac{\ln(f)}{\beta} - \frac{\ln(k)}{\beta} - \frac{d\ln(k)}{d\beta} \ . \end{aligned} \tag{6.7}$$

See Table 6-1 for all the parameters with physical definition.

**Table 6-1. Parameters used in semi-quantitative model based on transition state theory with physical definition and numerical value range at ambient temperature. See model scheme in Figure 6.1.**

| Parameter | Physical definition | Numerical value | Unit |
|---|---|---|---|
| $E_{a0}$ | Average internal energy of the reactant relative to the TS | [100, 400] | meV |
| $E_{stab}$ | Energy between vibrational state to the stabilized activation conformation in Pre-TS | [0, 1000] | meV |
| $\alpha$ | Coefficient factor of $E_{stab}$ | [0, 1] | - |
| P | Probability of achieving the Pre-TS | [0, 1] | - |
| N | Number of isoenergetic conformational substates | [0, infinite] | - |
| $\beta$ | thermodynamic beta | $= 1/k_B T$ | $meV^{-1}$ |
| $f$ | Vibrational frequency | $6.2*10^{12}$ (at 20 °C) | $s^{-1}$ |
| $E_a^H$ | Enthalpy of activation | [0, 1000] | meV |
| $E_a^S$ | Entropy of activation | [0, 1000] | meV |
| $\Delta G$ | Free energy of activation | [0, 1000] | meV |
| $\Delta S$ | The entropy change to form the transition state | [0, 4] | $meV\cdot K^{-1}$ |

So in a given isokinetic conformation N, the internal energy of the reactant $E_{a0}$ and coefficient factor α, the activation energy factor and probability of achieving the Pre-TS (Figure 6.2) as well as the rate constant and the enthalpic and entropic components could be presented as a function of $E_{stab}$ (Figure 6.3). Highlighted in green in Figure 6.3 is a range of $E_{stab}$ (for this specific example), in which a high variation of the enthalpy results only in a small change of the rate constant (about 1.5 times); the same is true for variation of the entropy in that range but in the opposite direction. This suggests a phenomenon of enthalpy-entropy compensation within the regime (highlighted in green) when the stabilized energy is between 520 meV and 600 meV. In this energy range, the correlation between enthalpy and entropy is close to a linear regression (WT in Figure 6.4). Regarding locally modified mutations, it requires more efforts to form a pre-transition state than in the naturally optimized wild-type species. The mutants show a bigger number of isoenergetic conformational substates and more stabilized energy is needed to achieve the proper conformation prior to the transition state. The fit parameters are listed in Table 6-2.

This shows that the EEC behavior is very comparable to the experimental findings in Figure 5.17, where the thermodynamic components of O-O bond formation are addressed with respect to both non-local and local alternation of water clusters inside the PSII protein system (wild-type and mutant, respectively).

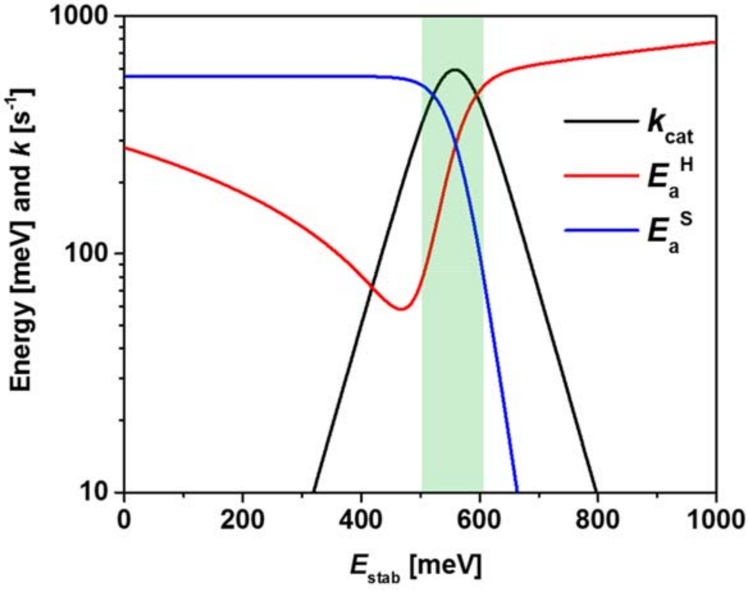

**Figure 6.3. An example of the correlation of rate constant, enthalpy and entropy versus the stabilized energy of the activation, based on Eq. (6.1), (6.2), (6.6) and (6.7), assuming N = 5*10$^9$, $\alpha$ = 0.5 and $E_{a0}$ = 280 meV.**

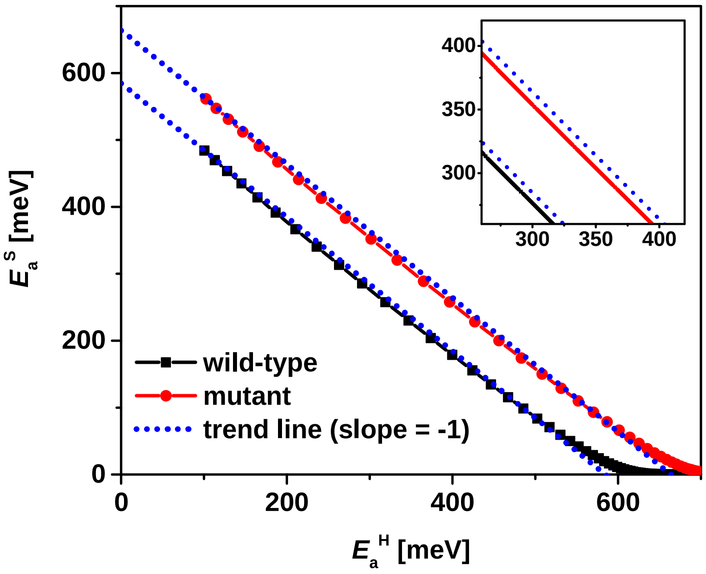

**Figure 6.4. Correlation of the change of entropic versus enthalpic components ($E_a^H$ vs. $E_a^S$). For wild-type species (in black) $E_{stab}$ = 520 meV to 600 meV, where N = 5*10$^9$, and $E_{a0}$ = 280 meV within the regime highlighted in green colour in Figure 6.3. In parallel, for site-directed mutations (in red) $E_{stab}$ = 585 meV to 675 meV, where N = 1*10$^{11}$, and $E_{a0}$ = 320 meV. The points indicate a spacing of $E_{stab}$ = 5 meV. A trend line (dotted in blue) with a slope of -1 shows a linear regression as reference.**

**Table 6-2. Fit parameters of the proposed model based on transition state theory. The model applies to both PSII wild-type and mutant, where N is the number of isoenergetic conformational sub-states, $E_{stab}$ is the energy between vibrational state and the stabilized activation conformation in Pre-TS, and $E_{a0}$ is the average internal energy of the reactant relative to the TS.**

| Fit parameter | N | $E_{stab}$ [meV] | $E_{a0}$ [meV] |
|---|---|---|---|
| Wild-type | $5 * 10^9$ | 520 - 600 | 270 |
| Mutant | $1 * 10^{11}$ | 585 - 675 | 320 |

The stabilized energy of approximately 600 meV is equivalent to that needed to break at least three hydrogen bonds, since the energy required for breaking the bond is varying between 62 meV to 240 meV depending on the estimated models (Smith et al., 2004; Suresh & Naik, 2000).

This means that during the reconstruction of the water clusters inside the PSII system the O-O bond formation takes place after breaking three hydrogen bonds or more. The mutations may decrease the stabilized energy enormously and form more isoenergetic states, thus slow down the reaction kinetics (with a factor of 20 - 30) compared to the wild type. Nevertheless, for different softness of the protein environment, the protein water interaction cannot be fully excluded.

The model fits the experimental observation in EEC of both the wild-type and mutated PSII species, i.e. the non-local and local modification altered protein matrix, respectively. It explains the driving force of the EEC from the perspectives of the energy levels and probability in achieving a pre-transition state prior to the O-O bond formation. The model suggests that the experimentally observed enthalpy-entropy compensation may relate to evolutionary optimisation stability of the pre-transition state. A qualitatively similar explanation may be applicable to many other enzymatic processes.

# Chapter 7 Summary and Outlook

## 7.1 Summary

In this thesis, results on the mechanism of O-O bond formation in photosynthetic water oxidation by photosystem II (PSII) are reported. The investigations were performed experimentally using three time-resolved techniques established previously (by the research group of Prof. Holger Dau). All three methods involve the excitation with sequence of light flashes (of nanosecond or microsecond duration) and detection of time courses typically in the time domain from about 10 μs to 500 ms that reflect functionally crucial processes in PSII. These three investigated "PSII signals" are: (1) variable PSII fluorescence (prompt chlorophyll fluorescence), (2) delayed (recombination) fluorescence of PSII, and (3) time-resolved oxygen polarography.

Firstly, in Chapter 3 close to 50% inhibition of oxygen evolving activity was found in both cyanobacterial and plant PSII using ammonia as a substrate analogue. Therefore, an anti-cooperative binding model was proposed for the first time wherein the ammonia binds at two different potential substrate water sites at the oxygen evolving complex (OEC). The model reconciles many aspects of the large body of experimental results on ammonia binding to PSII reported since 1975. The results of this study were published in the journal *Biochemistry* in 2017 (as co-first author).

Secondly, in Chapter 4 glycerol was used as a cosolvent to probe the conformational changes near the OEC. The kinetics of proton and electron transfers were significantly affected by the presence of glycerol in the assay buffer. O-O bond formation is stabilized within 30% glycerol, but decelerated at higher concentration. Investigation of the glycerol influence on the temperature dependence of PSII reactions revealed that the activation enthalpy of O-O bond formation was significantly decreased in the presence of (30%) glycerol. However, a compensating increase in the activation entropy resulted in approximately the same overall rate constant of O-O bond formation. These results motivated the investigation into the activation energy of this O-O bond formation step in greater detail. Conformational changes induced by glycerol in PSII may be analogous the differences among PSII variants derived from several biological and environmental backgrounds.

Thirdly, in Chapter 5 the activation energy of O-O bond formation was compared among four PSII variants: spinach, *Synechococcus* sp. PCC 7002 and both wild-type and PsbA3 isoform of *Thermosynechococcus elongatus* BP-1. Combining the new findings in Chapter 4 and revisiting the given reports in literature, including the second sphere site-directed mutation and Ca-Sr replacement PSII, a phenomenon of enthalpy-entropy compensation (EEC) of O-O bond formation was observed.

Lastly, based on the experimental evidence for EEC a semi-quantitative model was newly proposed in Chapter 6, rooting in transition state theory (Eyring equation). The model fits the experimental observation in EEC of both the wild-type and mutated PSII species, i.e. the non-local and local modification altered protein matrix, respectively. It explains the driving force of the EEC from the perspectives of the energy levels and probability in achieving a pre-transition state prior to the O-O bond formation. The model suggests that the experimentally observed enthalpy-entropy compensation may relate to evolutionary optimisation stability of the pre-transition state. A qualitatively similar explanation may be applicable to many other enzymatic processes.

## 7.2 Outlook on future research directions

The presented results of this thesis provide significant new information that supports our mechanistic understanding of O-O bond formation in photosynthetic water oxidation. Obviously, this single study cannot answer all open questions. But it can open up new windows for future research. Some open questions that could be addressed in the coming years are listed in the following.

**(i)** What about other cosolvents, with similar molecular structures as glycerol, do they interact with the water clusters and thus lower the activation enthalpy in a similar way?

**(ii)** Like ammonia, also methanol is a hydrophilic cosolvent, which has been suggested to exhibit direct binding to the Mn-complex, therefore affecting O-O bond formation (Noring et al., 2008a; Su et al., 2011). Can one get more clues from investigation of methanol binding using a similar approach as in the ammonia study of Chapter 3?

**(iii)** The ammonia binds either to W1 or W2, one of which is likely to be a water substrate. Does ammonia binding lower or raise the energetic barrier of O-O bond formation (increase activation enthalpy) even though room-temperature rate constant of O-O bond formation is not affected?

**(iv)** Is the enthalpy-entropy compensation phenomenon universally observed also for other reactions in photosynthesis and in general?

As introduced in Section 1.2, the PSII community is stepping very close into the crystal structure of individual S-state after decades of efforts by countless scientists working together. The protein structure could possibly be resolved without radiation damage by employing pulsed free-electron laser (FEL) crystallography. Presumably with well resolved atomic structures of all semi-stable S-states and hopefully also of intermediate, only transiently formed states, one could possibly develop a clearer idea about the mechanism of the O-O bond formation by distinguishing between the two highly debated candidates (the oxo-oxyl radical coupling versus the nucleophilic water attack mechanism) in today's commonly accepted hypothesis. However, there will remain important knowledge gaps:

**(i)** Much of our understanding of the O–O bond formation comes from computational studies rooting in crystallographic models of the atomic structure. Which experiments could be designed to confirm or reject the hypotheses generated from theory? Are structural studies (e.g. femtosecond X-ray crystallography) sufficient to understand the role of proton movements and protein dynamics? Is the combination of structural studies with computational chemistry sufficient to address the role of "rare states" that could be functionally decisive?

**(ii)** How can a deeper understanding of the OEC function bridge towards the design of synthetic catalysts for artificial water oxidation? How can one get closer to mimicking the performance of the natural system?

In my opinion, searching for the meaning of life is never easy. It may be equally challenging to understand photosynthetic water oxidation in fine detail. It requires not only powerful scientific methods, but also researchers with experience, fitness and determination. Note that each beautiful journey has an end. But every ending can lead the way into a new world.

To be continued, in my academic career.

# References

Åhrling, K. A., Evans, M. C. W., Nugent, J. H. A., & Pace, R. J. (2004). The two forms of the S2 state multiline signal in Photosystem II: effect of methanol and ethanol. *Biochimica et Biophysica Acta (BBA) - Bioenergetics, 1656*(1), 66-77.

Allakhverdiev, S. I., Karacan, M. S., Somer, G., Karacan, N., Khan, E. M., Rane, S. Y., . . . Renger, G. (1994). Reconstitution of the water-oxidizing complex in manganese-depleted photosystem II complexes by using synthetic binuclear manganese complexes. *Biochemistry, 33*(40), 12210-12214.

Amunts, A., Drory, O., & Nelson, N. (2007). The structure of a plant photosystem I supercomplex at 3.4 angstrom resolution. *Nature, 447*(7140), 58-63.

Ananyev, G., Nguyen, T., Putnam-Evans, C., & Dismukes, G. C. (2005). Mutagenesis of CP43-arginine-357 to serine reveals new evidence for (bi)carbonate functioning in the water oxidizing complex of Photosystem II. *Photochem Photobiol Sci, 4*(12), 991-998.

Andréasson, L. E., Hansson, O., & von Schenck, K. (1988). The interaction of ammonia with the photosynthetic oxygen-evolving system. *Biochimica et Biophysica Acta, 936*(3), 351-360.

Andréasson, L. E., & Lindberg, K. (1992). The inhibition of photosynthetic oxygen evolution by ammonia probed by EPR. *Biochimica et Biophysica Acta, 1100*(2), 177-183.

Arakawa, T., & Timasheff, S. N. (1982). Mechanism of Stabilization of Proteins by Glycerol and Sucrose. *Seikagaku, 54*(11), 1255-1259.

Askerka, M., Brudvig, G. W., & Batista, V. S. (2017). The O-2-Evolving Complex of Photosystem II: Recent Insights from Quantum Mechanics/Molecular Mechanics (QM/MM), Extended X-ray Absorption Fine Structure (EXAFS), and Femtosecond X-ray Crystallography Data. *Accounts of Chemical Research, 50*(1), 41-48.

Askerka, M., Vinyard, D. J., Brudvig, G. W., & Batista, V. S. (2015). NH3 Binding to the S-2 State of the O-2-Evolving Complex of Photosystem II: Analogue to H2O Binding during the S-2 -> S-3 Transition. *Biochemistry, 54*(38), 5783-5786.

Baker, N. R. (2008). Chlorophyll fluorescence: A probe of photosynthesis in vivo. *Annual Review of Plant Biology, 59*, 89-113.

Bao, H., & Burnap, R. L. (2015). Structural rearrangements preceding dioxygen formation by the water oxidation complex of photosystem II. *Proceedings of the National Academy of Sciences of the United States of America, 112*(45), E6139-E6147.

Baranov, S. V., Tyryshkin, A. M., Katz, D., Dismukes, G. C., Ananyev, G. M., & Klimov, V. V. (2004). Bicarbonate is a native cofactor for assembly of the manganese cluster of the photosynthetic water oxidizing complex. Kinetics of reconstitution of O2 evolution by photoactivation. *Biochemistry, 43*(7), 2070-2079.

Barber, J., Mauro, S., & Lannoye, R. (1977). The relationship between the yield factors for prompt and delayed fluorescence. *Febs Letters, 80*(2), 449-454.

Beck, W. F., Depaula, J. C., & Brudvig, G. W. (1986). Ammonia Binds to the Manganese Site of the O-2-Evolving Complex of Photosystem-Ii in the S-2 State. *Journal of the American Chemical Society, 108*(14), 4018-4022.

Berthold, D. A., Babcock, G. T., & Yocum, C. F. (1981). A Highly Resolved, Oxygen-Evolving Photosystem-II Preparation from Spinach Thylakoid Membranes - Electron-Paramagnetic-Res and Electron-Transport Properties. *Febs Letters, 134*(2), 231-234.

Blankenship, R. E. (2002). *Molecular mechanisms of photosynthesis*. Oxford, England: Blackwell Science.

Blankenship, R. E., Babcock, G. T., & Sauer, K. (1975). Kinetic study of oxygen evolution parameters in Triswashed, reactivated chloroplasts. *Biochimica et Biophysica Acta, 387*(1), 165-175.

Borsarelli, C. D., & Braslavsky, S. E. (1998). Volume Changes Correlate with Enthalpy Changes during the Photoinduced Formation of the 3MLCT State of Ruthenium(II) Bipyridine Cyano Complexes in the Presence of Salts. A Case of the Entropy−Enthalpy Compensation Effect†. *The Journal of Physical Chemistry B, 102*(32), 6231-6238.

Boussac, A., Rutherford, A. W., & Styring, S. (1990). Interaction of ammonia with the water Splitting enzyme of photosystem II. *Biochemistry, 29*(1), 24-32.

Bovi, D., Narzi, D., & Guidoni, L. (2013). The $S_2$ state of the oxygen-evolving complex of Photosystem II explored by QM/MM dynamics: Spin surfaces and metastable states suggest a reaction path towards the $S_3$ state. *Angewandte Chemie International Edition, 52*(45), 11744-11749.

Buchta, J., Grabolle, M., & Dau, H. (2007). Photosynthetic dioxygen formation studied by time-resolved delayed fluorescence measurements--method, rationale, and results on the activation energy of dioxygen formation. *Biochimica et Biophysica Acta, 1767*, 565-574.

Canchi, D. R., & Garcia, A. E. (2013). Cosolvent Effects on Protein Stability. *Annual Review of Physical Chemistry, Vol 64, 64*, 273-293.

Capone, M., Narzi, D., Bovi, D., & Guidoni, L. (2016). Mechanism of Water Delivery to the Active Site of Photosystem II along the S-2 to S-3 Transition. *Journal of Physical Chemistry Letters, 7*(3), 592-596.

Chodera, J. D., & Mobley, D. L. (2013). Entropy-Enthalpy Compensation: Role and Ramifications in Biomolecular Ligand Recognition and Design. *Annual Review of Biophysics, Vol 42, 42*, 121-142.

Clausen, J., Debus, R. J., & Junge, W. (2004). Time-resolved oxygen production by PSII: Chasing chemical intermediates. *Biochimica et Biophysica Acta, 1655*(1-3), 184-194.

Cox, N., Rapatskiy, L., Su, J.-H., Pantazis, D. A., Sugiura, M., Kulik, L., . . . Messinger, J. (2011). Effect of $Ca^{2+}/Sr^{2+}$ substitution on the electronic structure of the oxygen-evolving complex of Photosystem II: A combined multifrequency EPR, $^{55}$Mn-ENDOR, and DFT study of the $S_2$ state. *Journal of the American Chemical Society, 133*(10), 3635-3648.

Cox, N., Retegan, M., Neese, F., Pantazis, D. A., Boussac, A., & Lubitz, W. (2014). Photosynthesis. Electronic structure of the oxygen-evolving complex in photosystem II prior to O-O bond formation. *Science, 345*(6198), 804-808.

Dashnau, J. L., Nucci, N. V., Sharp, K. A., & Vanderkooi, J. M. (2006). Hydrogen bonding and the cryoprotective properties of glycerol/water mixtures. *Journal of Physical Chemistry B, 110*(27), 13670-13677.

Dau, H. (1994). Molecular mechanisms and quantitative models of variable photosystem II fluorescence. *Photochemistry and Photobiology, 60*(1), 1-23.

Dau, H., Andrews, J. C., Roelofs, T. A., Latimer, M. J., Liang, W., Yachandra, V. K., . . . Klein, M. P. (1995). Structural consequences of ammonia binding to the manganese center of the photosynthetic oxygen-evolving complex: an X-ray absorption spectroscopy study of isotropic and oriented photosystem II particles. *Biochemistry, 34*(15), 5274-5287.

Dau, H., & Haumann, M. (2008). The manganese complex of photosystem II in its reaction cycle—basic framework and possible realization at the atomic level. *Coordination Chemistry Reviews, 252*(3-4), 273-295.

Dau, H., & Sauer, K. (1996). Exciton equilibration and photosystem II exciton dynamics - a fluorescence study on photosystem II membrane particles of spinach. *Biochimica et Biophysica Acta, 1273*(2), 175-190.

Dau, H., & Zaharieva, I. (2009). Principles, efficiency, and blueprint character of solar-energy conversion in photosynthetic water oxidation. *Accounts of Chemical Research, 42*(12), 1861-1870.

Dau, H., Zaharieva, I., & Haumann, M. (2012). Recent developments in research on water oxidation by photosystem II. *Current Opinion in Chemical Biology, 16*(1–2), 3-10.

Davis-Searles, P. R., Saunders, A. J., Erie, D. A., Winzor, D. J., & Pielak, G. J. (2001). Interpreting the effects of small uncharged solutes on protein-folding equilibria. *Annual Review of Biophysics and Biomolecular Structure, 30*, 271-306.

de Grooth, B. G., & van Gorkom, H. J. (1981). External electric field effects on prompt and delayed fluorescence in chloroplasts. *Biochimica et Biophysica Acta, 635*(3), 445-456.

De Las Rivas, J., Balsera, M., & Barber, J. (2004). Evolution of oxygenic photosynthesis: genome-wide analysis of the OEC extrinsic proteins. *Trends in Plant Science, 9*(1), 18-25.

de Wijn, R., & van Gorkom, H. J. (2001). Kinetics of electron transfer from $Q_a$ to $Q_b$ in photosystem II. *Biochemistry, 40*(39), 11912-11922.

Dilbeck, P. L., Hwang, H. J., Zaharieva, I., Gerencser, L., Dau, H., & Burnap, R. L. (2012). The mutation D1-D61N in Synechocystis sp. PCC 6803 allows the observation of pH-sensitive intermediates in the formation and release of $O_2$ from Photosystem II. *Biochemistry, 51*(6), 1079–1091.

Dixon, D., Habereder, A., Farmand, M., Kaserer, S., Roth, C., & Ramaker, D. E. (2012). Space Resolved, in Operando X-ray Absorption Spectroscopy: Investigations on Both the Anode and Cathode in a Direct Methanol Fuel Cell. *Journal of Physical Chemistry C, 116*(13), 7587-7595.

Fang, C. H., Chiang, K. A., Hung, C. H., Chang, K. J., Ke, S. C., & Chu, H. A. (2005). Effects of ethylene glycol and methanol on ammonia-induced structural changes of the oxygen-evolving complex in photosystem II. *Biochemistry, 44*(28), 9758-9765.

Ferrante, A., & Gorski, J. (2012). Enthalpy-Entropy Compensation and Cooperativity as Thermodynamic Epiphenomena of Structural Flexibility in Ligand-Receptor Interactions. *Journal of Molecular Biology, 417*(5), 454-467.

Ferreira, K. N., Iverson, T. M., Maghlaoui, K., Barber, J., & Iwata, S. (2004). Architecture of the photosynthetic oxygen-evolving center. *Science, 303*, 1831-1838.

Frauenfelder, H., Sligar, S. G., & Wolynes, P. G. (1991). The energy landscapes and motions of proteins. *Science, 254*(5038), 1598-1603.

Gekko, K., & Timasheff, S. N. (1981). Thermodynamic and Kinetic Examination of Protein Stabilization by Glycerol. *Biochemistry, 20*(16), 4677-4686.

Gerencser, L., & Dau, H. (2010). Water Oxidation by Photosystem II: H2O−D2O Exchange and the Influence of pH Support Formation of an Intermediate by Removal of a Proton before Dioxygen Creation. *Biochemistry, 49*(47), 10098-10106.

Ghanotakis, D. F., Babcock, G. T., & Yocum, C. F. (1984). Calcium Reconstitutes High-rates of Oxygen Evolution In Polypeptide Depleted Photosystem-ii Preparations. *Febs Letters, 167*(1), 127-130.

Glockner, C., Kern, J., Broser, M., Zouni, A., Yachandra, V., & Yano, J. (2013). Structural changes of the oxygen-evolving complex in photosystem II during the catalytic cycle. *J Biol Chem, 288*(31), 22607-22620.

Goltsev, V., Zaharieva, I., Chernev, P., Kouzmanova, M., Kalaji, H. M., Yordanov, I., . . . Strasser, R. J. (2012). Drought-induced modifications of photosynthetic electron transport in intact leaves: Analysis and use of neural networks as a tool for a rapid non-invasive estimation. *Biochimica Et Biophysica Acta-Bioenergetics, 1817*(8), 1490-1498.

Goltsev, V., Zaharieva, I., Chernev, P., & Strasser, R. J. (2009). Delayed fluorescence in photosynthesis. *Photosynthesis Research, 101*(2-3), 217-232.

Grabolle, M. (2005). Die Donorseite des Photosystems II: Rekombinationsfluoreszenz- und Röntgenabsorptionsstudien (thesis). *Fachbereich Physik, Freie Univ. Berlin,* http://www.diss.fu-berlin.de/2005/174/.

Grabolle, M., & Dau, H. (2005). Energetics of primary and secondary electron transfer in Photosystem II membrane particles of spinach revisited on basis of recombination-fluorescence measurements. *Biochimica et Biophysica Acta, 1708*(2), 209-218.

Grabolle, M., & Dau, H. (2007). Efficiency and role of loss processes in light-driven water oxidation by PSII. *Physiologia Plantarum, 131*, 50-63.

Haddy, A. (2007). EPR spectroscopy of the manganese cluster of photosystem II. *Photosynthesis Research, 92*(3), 357-368.

Halverson, K. M., & Barry, B. A. (2003). Sucrose and glycerol effects on photosystem II. *Biophysical Journal, 85*(2), 1317-1325.

Han, P., & Bartels, D. M. (1996). Temperature dependence of oxygen diffusion in H2O and D2O. *Journal of Physical Chemistry, 100*(13), 5597-5602.

Haumann, M., Hundelt, M., Jahns, P., Chroni, S., Bogershausen, O., Ghanotakis, D., & Junge, W. (1997). Proton release from water oxidation by photosystem II: similar stoichiometries are stabilized in thylakoids and PSII core particles by glycerol. *Febs Letters, 410*(2-3), 243-248.

Haumann, M., Liebisch, P., Muller, C., Barra, M., Grabolle, M., & Dau, H. (2005). Photosynthetic $O_2$ formation tracked by time-resolved x-ray experiments. *Science, 310*(5750), 1019-1021.

Heimann, S., Ponamarev, M. V., & Cramer, W. A. (2000). Movement of the Rieske iron-sulfur protein in the p-slide bulk aqueous phase: Effect of lumenal viscosity on redox reactions of the cytochrome b(6)f complex. *Biochemistry, 39*(10), 2692-2699.

Ho, F. M., & Styring, S. (2008). Access channels and methanol binding site to the CaMn4 cluster in Photosystem II based on solvent accessibility simulations, with implications for substrate water access. *Biochim Biophys Acta, 1777*(2), 140-153.

Hoff, A. J., & Amesz, J. (1995). Energy-Transfer and Stabilization in Plants and Bacterial Photosynthetic Reaction Centers - Preface. *Chemical Physics, 194*(2-3), R3-R4.

Hou, H. J. M., & Mauzerall, D. (2011). Listening to PS II: Enthalpy, entropy, and volume changes. *Journal of Photochemistry and Photobiology B: Biology, 104*(1-2), 357-365.

Hou, L. H., Wu, C. M., Huang, H. H., & Chu, H. A. (2011). Effects of Ammonia on the Structure of the Oxygen-Evolving Complex in Photosystem II As Revealed by Light-Induced FTIR Difference Spectroscopy. *Biochemistry, 50*(43), 9248-9254.

Hussels, M., & Brecht, M. (2011a). Effect of Glycerol and PVA on the Conformation of Photosystem I. *Biochemistry, 50*(18), 3628-3637.

Hussels, M., & Brecht, M. (2011b). Evidence for direct binding of glycerol to photosystem I. *Febs Letters, 585*(15), 2445-2449.

Isgandarova, S., Renger, G., & Messinger, J. (2003). Functional Differences of Photosystem II from Synechococcus elongatus and Spinach Characterized by Flash Induced Oxygen Evolution Patterns. *Biochemistry, 42*(30), 8929 - 8938.

Ishikita, H., Saenger, W., Loll, B., Biesiadka, J., & Knapp, E. W. (2006). Energetics of a possible proton exit pathway for water oxidation in photosystem II. *Biochemistry, 45*(7), 2063-2071.

Joliot, P., & Joliot, A. (1968). Analysis of the interactions between the two photosystems in isolated chloroplasts. *Biochimica et Biophysica Acta, 153*(3), 635-652.

Jursinic, P., & Govindjee. (1977). Temperature dependence of delayed light emission in the 6 to 340 microsecond range after a single flash in chloroplasts. *Photochem Photobiol, 26*(1977), 617-628.

Karge, M., Irrgang, K. D., & Renger, G. (1997). Analysis of the reaction coordinate of photosynthetic water oxidation by kinetic measurements of 355 nm absorption changes at different temperatures in photosystem II preparations suspended in either H2O or D2O. *Biochemistry, 36*(29), 8904-8913.

Karge, O., Bondar, A. N., & Dau, H. (2014). Cationic screening of charged surface groups (carboxylates) affects electron transfer steps in photosystem-II water oxidation and quinone reduction. *Biochim Biophys Acta, 1837*(10), 1625-1634.

Keith Wilson, J. W. (2010). *Principles and Techniques of Biochemistry and Molecular Biology*.

Kern, J., Tran, R., Alonso-Mori, R., Koroidov, S., Echols, N., Hattne, J., . . . Yachandra, V. K. (2014). Taking snapshots of photosynthetic water oxidation using femtosecond X-ray diffraction and spectroscopy. *Nat Commun, 5*, 4371.

Klauss, A., Haumann, M., & Dau, H. (2012). Alternating electron and proton transfer steps in photosynthetic water oxidation. *Proceedings of the National Academy of Sciences of the United States of America, 109*(40), 16035-16040.

Klauss, A., Krivanek, R., Dau, H., & Haumann, M. (2009). Energetics and kinetics of photosynthetic water oxidation studied by photothermal beam deflection (PBD) experiments. *Photosynthesis Research, 102*(2-3), 499-509.

Klauss, A., Sikora, T., Suss, B., & Dau, H. (2012). Fast structural changes (200-900ns) may prepare the photosynthetic manganese complex for oxidation by the adjacent tyrosine radical. *Biochim Biophys Acta, 1817*, 1196-1207.

Koike, H., Hanssum, B., Inoue, Y., & Renger, G. (1987). Temperature dependence of S-state transition in a thermophilic cyanobacterium, *Synechococcus vulcanus* Copeland measured by absorption changes in the ultraviolet region. *Biochimica et Biophysica Acta, 893*, 524-533.

Kok, B., Forbush, B., & McGloin, M. (1970). Cooperation of charges in photosynthetic $O_2$ evolution - I. A linear four-step mechanism. *Photochemistry and Photobiology, 11*, 457-475.

Koulougliotis, D., Hirsh, D. J., & Brudvig, G. W. (1992). The $O_2$-evolving center of photosystem II is diamagnetic in the $S_1$ resting state. *Journal of the American Chemical Society, 114*(21), 8322-8323.

Krewald, V., Retegan, M., Neese, F., Lubitz, W., Pantazis, D. A., & Cox, N. (2016). Spin State as a Marker for the Structural Evolution of Nature's Water-Splitting Catalyst. *Inorg Chem, 55*(2), 488-501.

Krivanek, R., Dau, H., & Haumann, M. (2008). Enthalpy changes during photosynthetic water oxidation tracked by time-resolved calorimetry using a photothermal beam deflection technique. *Biophysical Journal, 94*(5), 1890-1903.

Lafont, V., Armstrong, A. A., Ohtaka, H., Kiso, Y., Amzel, L. M., & Freire, E. (2007). Compensating enthalpic and entropic changes hinder binding affinity optimization. *Chemical Biology & Drug Design, 69*(6), 413-422.

Lavorel, J. (1976). Matrix Analysis of Oxygen Evolving System of Photosynthesis. *Journal of Theoretical Biology, 57*(1), 171-185.

Lavorel, J. (1992). Determination of the Photosynthetic Oxygen Release Time by Amperometry. *Biochimica et Biophysica Acta, 1101*(1), 33-40.

Lazar, D. (1999). Chlorophyll a fluorescence induction. *Biochimica et Biophysica Acta, 1412*, 1-28.

Lichtenthaler, H. K. (1987). Chlorophylls and Carotenoids - Pigments of Photosynthetic Biomembranes. *Methods in Enzymology, 148*, 350-382.

Losi, A., Wegener, A. A., Engelhard, M., & Braslavsky, S. E. (2001). Enthalpy−Entropy Compensation in a Photocycle: The K-to-L Transition in Sensory Rhodopsin II from Natronobacterium pharaonis. *Journal of the American Chemical Society, 123*(8), 1766-1767.

Marcus, R. A. (1993). Electron transfer reactions in chemistry. Theory and experiment. *Reviews of Modern Physics, 65*(3), 599-610.

Mario Pagliaro, M. R. ( 2010). The Future of Glycerol: Edition 2 (pp. 3).

Messinger, J., Schroder, W. P., & Renger, G. (1993). Structure-function relations in photosystem II. Effects of temperature and chaotropic agents on the period four oscillation of flash-induced oxygen evolution. *Biochemistry, 32*(30), 7658-7668.

Mullineaux, C. W. (2014). Co-existence of photosynthetic and respiratory activities in cyanobacterial thylakoid membranes. *Biochimica Et Biophysica Acta-Bioenergetics, 1837*(4), 503-511.

Navarro, M. P., Ames, W. M., Nilsson, H., Lohmiller, T., Pantazis, D. A., Rapatskiy, L., . . . Cox, N. (2013). Ammonia binding to the oxygen-evolving complex of photosystem II identifies the solvent-exchangeable oxygen bridge (mu-oxo) of the manganese tetramer. *Proceedings of the National Academy of Sciences of the United States of America, 110*(39), 15561-15566.

Nield, J., Kruse, O., Ruprecht, J., da Fonseca, P., Buchel, C., & Barber, J. (2000). Three-dimensional structure of Chlamydomonas reinhardtii and Synechococcus elongatus photosystem II complexes allows for comparison of their oxygen-evolving complex organization. *Journal of Biological Chemistry, 275*(36), 27940-27946.

Noring, B., Shevela, D., Renger, G., & Messinger, J. (2008a). Effects of methanol on the S-i-state transitions in photosynthetic water-splitting. *Photosynthesis Research, 98*(1-3), 251-260.

Noring, B., Shevela, D., Renger, G., & Messinger, J. (2008b). Effects of methanol on the Si-state transitions in photosynthetic water-splitting. *Photosynthesis Research, 98*(1-3), 251-260.

Oyala, P. H., Stich, T. A., Debus, R. J., & Britt, R. D. (2015). Ammonia Binds to the Dangler Manganese of the Photosystem II Oxygen-Evolving Complex. *Journal of the American Chemical Society, 137*(27), 8829-8837.

Pal, R., Negre, C. F. A., Vogt, L., Pokhrel, R., Ertem, M. Z., Brudvig, G. W., & Batista, V. S. (2013). S-0-State Model of the Oxygen-Evolving Complex of Photosystem II. *Biochemistry, 52*(44), 7703-7706.

Pantazis, D. A., Ames, W., Cox, N., Lubitz, W., & Neese, F. (2012). Two interconvertible structures that explain the spectroscopic properties of the oxygen-evolving complex of photosystem II in the S2 state. *Angewandte Chemie, International Edition, 51*(39), 9935-9940.

Papageorgiou, G. C., & Govindjee. (2011). Photosystem II fluorescence: Slow changes – Scaling from the past. *Journal of Photochemistry and Photobiology B: Biology, 104*(1–2), 258-270.

Parsegian, V. A. (2002). Protein-water interactions. *International Review of Cytology - a Survey of Cell Biology, Vol 215, 215*, 1-31.

Pham, L. V., & Messinger, J. (2016). Probing S-state advancements and recombination pathways in photosystem II with a global fit program for flash-induced oxygen evolution pattern. *Biochimica Et Biophysica Acta-Bioenergetics, 1857*(6), 848-859.

Pokhrel, R., & Brudvig, G. W. (2014). Oxygen-evolving complex of photosystem II: correlating structure with spectroscopy. *Phys Chem Chem Phys, 16*(24), 11812-11821.

Polander, B. C., & Barry, B. A. (2012). A hydrogen-bonding network plays a catalytic role in photosynthetic oxygen evolution. *Proceedings of the National Academy of Sciences, 109*(16), 6112-6117.

Qian, H. (1998). Entropy-enthalpy compensation: Conformational fluctuation and induced-fit. *Journal of Chemical Physics, 109*(22), 10015-10017.

Rappaport, F., Ishida, N., Sugiura, M., & Boussac, A. (2011). Ca2+ determines the entropy changes associated with the formation of transition states during water oxidation by Photosystem II. *Energy & Environmental Science, 4*(7), 2520-2524.

Renger, G., & Hanssum, B. (1992). Studies on the reaction coordinates of the water oxidase in PS II membrane fragments from spinach. *Febs Letters, 299*(1), 28-32.

Renger, G., & Hanssum, B. (2009). Oxygen detection in biological systems. *Photosynthesis Research*.

Retegan, M., Krewald, V., Mamedov, F., Neese, F., Lubitz, W., Cox, N., & Pantazis, D. A. (2016). A five-coordinate Mn(IV) intermediate in biological water oxidation: spectroscopic signature and a pivot mechanism for water binding. *Chemical Science, 7*(1), 72-84.

Rippka, R. (1988). Isolation and purification of cyanobacteria. *Methods Enzymol, 167*, 3-27.

Roelofs, T. A., Lee, C. H., & Holzwarth, A. R. (1992). Global Target Analysis of Picosecond Chlorophyll Fluorescence Kinetics From Pea-chloroplasts - A New Approach To the Characterization of the Primary Processes In Photosystem-ii Alpha-units and Beta-units. *Biophysical Journal, 61*(5), 1147-1163.

Rutherford, A. W., Govindjee, & Inoue, Y. (1984). Charge accumulation and photochemistry in leaves studied by thermoluminescence and delayed light emission. *Proceedings of the National Academy of Sciences of the United States of America, 81*(Botany), 1107-1111.

Sachs, R. K., Halverson, K. M., & Barry, B. A. (2003). Specific isotopic labeling and photooxidation-linked structural changes in the manganese-stabilizing subunit of photosystem II. *J Biol Chem, 278*(45), 44222-44229.

Sander, J., Nowaczyk, M., Buchta, J., Dau, H., Vass, I., Deák, Z., . . . Rögner, M. (2010). Functional Characterization and Quantification of the Alternative PsbA Copies in Thermosynechococcus elongatus and Their Role in Photoprotection. *J Biol Chem, 285*(39), 29851-29856.

Schiller, H., & Dau, H. (2000). Preparation protocols for high-activity photosystem II membrane particles of green algae and higher plants, pH dependence of oxygen evolution and comparison of the S2-state multiline signal by X-band EPR spectroscopy. *J Photochem Photobiol B, 55*(2-3), 138-144.

Schraut, J., & Kaupp, M. (2014). On Ammonia Binding to the Oxygen-Evolving Complex of Photosystem II: A Quantum Chemical Study. *Chemistry-a European Journal, 20*(24), 7300-7308.

Schuth, N., Liang, Z., Schonborn, M., Kussicke, A., Assuncao, R., Zaharieva, I., . . . Dau, H. (2017). Inhibitory and Non-Inhibitory NH3 Binding at the Water-Oxidizing Manganese Complex of Photosystem II Suggests Possible Sites and a Rearrangement Mode of Substrate Water Molecules. *Biochemistry, 56*(47), 6240-6256.

Shen, J. R. (2015). The Structure of Photosystem II and the Mechanism of Water Oxidation in Photosynthesis. *Annual Review of Plant Biology, Vol 66, 66*, 23-48.

Shinkarev, V. P., & Govindjee. (1993). Insight into the relationship of chlorophyll a fluorescence yield to the concentration of its natural quenchers in oxygenic photosynthesis. *Proceedings of the National Academy of Sciences of the United States of America, 90*(16), 7466-7469.

Shinkarev, V. P., Xu, C., Govindjee, & Wraight, C. A. (1997). Kinetics of the oxygen evolution step in plants determined from flash-induced chlorophyll a fluorescence. *Photosynthesis Research, 51*(1), 43-49.

Shoji, M., Isobe, H., & Yamaguchi, K. (2015). QM/MM study of the S-2 to S-3 transition reaction in the oxygen-evolving complex of photosystem II. *Chemical Physics Letters, 636*, 172-179.

Shoji, M., Isobe, H., Yamanaka, S., Umena, Y., Kawakami, K., Kamiya, N., . . . Yamaguchi, K. (2015). Large-Scale QM/MM Calculations of Hydrogen Bonding Networks for Proton Transfer and Water Inlet Channels for Water Oxidation-Theoretical System Models of the Oxygen-Evolving Complex of Photosystem II. *Advances in Quantum Chemistry, Vol 70, 70*, 325-413.

Siddiqui, K. S., & Cavicchioli, R. (2006). Cold-adapted enzymes. *Annual Review of Biochemistry, 75*, 403-433.

Siegbahn, P. E. M. (2013). Water oxidation mechanism in photosystem II, including oxidations, proton release pathways, O—O bond formation and $O_2$ release. *Biochimica et Biophysica Acta (BBA) - Bioenergetics, 1827*(8–9), 1003-1019.

Siegbahn, P. E. M. (2017). Nucleophilic water attack is not a possible mechanism for O-O bond formation in photosystem II. *Proceedings of the National Academy of Sciences of the United States of America, 114*(19), 4966-4968.

Smith, J. D., Cappa, C. D., Wilson, K. R., Messer, B. M., Cohen, R. C., & Saykally, R. J. (2004). Energetics of hydrogen bond network rearrangements in liquid water. *Science, 306*(5697), 851-853.

Somepics. (2018). Light-dependent reactions of photosynthesis in the thylakoid membrane of plant cells. Thylakoid membrane 3.svg. Retrieved from https://commons.wikimedia.org/w/index.php?curid=38088695

Stevens, S. E., & Porter, R. D. (1980). Transformation in Agmenellum quadruplicatum. *Proceedings of the National Academy of Sciences of the United States of America, 77*(10), 6052-6056.

Strehler, B. L., & Arnold, W. (1951). Light production by green plants. *The Journal of General Physiology, 34*(6), 809-820.

Styring, S., & Rutherford, A. W. (1987). In the oxygen-evolving complex of Photosystem II the $S_0$ state is oxidized to the $S_1$ state by $D^+$ (signal II slow). *Biochemistry, 26*(9), 2401-2405.

Su, J. H., Cox, N., Ames, W., Pantazis, D. A., Rapatskiy, L., Lohmiller, T., . . . Messinger, J. (2011). The electronic structures of the S-2 states of the oxygen-evolving complexes of photosystem II in plants and cyanobacteria in the presence and absence of methanol. *Biochimica Et Biophysica Acta-Bioenergetics, 1807*(7), 829-840.

Suga, M., Akita, F., Sugahara, M., Kubo, M., Nakajima, Y., Nakane, T., . . . Shen, J. R. (2017). Light-induced structural changes and the site of O=O bond formation in PSII caught by XFEL. *Nature, 543*(7643), 131-135.

Suresh, S. J., & Naik, V. M. (2000). Hydrogen bond thermodynamic properties of water from dielectric constant data. *Journal of Chemical Physics, 113*(21), 9727-9732.

Tamura, N., Inoue, Y., & Cheniae, G. M. (1989). Photoactivation of the Water-Oxidizing Complex in Photosystem-Ii Membranes Depleted of Mn, Ca and Extrinsic Proteins .2. Studies on the Functions of Ca-2+. *Biochimica et Biophysica Acta, 976*(2-3), 173-181.

Thapper, A., Mamedov, F., Mokvist, F., Hammarstrom, L., & Styring, S. (2009). Defining the Far-Red Limit of Photosystem II in Spinach. *Plant Cell, 21*(8), 2391-2401.

Tsamaloukas, A. D. (2001). Fluoreszenzspektroskopie zur Excitonendynamik in den Chlorophyll-Antennen des Photosystems II der Pflanzen. *Diploma thesis, FB Physik, FU Berlin*.

Tsuno, M., Suzuki, H., Kondo, T., Mino, H., & Noguchi, T. (2011). Interaction and inhibitory effect of ammonium cation in the oxygen evolving center of photosystem II. *Biochemistry, 50*(13), 2506-2514.

Turzó, K., Laczkó, G., Filus, Z., & Maróti, P. (2000). Quinone-dependent delayed fluorescence from the reaction center of photosynthethic bacteria. *Biophysical Journal, 79*, 14-25.

Tzeng, S. R., & Kalodimos, C. G. (2012). Protein activity regulation by conformational entropy. *Nature, 488*(7410), 236-240.

Umena, Y., Kawakami, K., Shen, J.-R., & Kamiya, N. (2011). Crystal structure of oxygen-evolving photosystem II at a resolution of 1.9 Å. *Nature, 473*, 55-60.

Vagenende, V., Yap, M. G. S., & Trout, B. L. (2009a). Mechanisms of Protein Stabilization and Prevention of Protein Aggregation by Glycerol. *Biochemistry, 48*(46), 11084-11096.

Vagenende, V., Yap, M. G. S., & Trout, B. L. (2009b). Molecular Anatomy of Preferential Interaction Coefficients by Elucidating Protein Solvation in Mixed Solvents: Methodology and Application for Lysozyme in Aqueous Glycerol. *Journal of Physical Chemistry B, 113*(34), 11743-11753.

Van Gorkom, H. J., Pulles, M. P., Haveman, J., & Den Haan, G. A. (1976). Primary reactions of photosystem II at low pH. I. Prompt and delayed fluorescence. *Biochimica et Biophysica Acta, 423*(2), 217-226.

Velthuys, B. R. (1975). Binding of Inhibitor Nh3 to Oxygen-Evolving Apparatus of Spinach-Chloroplasts. *Biochimica et Biophysica Acta, 396*(3), 392-401.

Venediktov, P. S., Goltsev, V. N., & Shinkarev, V. P. (1980). The influence of the electric diffusion potential on delayed fluorescence light curves of chloroplasts treated with 3-(3,4-dichlorophenyl)-1,1-dimethylurea. *Biochimica et Biophysica Acta, 593*(1), 125-132.

Vinyard, D. J., Askerka, M., Debus, R. J., Batista, V. S., & Brudvig, G. W. (2016). Ammonia Binding in the Second Coordination Sphere of the Oxygen-Evolving Complex of Photosystem II. *Biochemistry, 55*(31), 4432-4436.

Vinyard, D. J., & Brudvig, G. W. (2015). Insights into substrate binding to the oxygen-evolving complex of photosystem II from ammonia inhibition studies. *Biochemistry, 54*(2), 622-628.

Vinyard, D. J., & Brudvig, G. W. (2017). Progress Toward a Molecular Mechanism of Water Oxidation in Photosystem II. *Annual Review of Physical Chemistry, Vol 68, 68*, 101-116.

Vinyard, D. J., Khan, S., & Brudvig, G. W. (2015). Photosynthetic water oxidation: binding and activation of substrate waters for O-O bond formation. *Faraday Discussions, 185*, 37-50.

Wraight, C. A. (2006). Chance and design--proton transfer in water, channels and bioenergetic proteins. *Biochim Biophys Acta, 1757*(8), 886-912.

Young, I. D., Ibrahim, M., Chatterjee, R., Gul, S., Fuller, F. D., Koroidov, S., . . . Yano, J. (2016). Structure of photosystem II and substrate binding at room temperature. *Nature, 540*(7633), 453-457.

Zaharieva, I., Grabolle, M., Chernev, P., & Dau, H. (2013). Water oxidation in photosystem II: Energetics and kinetics of intermediates formation in $S_2$->$S_3$ and $S_3$->$S_0$ transitions monitored by delayed chlorophyll fluorescence. In T. Kuang, C. Lu, & L. Zhang (Eds.), *Photosynthesis Research for Food, Fuel and Future* (pp. 234-238). Heidelberg: Springer.

Zimmermann, J. L., & Rutherford, A. W. (1986). Photoreductant-induced oxidation of Fe2+ in the electron-acceptor complex of Photosystem II. *Biochimica et Biophysica Acta (BBA) - Bioenergetics, 851*(3), 416-423.

Zoski, C. G. (2007). *Handbook of Electrochemistry*. Oxford, UK: Elsevier's Science & Technology Rights Department.

Zouni, A., Witt, H. T., Kern, J., Fromme, P., Krauss, N., Saenger, W., & Orth, P. (2001). Crystal structure of photosystem II from *Synechococcus elongatus* at 3.8 Å resolution. *Nature, 409*(6821), 739-743.

# Appendix

# Appendix A Buffer Compositions

## A.1 Buffer Used in Protein Purification

### A.1.1 Buffer A

| Chemicals / pH | [mM] |
|---|---|
| Sucrose | 400 |
| HEPES | 25 |
| NaCl | 15 |
| $MgCl_2$ | 5 |
| $CaCl_2$ | 5 |
| BSA * | 2 g/l |
| Na-ascorbate * | 5 |
| pH | 7.5 |

*Added one hour before used.

### A.1.2 Buffer B

| Chemicals / pH | [mM] |
|---|---|
| MES | 25 |
| NaCl | 150 |
| $MgCl_2$ | 5 |
| pH | 6.2 |

### A.1.3 Buffer C

| Chemicals / pH | [mM] |
|---|---|
| Betaine * | 1,000 |
| MES | 25 |
| NaCl | 15 |
| $MgCl_2$ | 10 |
| $CaCl_2$ | 5 |
| pH | 6.2 |

* For triton incubation without Betaine.

### A.1.4 Buffer D *

| Chemicals / pH | [mM] |
|---|---|
| Betaine | 1,000 |
| MES | 25 |
| NaCl | 15 |
| $MgCl_2$ | 5 |
| $CaCl_2$ | 5 |
| pH | 6.2 |

* Also used in measurement.

### A.1.5 Buffer MCMB

| Chemicals / pH | [mM] |
|---|---|
| Betaine | 500 |
| MES | 20 |
| $MgCl_2$ | 10 |

| | |
|---|---|
| $CaCl_2$ | 20 |
| pH | 6.0 |

### A.1.6 Buffer TSB

| Chemicals / pH | [mM] |
|---|---|
| Betaine | 1,200 |
| MES-NaOH | 50 |
| glycerol | 10% [v/v] |
| $MgCl_2$ | 5 |
| $CaCl_2$ | 5 |
| pH | 6.2 |

## A.2 Buffer Used in PSII Treatment Assays

### A.2.1 Glycerol Buffer

| Chemicals / pH | [mM] |
|---|---|
| Betaine | 1,000 |
| MES | 25 |
| NaCl | 15 |
| $MgCl_2$ | 5 |
| $CaCl_2$ | 5 |
| Glycerol | 67% [v/v] |
| pH | 6.2 |

### A.2.2 Buffer NaCl

| Chemicals / pH | [mM] |
|---|---|
| Betaine | 1,000 |
| MES | 25 |
| HEPES | 25 |
| HEPPS | 25 |
| NaCl | 150 |
| $MgCl_2$ | 5 |
| $CaCl_2$ | 5 |
| pH | 7.5 |

### A.2.3 Buffer Ammonia

| Chemicals / pH | [mM] |
|---|---|
| Betaine | 1,000 |
| MES | 25 |
| HEPES | 25 |
| HEPPS | 25 |
| $NH_4Cl$ | 150 |
| $MgCl_2$ | 5 |
| $CaCl_2$ | 5 |
| pH | 7.5 |

### A.2.4 Buffer Ternary

| Chemicals / pH | [mM] |
|---|---|
| Betaine | 1,000 |

| | |
|---|---|
| MES | 25 |
| HEPES | 25 |
| HEPPS | 25 |
| NaCl | 150 |
| $MgCl_2$ | 5 |
| $CaCl_2$ | 5 |
| pH | 6.2 |

# Appendix B Influence of the Time Period between Flashes on the Oxygen Evolution Transients

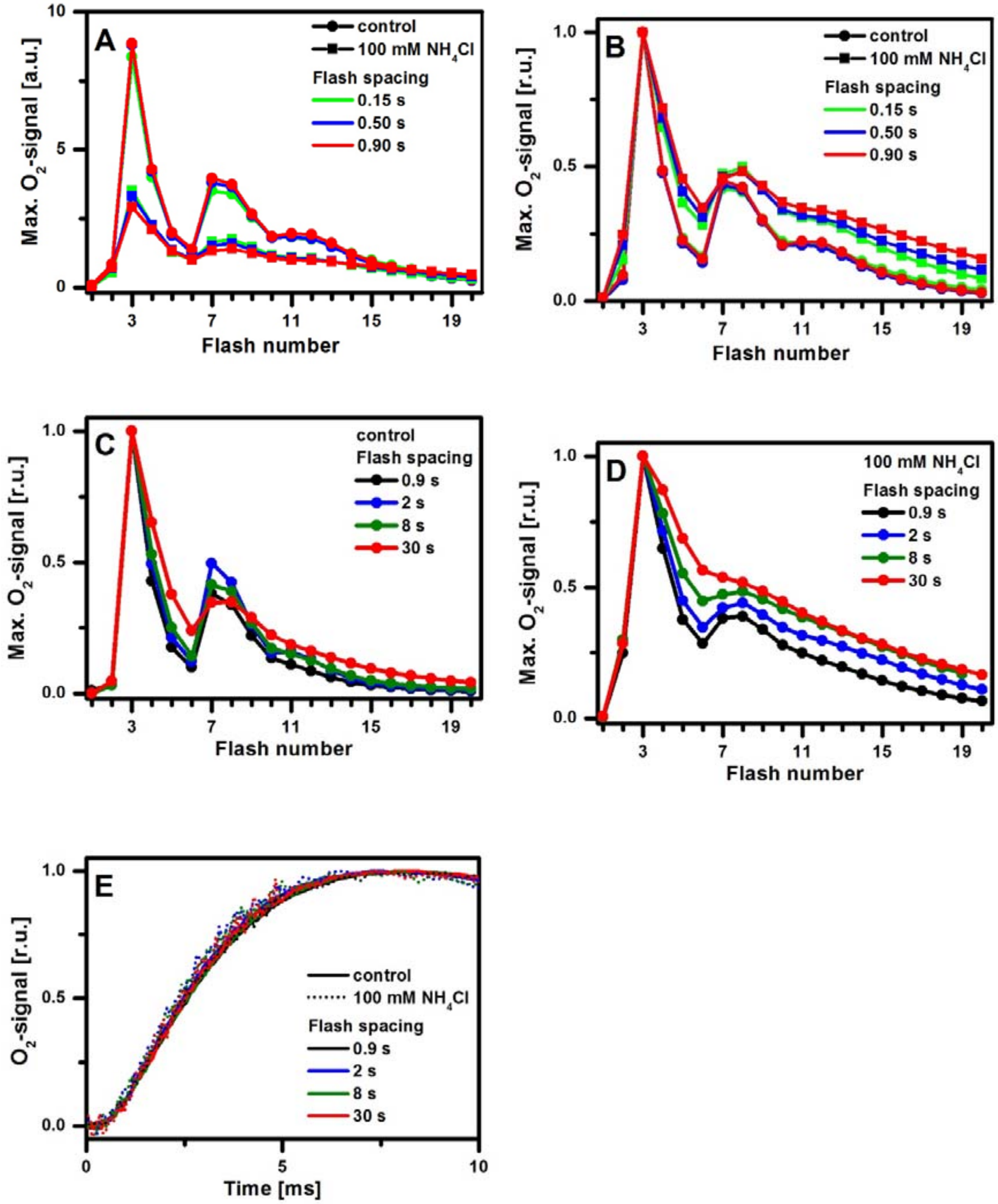

**Figure 0.1. Influence of the time period between flashes on the oxygen evolution transients (plant PSII membrane particles, pH 7.5). The flash spacing for all flashes was varied between 0.15 s and 30 s. In A, B, C, and D, flash-number dependencies (flash patterns) of the peak amplitudes of $O_2$-transients are shown for the various indicated time intervals between laser flashes. In B, C, and D, the flash patterns are normalized to the respective 3rd-flash**

**amplitude. (E) Normalized 3rd-flash $O_2$-signal showing that the rise time (time constant of $O_2$-formation) is unaffected by variation of the flash spacing.**

# Appendix C Prompt Chlorophyll Fluorescence Data

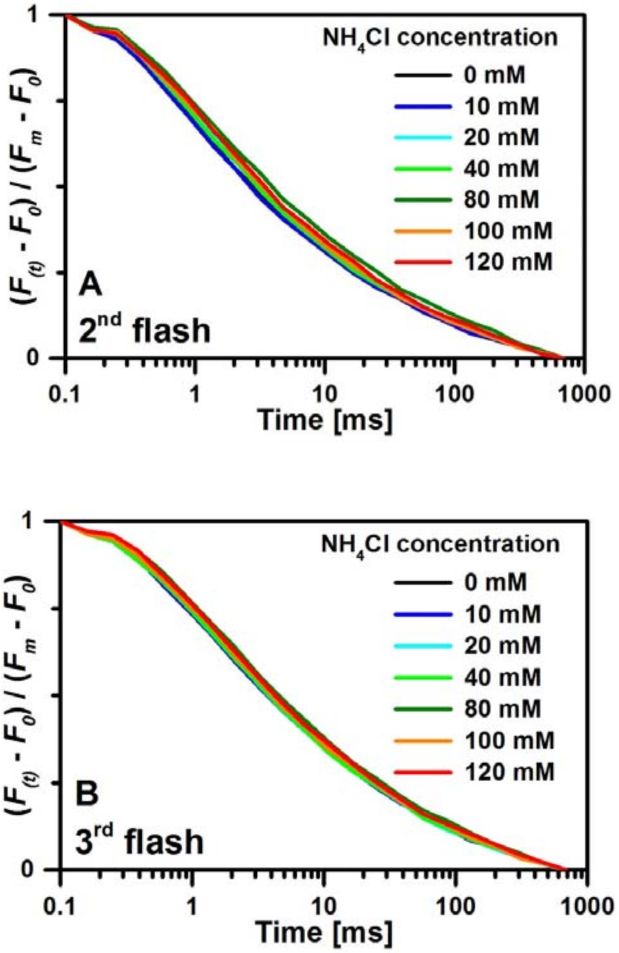

**Figure 0.2. The normalized prompt chlorophyll fluorescence at acceptor side reactions of PSII membrane particles from spinach after the 2nd (in A) and 3rd (in B) flash (at pH 7.5). The changes in the multi-exponential decay are small suggesting that the $Q_A^-$ re-oxidation kinetics are not significantly affected by $NH_4Cl$ addition (see also Figure 3.5 for the 1st flash data). The changes on the 2nd and 3rd flash are comparably small, but still larger than those on the 1st flash, possibly resulting from modified recombination properties in the ammonium-modified $S_2$ and $S_3$ state.**

# Appendix D Fit Parameters of Delayed Fluorescence Transients

**Table 0-1. Fit parameters of amplitudes ($A_1$, $A_2$, $A_3$ and C), time constants ($\tau_1$, $\tau_2$ and $\tau_3$) and fit errors ($\varepsilon^2$), resulting from a sum of three exponential functions to the decays in Figure 4.4. The parameters are averaged from six repeated measurements.**

| glycerol | $A_1$ | $A_2$ | $A_3$ | $\tau_1$ | $\tau_2$ | $\tau_3$ | C | $\varepsilon^2$ |
|---|---|---|---|---|---|---|---|---|
| 0 % | 1.09 | 0.33 | 0.02 | 0.02 | 0.10 | 1.73 | 0.0008 | 0.03 |
| 5 % | 1.06 | 0.28 | 0.03 | 0.03 | 0.13 | 1.71 | 0.0008 | 0.04 |
| 10 % | 1.15 | 0.29 | 0.03 | 0.03 | 0.14 | 1.69 | 0.0007 | 0.04 |
| 15 % | 1.26 | 0.31 | 0.03 | 0.03 | 0.16 | 1.63 | 0.0008 | 0.05 |
| 20 % | 1.26 | 0.29 | 0.03 | 0.03 | 0.18 | 1.67 | 0.0007 | 0.05 |
| 25 % | 1.30 | 0.32 | 0.03 | 0.03 | 0.21 | 1.68 | 0.0007 | 0.05 |
| 30 % | 1.33 | 0.35 | 0.03 | 0.03 | 0.22 | 1.72 | 0.0008 | 0.04 |
| 35 % | 1.38 | 0.39 | 0.03 | 0.03 | 0.24 | 1.90 | 0.0006 | 0.05 |
| 40 % | 1.43 | 0.41 | 0.03 | 0.03 | 0.25 | 1.96 | 0.0005 | 0.04 |
| 45 % | 1.52 | 0.46 | 0.03 | 0.03 | 0.25 | 2.05 | 0.0007 | 0.04 |
| 50 % | 1.35 | 0.40 | 0.02 | 0.03 | 0.26 | 2.16 | 0.0007 | 0.04 |

**Table 0-2. Fit parameters of the flash pattern in Figure 4.6, in which $S_0$ [%] and $S_1$ [%] are the population distribution (in terms of percentage) in the dark-adapted state of PSII.**

| glycerol | Miss | Std. dev. | Std. err. | Efficiency | $S_0$ [%] | $S_1$ [%] |
|---|---|---|---|---|---|---|
| 0 % | 9.36 | 0.89 | 0.36 | 90.64 | 0.73 | 99.27 |
| 5 % | 9.04 | 0.53 | 0.21 | 90.96 | 7.90 | 92.10 |
| 10 % | 9.43 | 0.59 | 0.24 | 90.57 | 2.68 | 97.32 |
| 15 % | 9.83 | 0.59 | 0.24 | 90.17 | 1.62 | 98.38 |
| 20 % | 9.66 | 0.67 | 0.27 | 90.34 | 0.00 | 100.00 |
| 25 % | 10.05 | 0.58 | 0.24 | 89.95 | 0.18 | 99.82 |
| 30 % | 10.49 | 0.45 | 0.19 | 89.51 | 1.84 | 98.16 |
| 35 % | 12.04 | 0.90 | 0.37 | 87.96 | 1.97 | 98.03 |
| 40 % | 12.94 | 0.88 | 0.36 | 87.06 | 0.63 | 99.37 |
| 45 % | 13.58 | 1.10 | 0.45 | 86.42 | 0.93 | 99.07 |
| 50 % | 14.47 | 1.37 | 0.56 | 85.53 | 1.80 | 98.20 |

**Table 0-3. Fit parameters of amplitudes ($A_1$, $A_2$, $A_3$ and C), time constants ($\tau_1$, $\tau_2$ and $\tau_3$) and fit errors ($\varepsilon^2$), resulting from a sum of three exponential functions to the decays in Figure 4.8. The parameters are averaged from six repeated measurements.**

| glycerol | $A_1$ | $A_2$ | $A_3$ | $\tau_1$ | $\tau_2$ | $\tau_3$ | C | $\varepsilon^2$ |
|---|---|---|---|---|---|---|---|---|
| 0 % | 0.74 | 0.14 | 0.02 | 0.02 | 0.08 | 0.31 | 0.0009 | 0.02 |
| 5 % | 0.78 | 0.16 | 0.02 | 0.02 | 0.08 | 0.35 | 0.0008 | 0.02 |
| 10 % | 0.81 | 0.16 | 0.03 | 0.02 | 0.09 | 0.37 | 0.0009 | 0.02 |
| 15 % | 0.88 | 0.17 | 0.04 | 0.02 | 0.09 | 0.37 | 0.0012 | 0.01 |
| 20 % | 0.87 | 0.18 | 0.05 | 0.02 | 0.09 | 0.37 | 0.0010 | 0.01 |
| 25 % | 0.92 | 0.20 | 0.07 | 0.02 | 0.10 | 0.39 | 0.0011 | 0.01 |
| 30 % | 0.91 | 0.22 | 0.09 | 0.02 | 0.11 | 0.41 | 0.0013 | 0.01 |
| 35 % | 1.04 | 0.26 | 0.12 | 0.02 | 0.10 | 0.40 | 0.0017 | 0.00 |
| 40 % | 1.11 | 0.27 | 0.14 | 0.02 | 0.10 | 0.42 | 0.0017 | 0.00 |
| 45 % | 1.13 | 0.31 | 0.16 | 0.02 | 0.11 | 0.42 | 0.0022 | 0.00 |
| 50 % | 0.96 | 0.29 | 0.15 | 0.02 | 0.11 | 0.44 | 0.0025 | 0.00 |

**Table 0-4. Fit parameters of amplitudes ($A_1$, $A_2$, $A_3$ and C), time constants ($\tau_1$, $\tau_2$ and $\tau_3$) and fit errors ($\varepsilon^2$), resulting from a sum of three exponential functions to the decays in Figure 4.14A (0% glycerol).**

| T [°C] | $A_1$ | $\tau_1$ | $A_2$ | $\tau_2$ | $A_3$ | $\tau_3$ | Std. err. | C | $\varepsilon^2$ |
|---|---|---|---|---|---|---|---|---|---|
| 0.0 | 0.13 | 0.03 | 0.04 | 0.25 | 0.00 | 3.41 | 0.46 | 0.0001 | 0.05 |
| 2.5 | 1.07 | 0.02 | 0.17 | 0.19 | 0.01 | 2.92 | 0.24 | 0.0008 | 0.04 |
| 5.0 | 0.95 | 0.02 | 0.18 | 0.18 | 0.01 | 2.72 | 0.06 | 0.0005 | 0.04 |
| 7.5 | 0.53 | 0.02 | 0.16 | 0.16 | 0.01 | 2.60 | 0.13 | 0.0003 | 0.03 |
| 10.0 | 0.98 | 0.02 | 0.22 | 0.16 | 0.02 | 2.46 | 0.10 | 0.0005 | 0.03 |
| 12.5 | 0.56 | 0.03 | 0.17 | 0.15 | 0.01 | 2.01 | 0.08 | 0.0006 | 0.03 |
| 15.0 | 1.06 | 0.02 | 0.26 | 0.14 | 0.02 | 1.97 | 0.06 | 0.0007 | 0.03 |
| 17.5 | 0.84 | 0.02 | 0.24 | 0.12 | 0.02 | 1.75 | 0.08 | 0.0012 | 0.03 |
| 20.0 | 1.07 | 0.02 | 0.27 | 0.13 | 0.02 | 1.70 | 0.05 | 0.0009 | 0.03 |
| 22.5 | 0.90 | 0.03 | 0.23 | 0.11 | 0.02 | 1.47 | 0.03 | 0.0015 | 0.02 |
| 25.0 | 1.06 | 0.02 | 0.29 | 0.11 | 0.03 | 1.45 | 0.03 | 0.0012 | 0.03 |
| 27.5 | 0.99 | 0.02 | 0.26 | 0.10 | 0.03 | 1.35 | 0.04 | 0.0020 | 0.02 |
| 30.0 | 1.16 | 0.02 | 0.29 | 0.10 | 0.03 | 1.31 | 0.02 | 0.0016 | 0.03 |

**Table 0-5. Fit parameters of amplitudes ($A_1$, $A_2$, $A_3$ and C), time constants ($\tau_1$, $\tau_2$ and $\tau_3$) and fit errors ($\varepsilon^2$), resulting from a sum of three exponential functions to the decays in Figure 4.14B (30% glycerol).**

| T [°C] | $A_1$ | $\tau_1$ | $A_2$ | $\tau_2$ | $A_3$ | $\tau_3$ | Std. err. | C | $\varepsilon^2$ |
|---|---|---|---|---|---|---|---|---|---|
| 0.0 | 0.18 | 0.03 | 0.05 | 0.26 | 0.01 | 2.79 | 0.36 | 0.0001 | 0.04 |
| 2.5 | 1.23 | 0.02 | 0.18 | 0.22 | 0.02 | 2.42 | 0.14 | 0.0007 | 0.04 |
| 5.0 | 1.12 | 0.02 | 0.19 | 0.21 | 0.02 | 2.32 | 0.09 | 0.0005 | 0.05 |
| 7.5 | 0.79 | 0.02 | 0.18 | 0.19 | 0.02 | 2.15 | 0.10 | 0.0004 | 0.04 |
| 10.0 | 1.24 | 0.03 | 0.23 | 0.22 | 0.03 | 1.97 | 0.09 | 0.0005 | 0.05 |
| 12.5 | 0.88 | 0.03 | 0.20 | 0.21 | 0.02 | 1.87 | 0.09 | 0.0005 | 0.05 |
| 15.0 | 1.26 | 0.03 | 0.24 | 0.26 | 0.03 | 1.67 | 0.05 | 0.0003 | 0.07 |
| 17.5 | 1.27 | 0.03 | 0.27 | 0.23 | 0.04 | 1.57 | 0.08 | 0.0010 | 0.05 |
| 20.0 | 1.43 | 0.03 | 0.31 | 0.33 | 0.06 | 1.60 | 0.06 | 0.0011 | 0.05 |
| 22.5 | 1.33 | 0.03 | 0.30 | 0.24 | 0.03 | 1.47 | 0.11 | 0.0012 | 0.04 |
| 25.0 | 1.60 | 0.03 | 0.43 | 0.23 | 0.04 | 1.50 | 0.05 | 0.0015 | 0.03 |
| 27.5 | 1.41 | 0.04 | 0.36 | 0.23 | 0.03 | 1.39 | 0.05 | 0.0018 | 0.03 |
| 30.0 | 1.85 | 0.04 | 0.47 | 0.20 | 0.04 | 1.47 | 0.05 | 0.0018 | 0.03 |

**Equation 0.1. Standard equation for non-cooperative ligand binding based on the Michaelis-Menten equation. $A_{\min}$ is the minimum reaction rate when the substrate concentration is zero, $A_{\min}$ is the saturation maximum in Michalis-Menten kinetics, $c$ is the substrate concentration, and $K_M$ is the substrate concentration, at which the reaction rate is half of the maximum.**

$$A(c) = A_{\min} + (A_{\max} - A_{\min})\frac{c}{c + K_M} \quad .$$

# Appendix E Fitted Transients and Parameters of the Oxygen Diffusion Model

## E.1 *Synechococcus* sp. PCC 7002

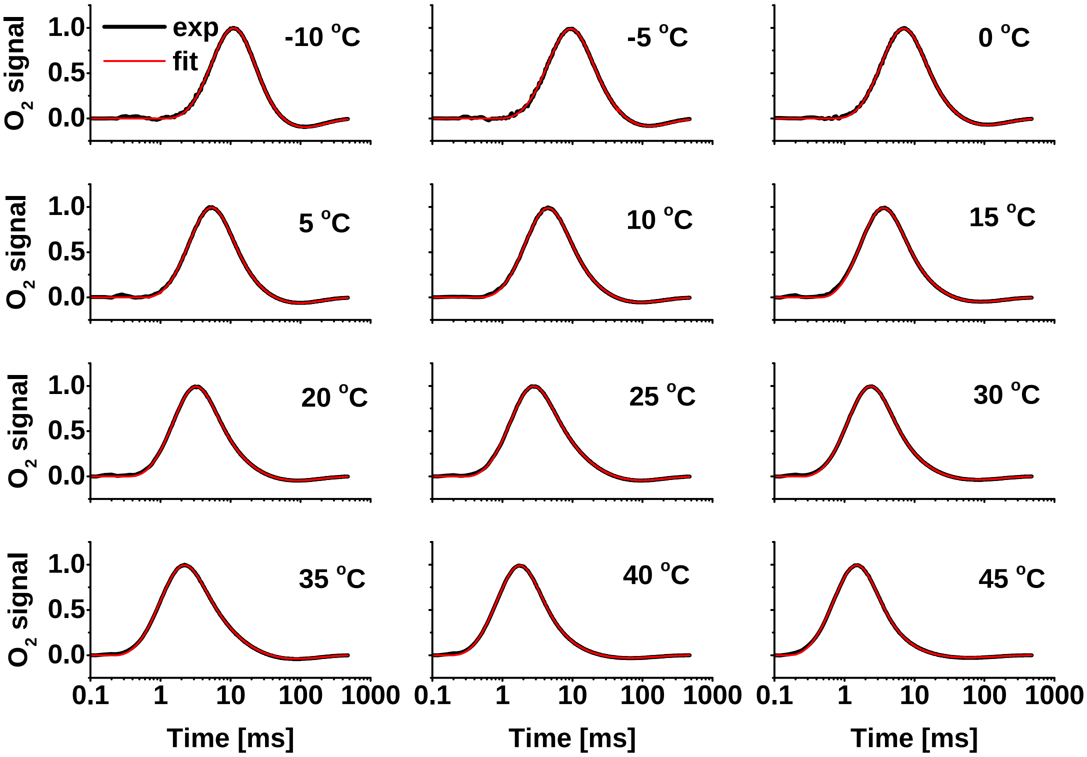

**Figure 0.3. Transients of the individual oxygen signal of *Synechococcus* sp. PCC 7002 from Figure 5.3, fitted by oxygen diffusion model (experimental data in black and fit in red), from -10 ºC to 45 ºC in an increment of 5 ºC (from upper left to lower right orientation).**

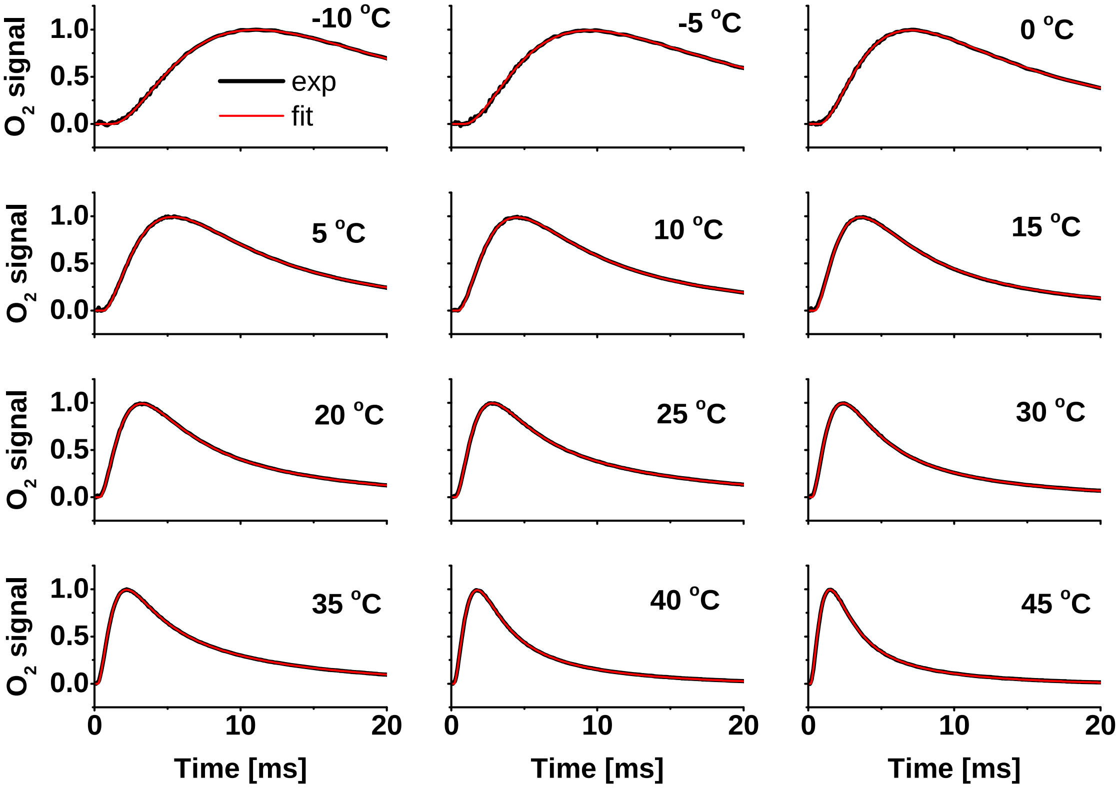

**Figure 0.4. Transients of the individual oxygen signal of *Synechococcus* sp. PCC 7002 from Figure 5.3, fitted by oxygen diffusion model (experimental data in black and fit in red), from -10 ºC to 45 ºC (from upper left to lower right orientation). They are presented in linear scale from 0 to 20 ms, highlighting the rising time of the transients.**

## E.2 *Thermosynechococcus elongatus* BP-1

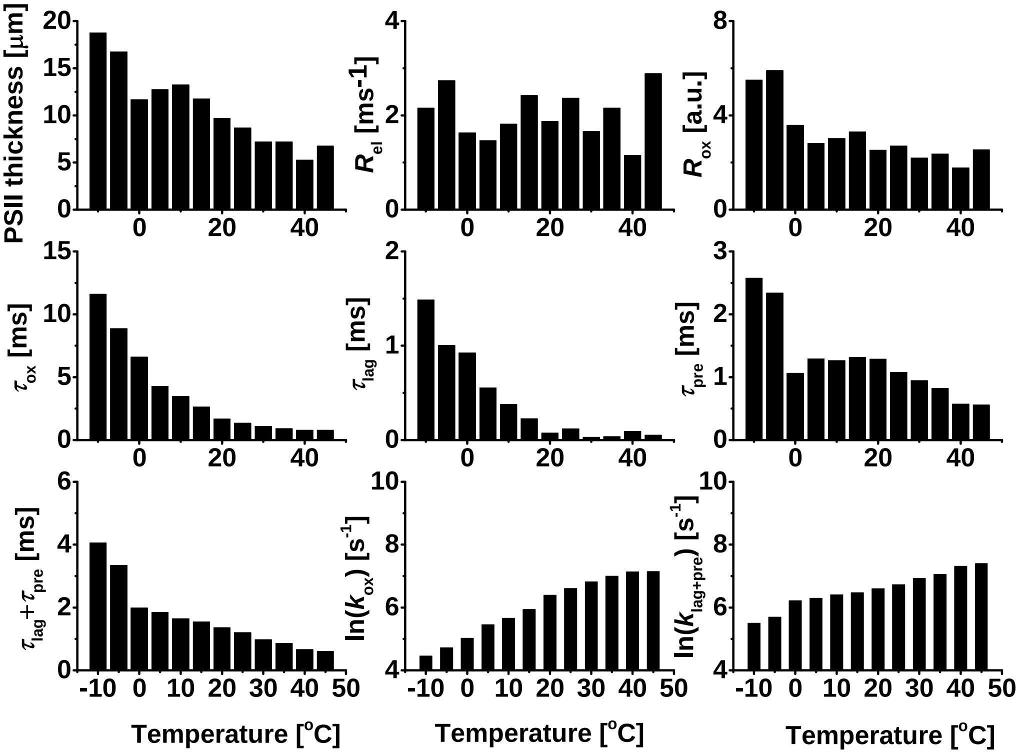

**Figure 0.5. Fit parameters of the diffusion model, applied to the individual transients of *Thermosynechococcus elongatus* BP-1 (wild-type). Orientation from upper left to lower right: (i) PSII thickness of the thylakoid membrane layer deposited on the electrode surface; (ii) $R_{el}$, electrode constant of the oxygen reduction speed; (iii) Rox, the population of the $S_3$ state; (iv) $\tau_{ox}$, the slow phase of oxygen evolution; (v) $\tau_{lag}$, the lag phase of the delay of electrode response; (vi) $\tau_{pre}$, the pre-phase of the delay of oxygen evolution; (vii) $\tau_{lag}$+$\tau_{pre}$, sum of the lag- and pre-phases;**

**viii) ln($k_{ox}$), rate constant of the slow phase of the in natural logarithmic scale; and (ix) ln($k_{lag+pre}$), rate constant of the sum of the lag- and pre-phases in natural logarithmic scale.**

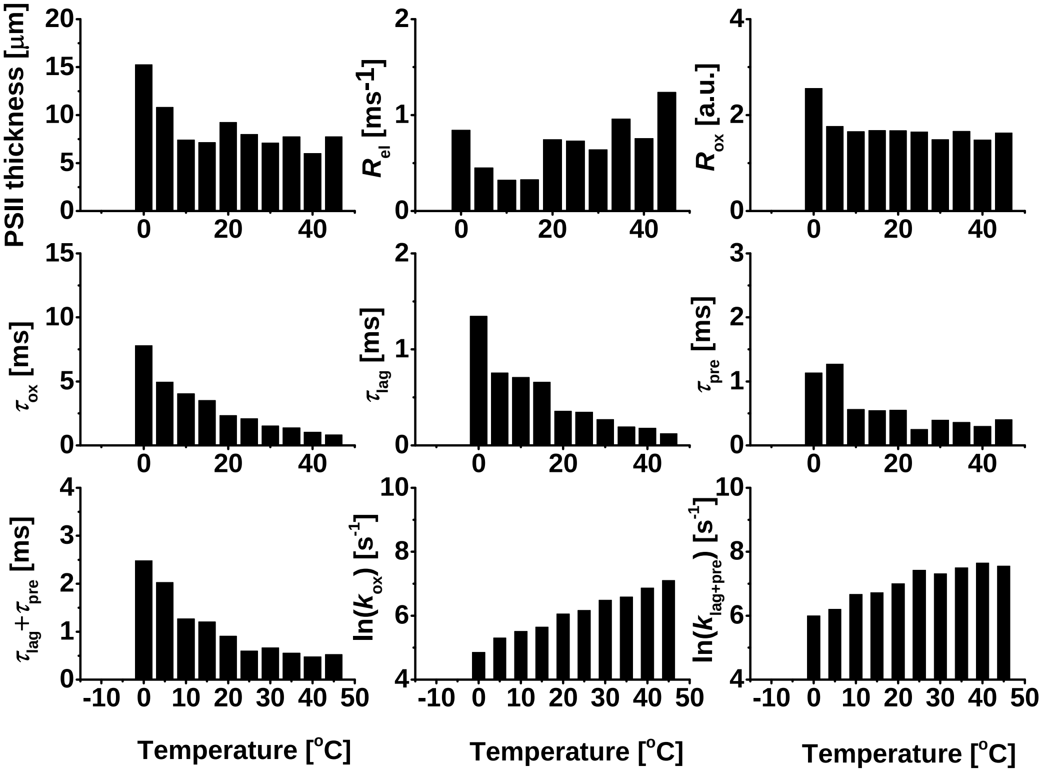

**Figure 0.6. Fit parameters of the diffusion model, applied to the individual transients of *Thermosynechococcus elongatus* BP-1 (PsbA3). Orientation from upper left to lower right: (i) PSII thickness of the thylakoid membrane layer deposited on the electrode surface; (ii) $R_{el}$, electrode constant of the oxygen reduction speed; (iii) Rox, the population of the $S_3$ state; (iv) $\tau_{ox}$, the slow phase of oxygen evolution; (v) $\tau_{lag}$, the lag phase of the delay of electrode response; (vi) $\tau_{pre}$, the pre-phase of the delay of oxygen evolution; (vii) $\tau_{lag}+\tau_{pre}$, sum of the lag- and pre-phases; viii) ln($k_{ox}$), rate constant of the slow phase of the in natural logarithmic scale; and (ix) ln($k_{lag+pre}$), rate constant of the sum of the lag- and pre-phases in natural logarithmic scale.**

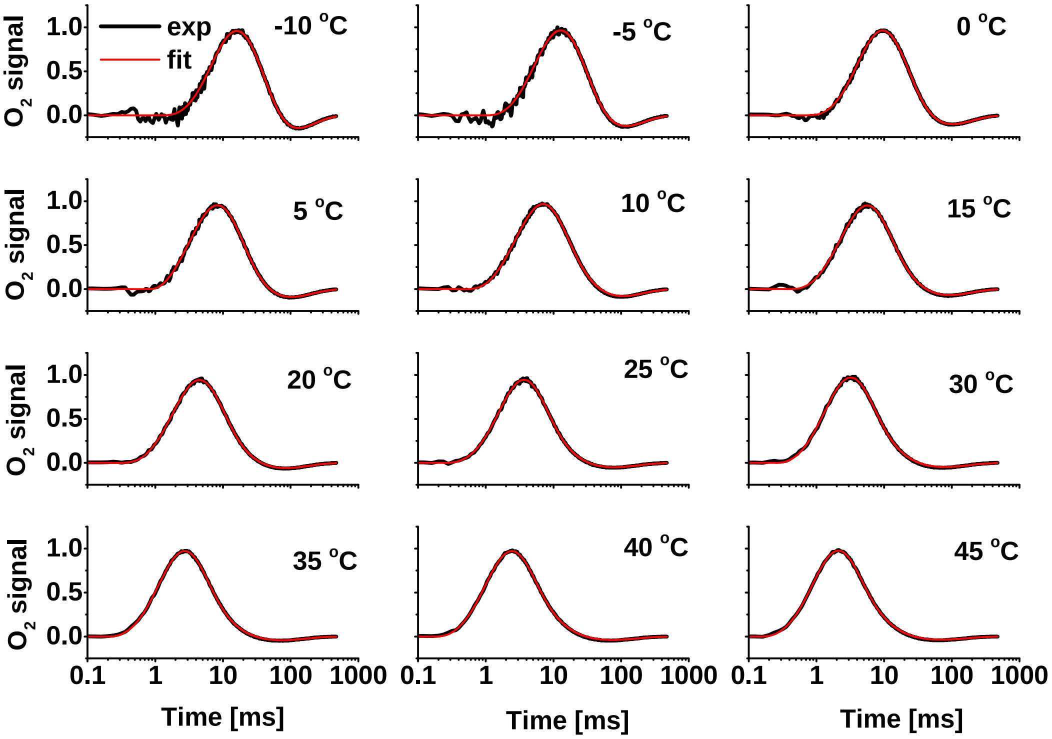

**Figure 0.7. Transients of the individual oxygen signal of *Thermosynechococcus elongatus* BP-1 (wild-type), fitted by oxygen diffusion model (experimental data in black and fit in red), from -10 °C to 45 °C (from upper left to lower right orientation).**

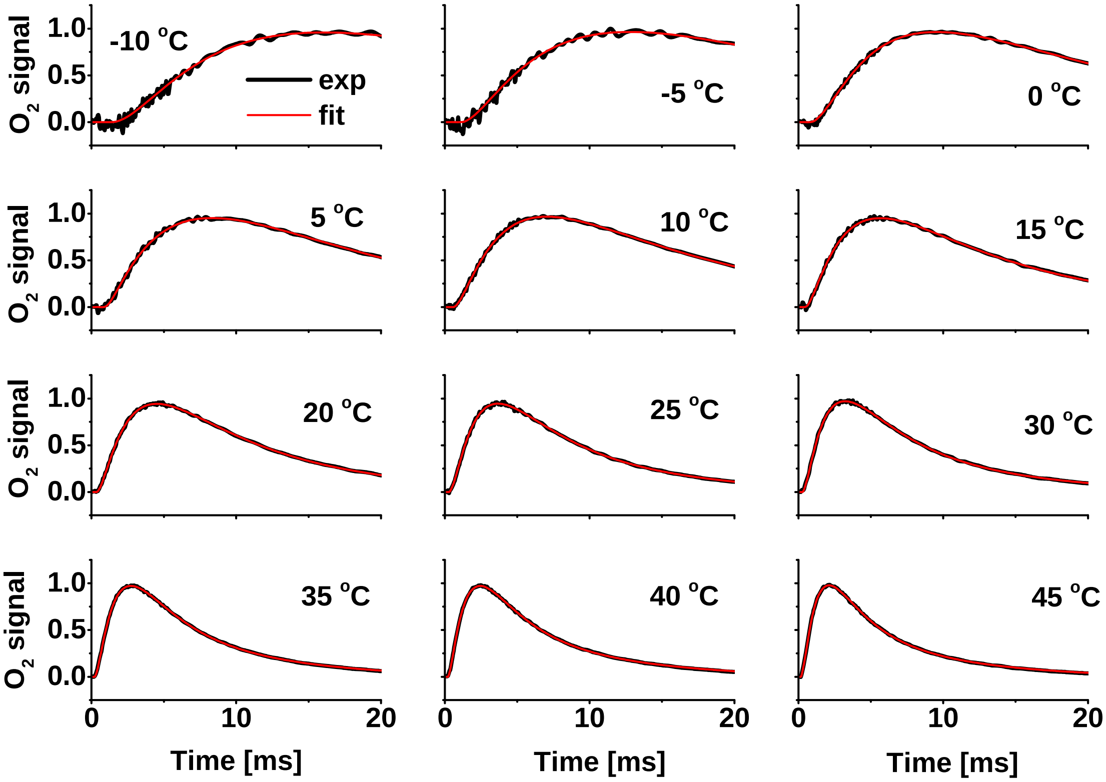

**Figure 0.8. Transients of the individual oxygen signal of *Thermosynechococcus elongatus* BP-1 (wild-type), fitted by oxygen diffusion model (experimental data in black and fit in red), from -10 °C to 45 °C (from upper left to lower right orientation). They are presented in linear scale from 0 to 20 ms, highlighting the rising time of the transients.**

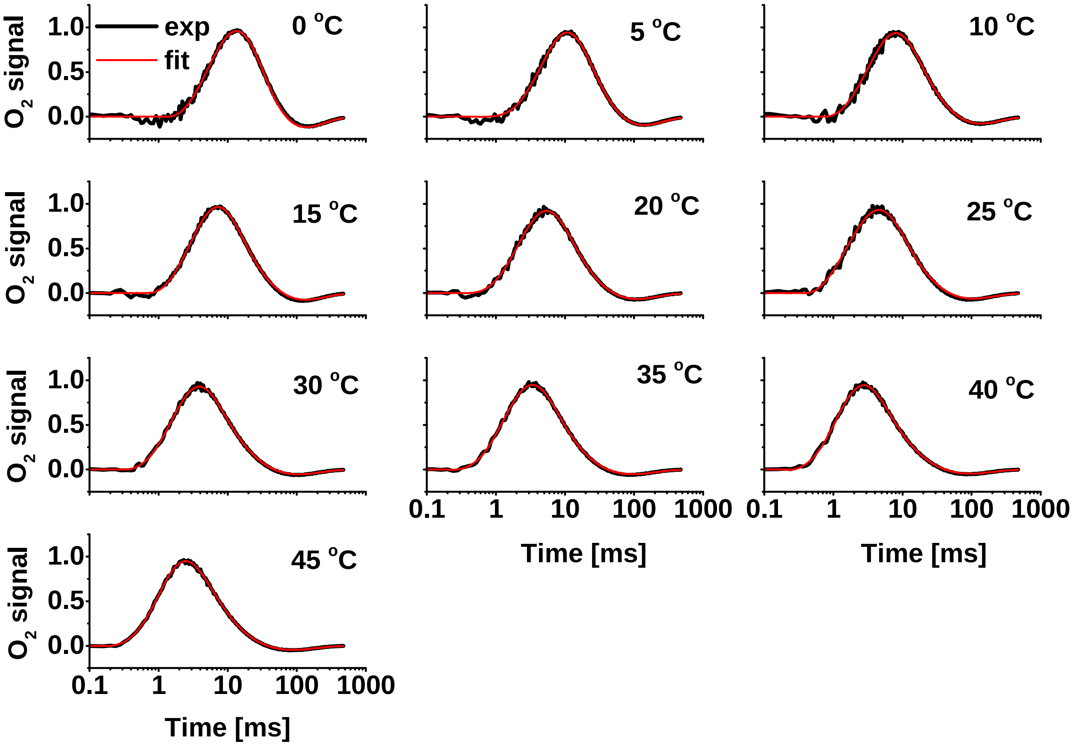

**Figure 0.9. Transients of the individual oxygen signal of *Thermosynechococcus elongatus* BP-1 (PsbA3), fitted by oxygen diffusion model (experimental data in black and fit in red), from 0 °C to 45 °C (from upper left to lower right orientation).**

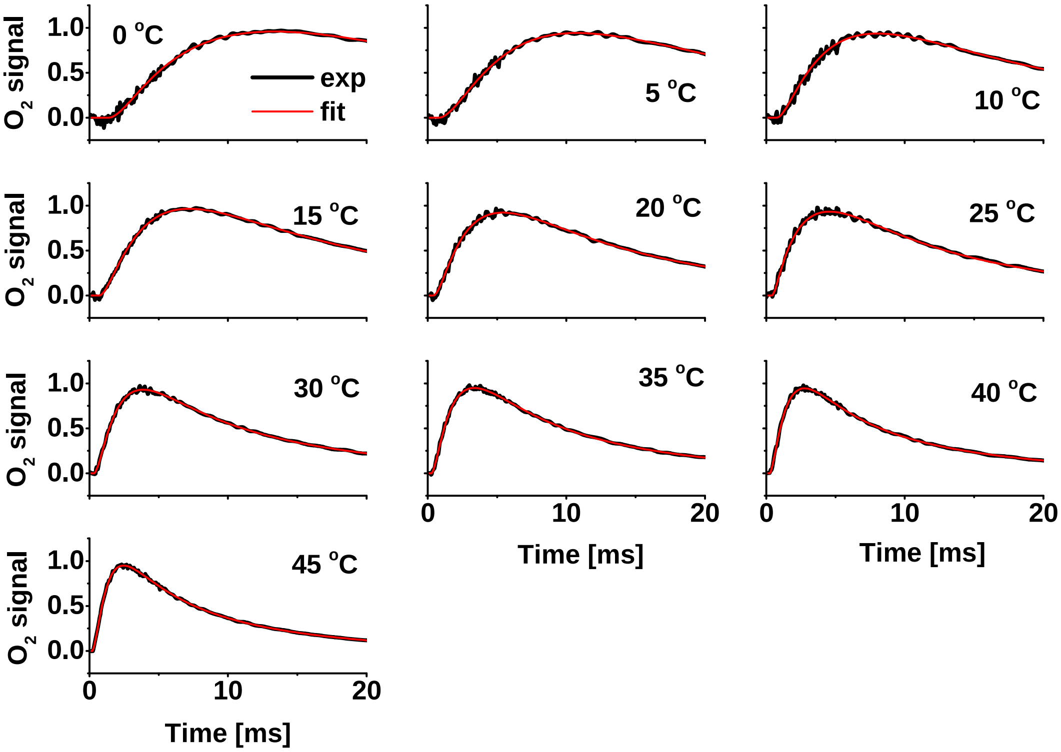

**Figure 0.10. Transients of the individual oxygen signal of *Thermosynechococcus elongatus* BP-1 (PsbA3), fitted by oxygen diffusion model (experimental data in black and fit in red), from 0 °C to 45 °C (from upper left to lower right orientation). They are presented in linear scale from 0 to 20 ms, highlighting the rising time of the transients.**

## E.3 Spinach

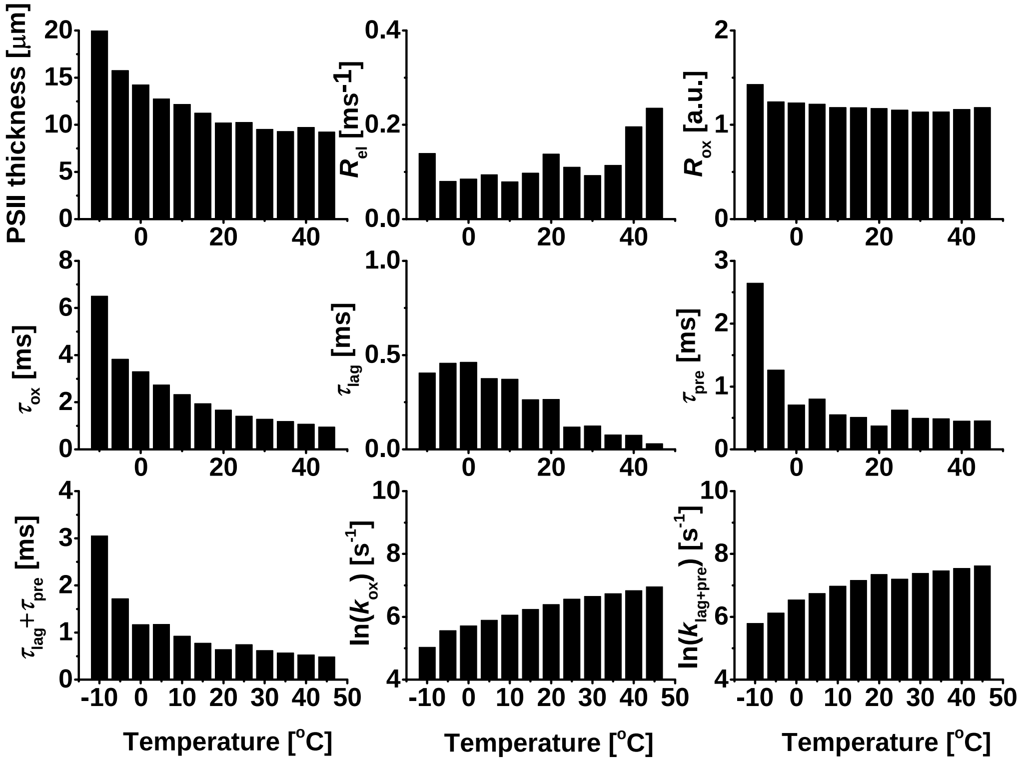

**Figure 0.11. Fit parameters of the diffusion model, applied to the individual transients of spinach. Orientation from upper left to lower right: (i) PSII thickness of the thylakoid membrane layer deposited on the electrode surface; (ii) $R_{el}$, electrode constant of the oxygen reduction speed; (iii) Rox, the population of the $S_3$ state; (iv) $\tau_{ox}$, the slow phase of oxygen evolution; (v) $\tau_{lag}$, the lag phase of the delay of electrode response; (vi) $\tau_{pre}$, the pre-phase of the delay of oxygen evolution; (vii) $\tau_{lag+}\tau_{pre}$, sum of the lag- and pre-phases; viii) ln($k_{ox}$), rate constant of the slow phase of the in natural logarithmic scale; and (ix) ln($k_{lag+pre}$), rate constant of the sum of the lag- and pre-phases in natural logarithmic scale.**

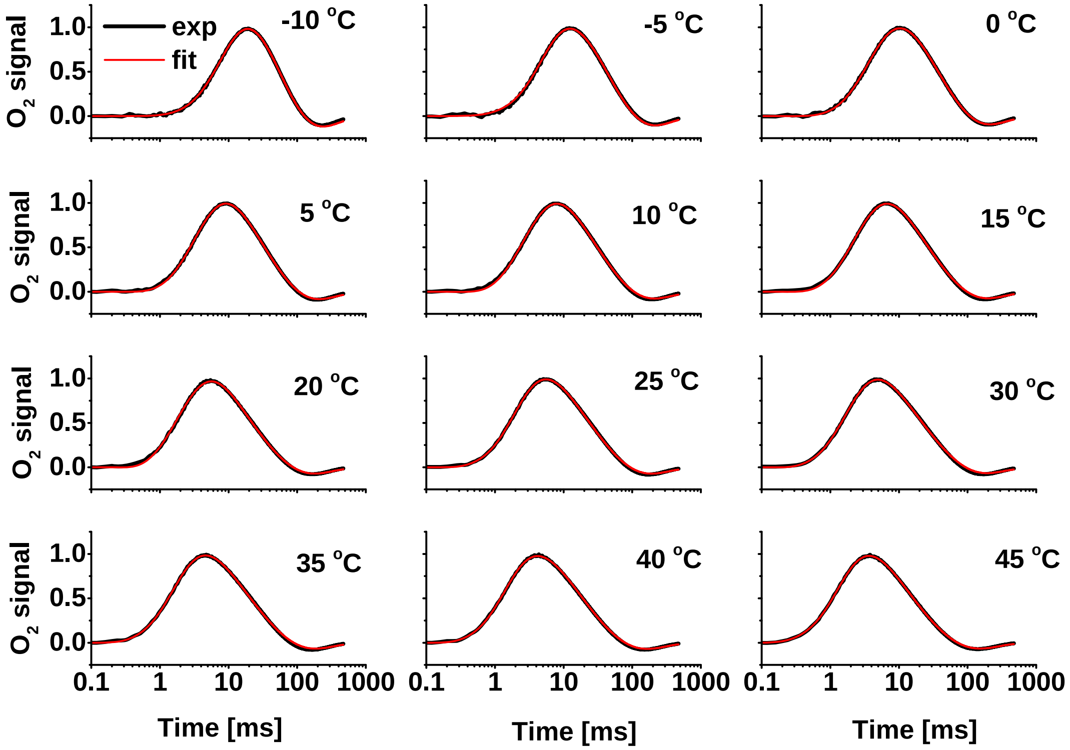

**Figure 0.12. Transients of the individual oxygen signal of spinach, fitted by oxygen diffusion model (experimental data in black and fit in red), from -10 °C to 45 °C in an increment of 5 °C (from upper left to lower right orientation).**

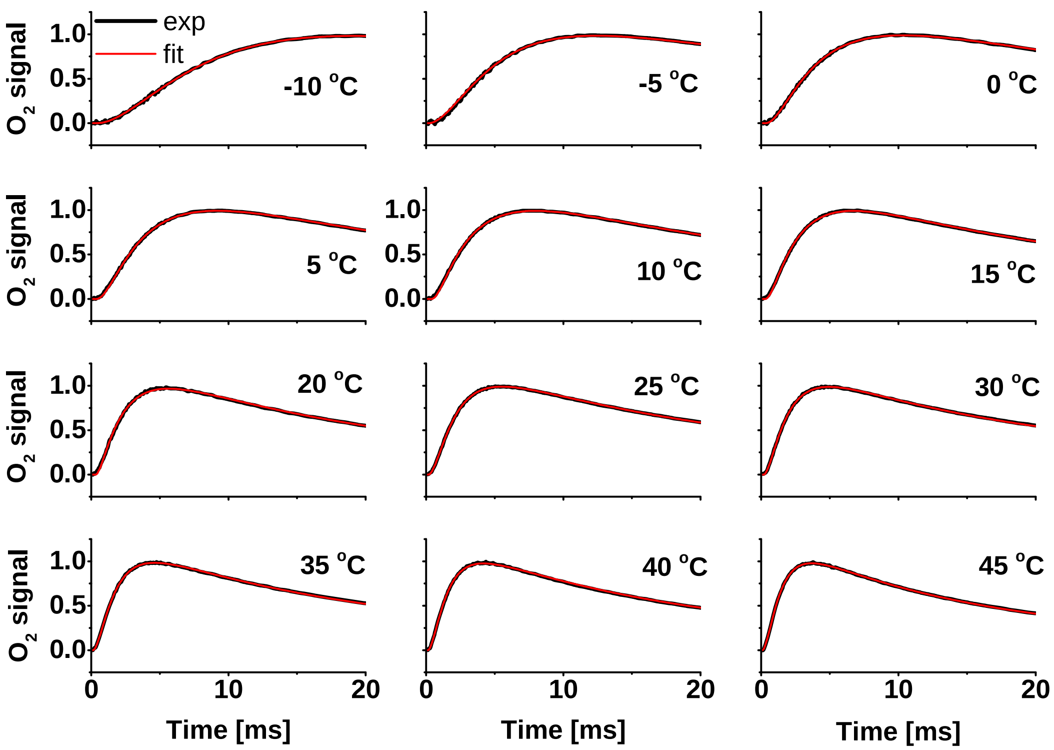

**Figure 0.13. Transients of the individual oxygen signal of spinach, fitted by oxygen diffusion model (experimental data in black and fit in red), from -10 ºC to 45 ºC (from upper left to lower right orientation). They are presented in linear scale from 0 to 20 ms, highlighting the rising time of the transients.**

# Appendix F Fitted Parameters of Figure 4.15

**0% glycerol**

| | | |
|---|---|---|
| Equation | y = a + b*x | |
| Weight | No Weighting | |
| Residual Sum of Squares | 0.00316 | |
| Adj. R-Square | 0.98252 | |
| | Value | Standard Error |
| Intercept | -3.80391 | 0.16437 |
| Slope | 0.10142 | 0.00408 |

**30% glycerol**

| | | |
|---|---|---|
| Equation | y = a + b*x | |
| Weight | No Weighting | |
| Residual Sum of Squares | 0.00675 | |
| Adj. R-Square | 0.9353 | |
| | Value | Standard Error |
| Intercept | -2.5326 | 0.21146 |
| Slope | 0.069 | 0.00522 |

# Appendix G Arrhenius Plots of Oxygen Release Rate Constants

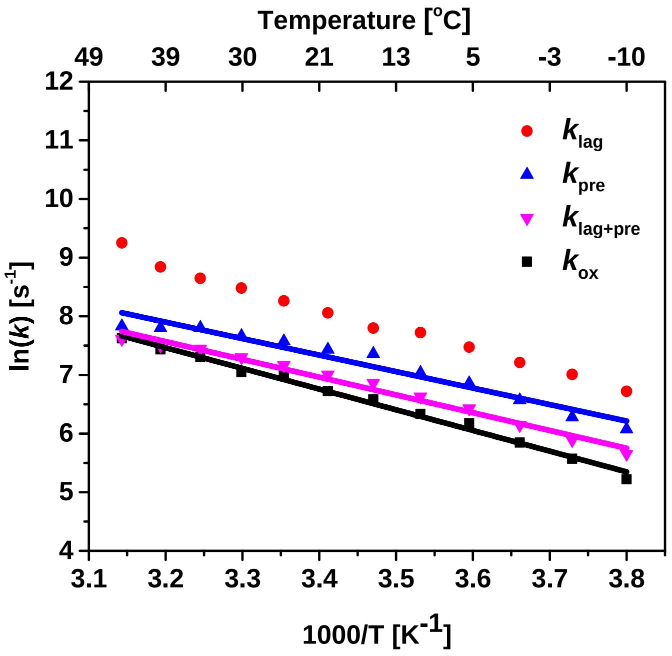

**Figure 0.14. Arrhenius plot of the rate constants of the lag phase (red), pre-phase (blue), the sum of lag and pre-phase (purple) and oxygen phase (black) of *Synechococcus* sp. PCC 7002. Kinetics are resolved from the diffusion model of the simulation. The symbols represent the experimental data while the lines in corresponding colour are obtained from a linear fit of the data. The plot is based on Arrhenius equation $\ln(k) = \ln(A) - E_a/k_BT$, where $k$ is the rate constant, $A$ is the pre-exponential frequency factor, and $E_a$ is the activation energy. $A$ and $E_a$ are determined from the intercept (y-axis) and slope, respectively. See detail fit parameters in Table 5-2 and Table 5-3 in Section 5.2.4.**

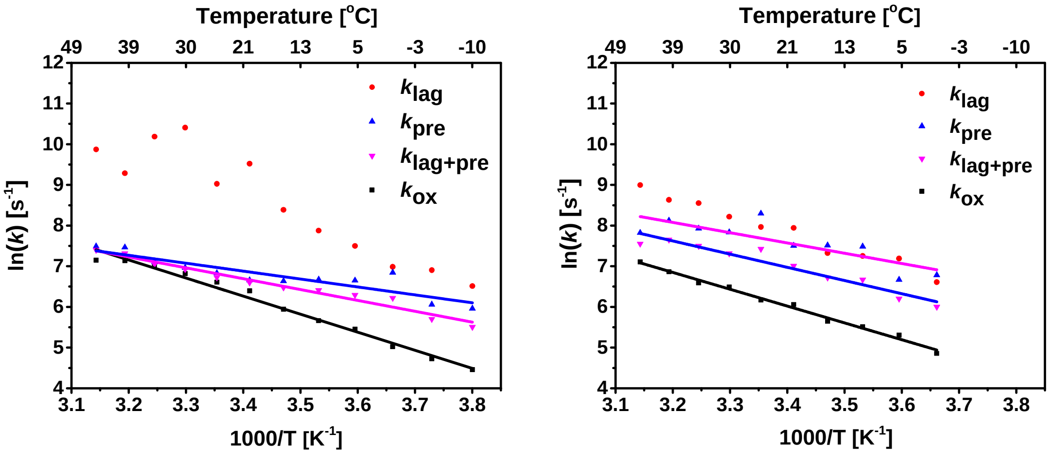

**Figure 0.15. Arrhenius plot of oxygen release rate constants of lag phase (red), pre-phase (blue), the sum of lag and pre-phase (purple) and oxygen phase (black) of *Thermosynechococcus elongatus* BP-1. (A) PSII wild-tpye and (B) PSII-PsbA3. Kinetics are resolved from the diffusion model of the simulation. The symbols represent the experimental data while the lines in corresponding colour are obtained from a linear fit of the data. The plot is based on Arrhenius equation $\ln(k) = \ln(A) - E_a/k_BT$, where $k$ is the rate constant, $A$ is the pre-exponential frequency factor, and $E_a$ is the activation energy. $A$ and $E_a$ are determined from the intercept (y-axis) and slope, respectively. See detail fit parameters in Table 5-2 and Table 5-3 in Section 5.2.4.**

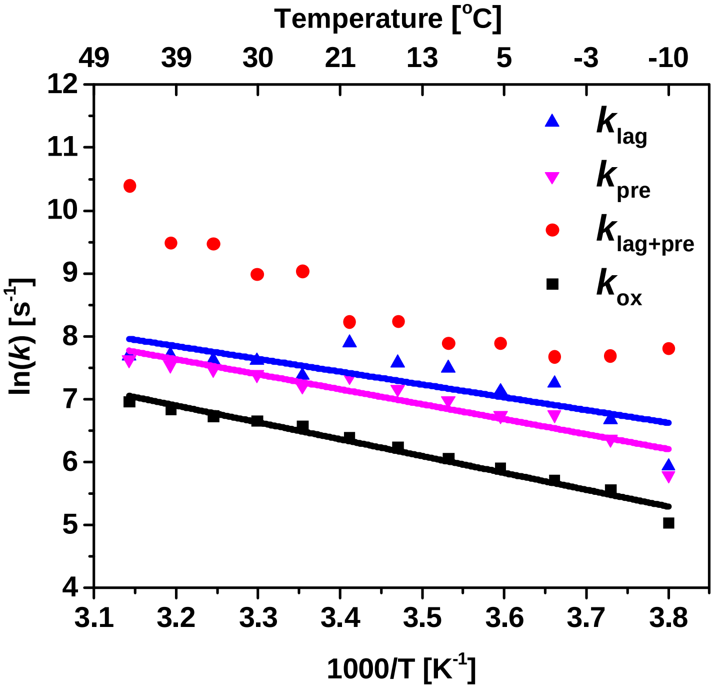

**Figure 0.16. Arrhenius plot of oxygen release rate constants of lag phase (red), pre-phase (blue), the sum of lag and pre-phase (purple) and oxygen phase (black) of spinach. Kinetics are resolved from the diffusion model of the**

**simulation. The symbols represent the experimental data while the lines in corresponding colour are obtained from a linear fit of the data. The plot is based on Arrhenius equation ln($k$) = ln($A$) - $E_a/k_B$T, where $k$ is the rate constant, $A$ is the pre-exponential frequency factor, and $E_a$ is the activation energy. $A$ and $E_a$ are determined from the intercept (y-axis) and slope, respectively. See detail fit parameters in Table 5-2 and Table 5-3 in Section 5.2.4.**

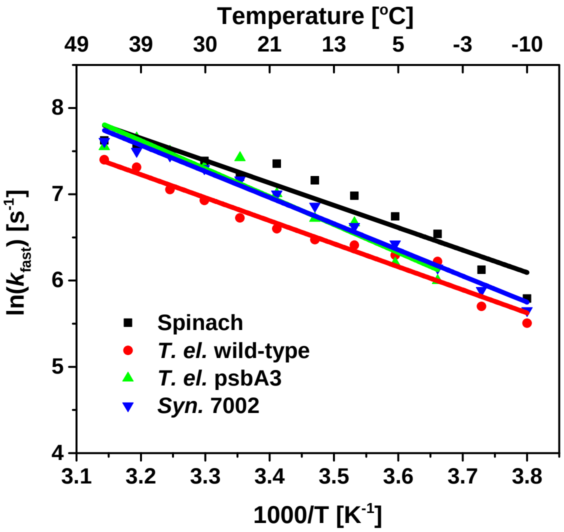

**Figure 0.17. Arrhenius plot of the rate constants of the fast phase (a sum of the lag and pre phases) $k_{ox}$, comparing PSIIs from *Synechococcus* sp. PCC 7002 (blue), *Thermosynechococcus elongatus* BP-1 wild-type (red) and PsbA3 (green) and spinach (black) from -10 °C to 45 °C, with increment of 5 °C. The lines are the linear fit of the data sets of corresponding colour.**

**Table 0-6. Fit parameters of the Arrhenius plot (in Figure 0.17), comparing spinach, *Thermosynechococcus elongatus* BP-1 PSII-wild-type and PSII-PsbA3, and *Synechococcus* sp. PCC 7002. $\tau_{fast}$ is the time constant of the fast phase at 20 °C, a and b are the slope and intercept from the linear regression, respectively, and $R^2$ is the fit deviation.**

| Species | $\tau_{fast}$ at 20 °C [ms] | Slope (a) [K·s$^{-1}$] | Intercept (b) [s$^{-1}$] | $R^2$ |
|---|---|---|---|---|
| Spinach | 0.64 | -2.38 | 15.25 | 0.91 |
| *T. elongatus* PSII-wild-tpye | 1.36 | -2.67 | 15.78 | 0.97 |
| *T. elongates* PSII-PsbA3 | 0.91 | -3.24 | 18 | 0.93 |
| *Synechococcus* 7002 | 0.91 | -3.03 | 17.27 | 0.98 |

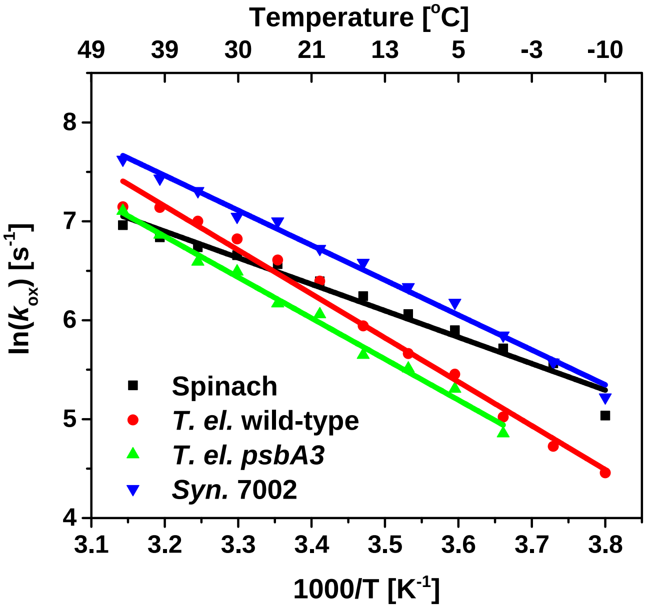

**Figure 0.18. Arrhenius plot of the rate constant of the slow phase, $k_{ox}$, comparing *Synechococcus* sp. PCC 7002 (blue), *Thermosynechococcus elongatus* BP-1 wild-type (red) and PsbA3 (green) and spinach (black) from -10 °C to 45 °C, with increment of 5 °C. The lines are the linear fit of the data sets in corresponding colour.**

**Table 0-7. Fit parameters of the Arrhenius plot (in Figure 0.18), comparing *Synechococcus* sp. PCC 7002, *Thermosynechococcus elongatus* BP-1 wild-type and PsbA3 and spinach. $\tau_{ox}$ is the time constant of the slow phase at 20 °C, a and b are the slope and intercept from the linear regression, respectively, and $R^2$ is the fit deviation.**

| PSII | $\tau_{ox}$ at 20 °C [ms] | Slope (a) [$K \cdot s^{-1}$] | Intercept (b) [$s^{-1}$] | $R^2$ |
|---|---|---|---|---|
| Spinach | 1.67 | -2.68 | 15.46 | 0.97 |
| *T. elongatus* PSII-wild-tpye | 1.67 | -4.44 | 21.37 | 0.98 |
| *T. elongates* PSII-PsbA3 | 2.34 | -4.14 | 20.09 | 0.99 |
| *Synechococcus* 7002 | 1.20 | -3.53 | 18.75 | 0.99 |

# Acknowledgement

I was often asked, what do you do in your research? How can your knowledge be applied to daily life? And why do you do that? I tried to explain the possible background and details of my study from different perspectives, starting from physics, biophysics, photosynthesis, photosystem II, catalysis, enzymes to electron and proton dynamics, targeting to understand a very tiny bit of what is happening in nature (a typical step of fundamental research). Frankly speaking, at the very beginning of the study, I thought the target was to understand nature in order to apply it to artificial photosynthesis and to then produce clean energy, for instance, by means of hydrogen. This is a reasonable blueprint for the next generation of renewable energy, with almost unlimited resources. However, I didn't manage to get all these done, as least not within my limited PhD period.

Actually, the more I got to know the background, challenges and difficulties in the community of photosynthesis, I started to realize that it was close to a mission impossible in the coming decades, not to mention only within the life-time of a PhD program. Instead, in my very specific program, the very limited couple of years allowed me to understand and investigate a very little step of the system, by diving into the tiny details as deep as possible. However, the more one approaches a topic in detail, the more questions one may have in mind on the next deeper level. Gradually this journey guides me to the searching for the meaning of life. Thanks to the beauty of curiosity.

First of all, I would like to give priority to Prof. Holger Dau, who was kind enough to invite me to work together by exploring the universe of PSII in the past five years. I am touched by his critical way of thinking, his dedication to science, as well as his patience to students. It is my pleasure to learn pretty much more than only science from his professional tutoring. Thanks to Prof. Ulrike Alexiev, who consulted me with constructive feedback along with timely encouragement.

One of the best parts of writing this thesis was the opportunity to learn from colleagues and friends more often than usual. I am deeply grateful to Dr. Yvonne Zilliges and Sarah Mäusle, who provided intensive and professional critics for my academic writing in specific and numerous ways as I wrote this thesis. Their insight definitely has brought this work up to another degree of profession. Yvonne, as an expert in cyanobacteria mutagenesis, filled the knowledge gap of my education in biology. And what is more, her passionate, motivating and extremely constructive ideas all together excited a very important source of power that pushes me walking forward. While Sarah, as a global citizen, was

unbelievably detail minded by instructing me about the rules of grammar in one of the popular languages in the world.

I am indebted to the PSII members in particular Philipp Simon and Dr. Matthias Schönborn, who helped to challenge the preparation of BBY from spinach as well as brain storm in the topics relevant to photosynthetic water oxidation. I benefited also from Matthias's excellent engineering of the oxygen electrode so that the important part of research didn't get a huge delay. In parallel, credits are delivered to Janis Hantke, Rebecca Christiana, Elena Laufer, Valentina Teresa Tovazzi and Hannah Davis, for their huge efforts in keeping the cyanobacteria as healthy as possible, followed by perfect protein preparation.

I am indebted to Oliver Karge and Dr. Ivelina Zaharieva, who showed me the entrance to the world of experimental biochemistry and biophysics by transferring their knowledge and experience in particular the fluorescence measurements. Thanks to Dr. Petko Chernev, for his knowledge in software and science that usually inspired a very deep discussion, not only around the office but also in Krumme Lanke, a place that could be awarded as one of the best meeting points for an academic debate. It is my honour to share the office with Chiara Pasquini, Paul Kubella and Ricardo Assunção. They helped to create a pleasant and relaxing office atmosphere around the clock despite our perfect mismatch in schedule occasionally. I am fortunate to meet Reza Mohammadi, Shan Jiang and Paul Greife regularly and developed interesting conversations not limited to our research interests. Thanks again to all members of AG Dau, including the current as well as the previous generations. Based on so much efforts working together from them, I was lucky to have a solid base to do research and develop my ideas. Thanks a lot to Frau Sieglinde Endrias, who always responded to my requests and supported me administratively whenever I had questions in mind. She definitely helped to relieve my stress besides academic headache to a great extent.

I am glad to have the support from the electronic and mechanic workshop in the Department of Physics in Free University of Berlin. Especially Herr Martin Rust and Herr Christian Güttler from the electronic as well as Herr Detlef Müller from the mechanic workshop, they came back to me every time with a component or an instrument in perfect shape. That was amazing.

It was a wonderful chance to study with all collaboration partners, even though we didn't yet manage to report the results or ideas to the journal of Nature or Science. I realize that it could be a hard choice. I would like to thank specifically Prof. Rob Burnap from Oklahoma State University, USA, for his experienced guidance and constructive ideas to the experimental work, as well as Dr. Daniela Russo from Institute Laue-Langevin, France for her intensive support in neutron scattering. In addition, the joint group meeting almost once per year was quite a luxury location to exchange ideas with experts and students from Umeå University, Uppsala University and University of Rome.

Funding support from the project SFB1078 (DFG) in cooperation with FU Berlin is highly appreciated. It was a solid electron source of my searching for the meaning of life. Thanks to Frau Sylvia Luther, Dr. Kerstin Wagner and Dr. Christian Frischkorn, for their fantastic organization for the project seminars, colloquiums and retreats. In particular Sylvia helped me to manage the scholarship perfectly in time. I was happy to have participated in the Dahlem Research School by learning a package of soft skills more than doing only 'Rocket Science'. Café Kornfeld, Café Baci and Café Cross in Dahlemdorf should be a good try if one gets stuck in mind from physics or whatever may add up stress.

The department of Physics in Umeå University, especially Prof. Ove Axner who explored my talent, recommended me to go further in physics research in a very constructive manner. And Prof. Roger Rolling played an important role to plan and bridge my study from a city neighbouring the arctic to the cultural centre of Europe.

Friends here in Berlin, especially Marion, Gabriela and Urban, who paid unbelievable efforts in leading me to the beauty of German language, challenging me to the art of German disciplines as well as touching the heart of German culture. Meanwhile, support from friends in China is highly appreciated, particularly Helen Chen and Tom Tang from Shenzhen, who coached me and helped me to gain more confidence in social perspectives in addition to academic way of thinking. Thanks to the friends who had helped me and taken care of me and loved me. There are too many to name. I didn't manage to write down all the details due to the tight schedule of a PhD program. Luckily, you know who you are.

Dr. Ling Sun shall take a significant part of the contribution. Not only because her expertise in Matlab impressed me with the magic of matrices, but also her passion in academic career amazed me in a great extent. Furthermore, her kindness and care hardly let me feel alone on the way to this milestone.

Family is always an important topic. I am glad to meet my brother Tao regularly, who brings me new ideas from time to time. The most grateful appreciation is given to my parents, who support this journey in every perspective unconditionally. They never forget to remind me that life and love matter the most.

Best wishes to all of us.

# Abstract

Photosynthetic water oxidation is a fundamental process that changed the atmosphere from an anaerobic to an aerobic one, first by cyanobacteria and then later on additionally by algae and plants. It is in the protein complex photosystem II (PSII) that oxygenic molecules are produced from water, driven by photoabsorption of solar radiation. The process is catalysed by a Mn-complex, the mechanism of which is still one of the unsolved questions.

In this thesis, results on the mechanism of O-O bond formation in photosynthetic water oxidation by PSII are reported, specifically from the kinetic and energetic point of view. The investigations were performed experimentally using three time-resolved techniques established previously, which involve the excitation with sequence of light flashes (of nanosecond or microsecond duration) and detection of time courses typically in the time domain from about 10 μs to 500 ms that reflect functionally crucial processes in PSII. These techniques are: (1) variable PSII fluorescence (prompt chlorophyll fluorescence), (2) delayed (recombination) fluorescence of PSII, and (3) time-resolved oxygen polarography.

Partial inhibition of oxygen evolving activity was found in both cyanobacterial and plant PSII using ammonia as a substrate analogue of water. Therefore, an anti-cooperative binding model was proposed for the first time wherein the ammonia binds at two different potential substrate water sites at the oxygen evolving complex (OEC). The model reconciles many aspects of the large body of experimental results on ammonia binding to PSII reported since 1975. The results of this study were published in the journal *Biochemistry* (Schuth, Liang, et al., 2017).

Investigation of the glycerol influence on the temperature dependence of PSII reactions revealed that, the activation enthalpy of O-O bond formation was significantly decreased in the presence of (30%) glycerol. In addition, the activation energy of O-O bond formation was compared among four PSII variants. A phenomenon of enthalpy-entropy compensation (EEC) of O-O bond formation was observed. A semi-quantitative model was newly proposed, that fits the experimental observation in EEC of both the wild-type and mutated PSII species, i.e. the non-local and local modification altered protein matrix, respectively. It explains the driving force of the EEC from the perspectives of the energy levels and probability in achieving a pre-transition state prior to the O-O bond formation. The model suggests that the experimentally observed enthalpy-entropy compensation may relate to evolutionary optimisation stability of the pre-transition state. A qualitatively similar explanation may be applicable to many other enzymatic processes.

# Zusammenfassung

Photosynthetische Wasseroxidation ist ein fundamentaler Prozess, der zunächst in Cyanobakterien und später auch in Algen und Pflanzen dazu führte, dass die einst anaerobe Atmosphäre in eine aerobe umgewandelt wurde. Ausgelöst durch die Absorption von Sonnenstrahlung, findet im Proteinkomplex Photosystem II (PSII) die Spaltung von Wasser in Sauerstoff und Protonen statt. Dieser Prozess wird von einem Mn-Komplex katalysiert, wobei der genaue Mechanismus eine bisher ungelöste Fragestellung darstellt.

In der vorliegenden Arbeit werden neue Erkenntnisse zum Mechanismus der O-O-Bindungsbildung in photosynthetischer Wasseroxidation von einem kinetischen sowie energetischen Standpunkt aus vorgestellt. Die Untersuchungen wurden mittels drei verschiedener, bereits etablierten, zeitaufgelösten Methoden experimentell durchgeführt: (1) variable PSII Fluoreszenz (prompte Chlorophyllfluoreszenz), (2) verzögerte (Rekombinations-) Fluoreszenz und (3) zeitaufgelöste Polarographie. Alle drei Methoden beinhalten die Anregung mit einer Sequenz von Lichtblitzen (mit einer Dauer im Bereich von Nano- bzw. Mikrosekunden) und der zeitaufgelösten Detektion eines Signals, welches Informationen über einen für PSII wichtigen Prozess enthält. Die Detektion erfolgte jeweils über einen Zeitraum von etwa 10 µs bis 500 ms.

Sowohl in cyanobakteriellem als auch in pflanzlichem PSII wurde eine partielle Inhibition der Sauerstoffproduktion festgestellt, wenn Ammoniak als Substratanalog für Wasser eingesetzt wird. In diesem Zusammenhang wurde zum ersten Mal ein anti-kooperatives Bindungsmodell vorgeschlagen, laut dem Ammoniak an zwei verschiedenen Bindungsstellen bindet, die potentielle Kandidaten für die Substratwasserbindung im Sauerstoff-produzierenden Komplex (OEC) darstellen. Das Modell bietet eine Erklärung für viele Aspekte der umfassenden experimentellen Ergebnisse zur Bindung von Ammoniak an PSII, welche seit 1975 Gegenstand der Forschung ist. Diese Ergebnisse wurden bereits im *Biochemistry*-Journal publiziert (Schuth, Liang et al., 2017).

Untersuchungen zum Einfluss von Glycerin auf die Temperaturabhängigkeit der Reaktionen in PSII ergaben, dass die Aktivierungsenthalpie der Sauerstoffbindungsbildung mit der Zugabe von 30% Glycerin signifikant herabgesetzt wird. Zusätzlich wurde die Aktivierungsenergie der O-O-Bindungsbildung vier verschiedener PSII-Varianten verglichen, wobei das Phänomen der Enthalpie-Entropie-Kompensation (EEC) beobachtet wurde. Ein semi-quantitatives Modell formuliert, das eine Erklärung für die experimentellen Beobachtungen der EEC liefert. Dies gilt sowohl für die Ergebnisse verschiedener Wildtyp-PSII als auch mutierter PSII-Spezies, d.h. für nicht-lokale sowie lokale Modifikationen der Proteinmatrix. Das Modell erklärt die treibende Kraft der EEC aus der Perspektive von Energieniveaus und der Wahrscheinlichkeit, den Übergangszustand vor der O-O-Bindungsbildung zu erreichen. Zudem deutet das Modell auf die Möglichkeit hin, dass die observierte Enthalpie-Entropie-Kompensation eine Folge der evolutionären Stabilisierung des Übergangszustands sein könnte. Qualitativ ähnliche Erklärungen könnten auf zahlreiche andere enzymatische Prozesse anwendbar sein.

# List of Publications

Nils Schuth#, **Zhiyong Liang**#, Matthias Schönborn, André Kussicke, Ricardo Assunção, Ivelina Zaharieva, Yvonne Zilliges, and Holger Dau (2017).

# These authors contributed equally.

“Inhibitory and Non-Inhibitory NH3 Binding at the Water-Oxidizing Manganese Complex of Photosystem II Suggests Possible Sites and a Rearrangement Mode of Substrate Water Molecules.”

Biochemistry 56(47):6240-6256.

DOI:10.1021/acs.biochem.7b00743

[Chapter 3: **Ammonia Binding to the Water-oxidizing Manganese Complex of PSII**]

# Selbständigkeitserklärung

Ich erkläre gegenüber der Freien Universität Berlin, dass ich die vorliegende Doktorarbeit selbstständig und ohne Benutzung anderer als der angegebenen Quellen und Hilfsmittel angefertigt habe. Die vorliegende Arbeit ist frei von Plagiaten. Alle Ausführungen, die wörtlich oder inhaltlich aus anderen Schriften entnommen sind, habe ich als solche kenntlich gemacht. Diese Arbeit wurde in gleicher oder ähnlicher Form noch bei keiner anderen Universität als Prüfungsleistung eingereicht und ist auch noch nicht veröffentlicht.

Datum Unterschrift